DYNAMIC VISUALIZATION OF PROTEIN INTERACTIONS: MAPPING AND FRET BIOSENSOR DEVELOPMENT

by

Laurel Oldach

A dissertation submitted to The Johns Hopkins University in conformity with the requirements of the degree of Doctor of Philosophy

Baltimore, Maryland

December, 2017

Abstract

Intracellular levels of the RNA-binding protein and pluripotency factor, Lin28a, are tightly controlled to govern cellular and organismal growth. Lin28a is extensively regulated at the post-transcriptional level, and can undergo mitogen-activated protein kinase (MAPK)-mediated elevation from low basal levels in differentiated cells by phosphorylation-dependent stabilizing interaction with the RNA-silencing factor HIV TAR-RNA-binding protein (TRBP). However, molecular and spatio-temporal details of this critical control mechanism remained unknown. In the second chapter of this work, we dissect the interacting regions of Lin28a and TRBP proteins and develop a sensor to visualize this interaction. We identify truncated domains of Lin28a and of TRBP that are sufficient to support co-association and mutual elevation of protein levels, and a requirement for MAPK-dependent phosphorylation of TRBP at putative ERK-target serine 152 in mediating increase of Lin28a protein by TRBP. The phosphorylation-dependent association of Lin28a and TRBP truncated constructs is leveraged to develop a FRET-based sensor for dynamic monitoring of Lin28a and TRBP interaction. We demonstrate response of this FRET sensor to growth factor stimulation in living cells, with coimaging of Erk activation to achieve further understanding of the role of MAPK signaling in Lin28a regulation.

The IκB kinase (IKK) is a key mediator of NFκB activation, which affects inflammatory signaling. In the third chapter of this work, we expand our focus from Lin28a to review the process of biosensor development for kinase activity,

taking as a case study our efforts to develop a FRET-based biosensor for IKK. We successfully identified an IKK substrate peptide that could be inducibly phosphorylated, and had some success in visualizing this substrate's phosphorylation. However, further optimization will be required to engineer a sensor that reliably diffuses throughout the cell and does not perturb the NFκB signaling status of the cell.

Acknowledgments

This dissertation process was an education in team science.

This work would have been impossible to complete without the steadfast support and mentorship of Dr. Jin Zhang. For her initial openness to the idea of a comentored project, her kind guidance and keenly directed questions along the way, and her great generosity in supporting me as a student in another lab for the final two years of my degree, I am deeply indebted to her.

I also owe thanks to Dr. Mollie Meffert, who introduced me to Lin28 and TRBP, and whose ability to recruit a team of passionate scientists with laser focus is truly impressive. I thank her for teaching me so much about experimental design, troubleshooting, and interpretation, and for her focused approach to questions.

I am grateful to the other members of my thesis committee, Dr. Takanari Inoue and Dr. Mike Caterina, for asking good questions at the right times, helping me at crucial points, and supporting my science publishing aspirations. In particular, I appreciate the generosity of the Inoue lab in sharing microscopes and training, and inviting me to join in lab meetings.

I learned a tremendous amount about fluorescence microscopy, confocal and otherwise, from Dr. Sohum Mehta, Dr. Gary Mo, Dr. Randy Reed, and Dr. Michelle Pucak. I thank each of them for their patience and technical acumen. Dr. Nwe-Nwe Aye-Han, to whom I am grateful for her patient training, started the IKK sensor portion of the project. Thanks also to the other members of the Zhang lab with whom I overlapped: Terri Clister, who was both a colleague and a

roommate; Brian Ross, Kirill Gorshkov, Brian Tenner, Xin Zhou, Fabian Hertel, Charlene Depry, and Qiang Ni.

For guidance on the difficult immunoprecipitation of Lin28 and TRBP, I thank Dr. Alex Amen. For training in how to successfully culture hippocampal neurons, I am grateful to Dr. Daniel Pham. Thanks to all the other members of the Meffert lab, including Megha Subramanian, Purnima Padmanabhan, Timothy Gamache, Christina Timmerman, Joshua Schwarz, Leo Hagmann, Claudia Ruiz and Jay Shi for making the lab a home away from home. Thanks to rotation student Billy Mills for logistical and cloning support at a busy time.

The academy runs because of the competent professionals who keep it running. I am grateful to the Biological Chemistry department office; to the Pharmacology department offices—especially Amy Paronto, who fielded the majority of my questions—and most of all to the BCMB program office: Arhonda Gogos, Sharon Root and Carolyn Machamer. As I begin my next steps, I thank the Biomedical Careers Initiative, especially Caroline Pounds, for helping me get there.

Thanks to all of the members of my cohort in the Biochemistry, Cellular and Molecular Biology program, who have become dear friends as well as valued colleagues. Risa Burr, Catherine Gilbert, Mark Zbinden, John and Kelsey Bettridge, Stefanie Tan, Tom Schaeffer, and Jarrett Smith, this journey would have been more difficult without your energy, commiseration, and support (both technical and emotional). I am also grateful to my friends outside of science for

their sympathy and patience, even though the demands of lab work were unfamiliar to them.

Finally, thanks to my family: Warren Weber, Phoebe and Eliza Oldach, David Oldach, Toby Ritterhoff, and all of the members of the Ritterhoff and Oldach families, who collectively supported me every step of the way.

Table of Contents

List of Figures and Tables

This page intentionally blank.

Introduction

Introduction to cell signaling

Cells process external information through signal transduction to evoke appropriate responses. Post-translational modifications to proteins, such as phosphorylation, glycosylation, and methylation, offer a group of mechanisms for rapidly changing the function of proteins and pathways to mediate signal transduction. These modifications are generally executed by enzymes, such as kinases for phosphorylation and phosphatases for removal of phosphate groups. Because of the dynamic and reversible nature of phosphorylation, and its broad spectrum of effects on protein function, understanding the activity of such enzymes is of great interest. Since their first introduction in the late 1990s, genetically encodable FRET sensors for kinase activity and second messengers have emerged as powerful tools to probe cellular signaling events (Mehta & Zhang, 2011). Chapter 3 of this thesis gives a more in-depth review of the development and implementation of FRET biosensors, especially for kinase activity, and their utility for understanding localized changes within cells.

Neurons are highly compartmentalized and specialized signaling cells, encoding a high degree of complexity to carry out their function. Differentiated neurons have extraordinarily complicated signaling architectures, with many levels of compartmentalization, from large divisions such as dendrite/axon/soma, to macrocompartments such as dendritic spines, to microcompartments such as those found in the neighborhood of receptors at the synapse. Each of these

signaling environments maintains a unique identity and contributes to the cell's capacity for input, summation, coincidence detection, and many other computations without which cognition would be impossible. Studies using real-time kinase and second messenger indicators in differentiating neurons have furthered our understanding of the specification of these signaling environments from undifferentiated neurites (Shelly et al., 2010; Shelly et al., 2011). In mature neurons, biosensor probes are useful in understanding how biochemical computations occur, which kinases participate in spatially-restricted signaling, and what functional sub-compartments are involved in mediating synaptic inputs.

Signaling in synaptic plasticity

Hippocampal pyramidal neurons are an excitatory cell type in the hippocampus. Their architecture is highly complex, with a tree-like dendritic arbor branching out from the soma. Budding from each dendrite are numerous dendritic spines, each of which can receive excitatory synaptic inputs from other neurons. At synapses, the spine is closely apposed to the axon terminal of another neuron. Within the spine, a region called the postsynaptic density is a cluster of densely packed neurotransmitter receptors, scaffolding proteins, and signal transduction factors. In response to repetitive trains of release of the excitatory neurotransmitter glutamate by presynaptic neurons, signaling originating from within the PSD transduces to the rest of the neuron, enabling synapses to increase in strength, a phenomenon known as long-term potentiation (LTP) (reviewed by Kennedy, 2000).

LTP occurs in two phases. In the early stage, calcium-dependent cytoskeletal changes mediate growth of the spine, and receptor trafficking to the postsynaptic membrane mediates an increase in responsiveness to neurotransmitter release. Lee and colleagues showed using a FRET-based activity probe that the calcium dependent kinase CaMKII is activated only in individual stimulated spines, and that kinase activation level is proportional to the growth of the spine (Lee et al., 2009). Meanwhile, signaling events induce translation both local to and distal from the synapse. If translation is blocked, early stage spine growth is transient, and the spine reverts to its baseline size within about an hour (Yang et al., 2008). New protein synthesis enables lasting changes to the size and strength of synaptic connections. Because stronger connections mediate better neuronal communication, long-term potentiation has come to be appreciated as a cellular correlate of learning-induced plasticity (Kandel, 2001).

Autocrine BDNF release after glutamate stimulation of a single spine indicates a crucial role for brain-derived neurotrophic factor (BDNF) in LTP (Harward et al., 2017). When BDNF signaling is blocked, glutamate alone can induce transitory spine growth, but is not adequate to induce enduring LTP (Montalbano et al., 2013; Tanaka et al., 2008). *In vivo*, BDNF plays an integral role in memory formation, with knockout animals showing defects in long-term potentiation (Patterson et al., 1996) and spatial learning (Linnarsson et al., 1997). In dissociated hippocampal neuron culture, BDNF treatment results in increased dendritic arborization (Cohen-Cory et al., 1999) and greater abundance and size

of dendritic spines (Alonso et al., 2004). Importantly, there is evidence that spatial restriction of BDNF availability within a neuron limits these changes to the areas exposed to BDNF (Horch & Katz, 2002; Tanaka et al., 2008; Aakalu et al., 2001).

Excitatory signaling through BDNF

After binding of glutamate to postsynaptic NMDA receptors, the calmodulin dependent kinase CamKII is activated, triggering autocrine release of BDNF (Harward et al., 2017). BDNF is recognized by the receptor tyrosine kinase TrkB, whose homodimerization and autophosphorylation activate numerous signaling pathways, including MAPK/Erk, PI3K/Akt/mTor and phospholipase C (see figure 1.1) (reviewed by Chao, 2003). These pathways affect both translation-independent and translation-dependent mediators of LTP.

BDNF induces translation-independent short-term strengthening of synaptic connections through protein trafficking and modulation of cytoskeletal dynamics. TrkB activation causes NMDA receptor insertion into the postsynaptic membrane (Caldeira et al., *Mol Cell Neurosci* 2007), and scaffolding protein PSD95 localization to the postsynaptic density (Yoshii and Constantine-Paton, 2010). BDNF also promotes changes in actin dynamics through GTPase activity. RhoA-induced activation of Lim kinase 1 inhibits the actin protease cofilin in dendritic spines, allowing for actin polymerization, while Rac stimulates the kinase PAK, regulating actin branching (Rex et al., 2007). Together, these

translation-independent changes strengthen the synaptic response to each neurotransmitter release and increase the size of the spine.

Translation-independent changes to cytoskeletal dynamics and receptor localization are reinforced by changes in local protein synthesis, which are required for enduring synaptic plasticity. Dendrites have been known for some time to be competent to translate new proteins in response to BDNF, even if separated from the cell body (Bradshaw et al., 2003; Huang & Kandel, 2005; Kang & Schuman, 1996). BDNF induces an increase in synaptic protein translation through Erk-dependent pathways, which are discussed in the next section. Local translation adds to the available pool of receptors and signaling proteins (Schratt et al., 2004). BDNF also mediates local synthesis of the GTPase RhoA (Briz et al., 2015), the cytoskeleton-associated scaffolding protein Arc (Messaoudi et al., 2007; Bramham et al., 2010), and many components of the translation machinery including translation factors and ribosomal proteins (Caravalho et al., 2008; Aakalu et al., 2001; Liao et al., 2007).

Other effects of BDNF on gene expression depend on long-range signaling to the nucleus to activate transcription of target genes. A number of transcription factors, including NFκB, CREB and NFAT, can be activated by BDNF and translocate from the dendrite or synaptic spine to the nucleus (Meffert et al., 2006; Pizzorusso et al., 2000; Groth & Mermelstein, 2003). Similarly, some enzymes, including the MAP kinase Erk (Patterson et al., 2001) can be translocated in active form.

Erk signaling in synaptic plasticity

The MEK/Erk pathway is a well-known intermediate in the response to BDNF, activated by TrkB within minutes after BDNF treatment (Ying et al., 2002). Erk activity is absolutely required for long-term potentiation (LTP) (English et al., 1996; Davis et al., 2000) and for lasting BDNF-induced increases in spine size and density (Alonso et al., 2004; Huang et al., 2012). While some Erk pathway targets function at the synapse to reinforce LTP, this kinase also induces signaling to and itself translocates to the nucleus, where it induces further changes in mRNA expression (Cohen et al, 2011; Wiegert et al., 2007).

Like all kinases in the MAPK family, Erk1/2 is activated by a highly specific response pathway. Downstream of receptor tyrosine kinases such as TrkB, GTPases, such as Ras, activate serine/threonine MAP3Ks, such as Raf. Active MAP3K phosphorylates a dual-specificity MAP2K, such as MEK, which phosphorylates the activation loop of Erk1/2 at threonine 183 and tyrosine 185 (Canagarajah et al., 1997). This pathway can also be activated Rtk-independently through crosstalk with other signaling pathways. For example, Ras GTPase can be activated by PKC, e.g. by the direct PKC activator PMA (Mendoza et al., 2011).

Once activated, MAPKs can phosphorylate serine or threonine residues, dependent on presence of a proline in the next residue. Studies of phosphorylation on purified peptides indicate that PX[S/T]P is a strong substrate for ERK1/2 (Gonzalez et al., 1991). Substrate specificity is also conferred by docking motifs within the MAPK substrate, near but not within the substrate site.

Some important docking motifs include the D box, a lysine/arginine-rich docking motif, and the amino acid sequence DEJL, which are recognized both by Erk and by its fellow MAP kinase JNK; and an FXFP motif, which mediates only Erk docking, and dramatically enhances the rate of phosphorylation (Jacobs et al., 1999).

Erk diffusibility- mechanisms and means of study

MAPK signaling can be spatially controlled by molecular scaffolding, which can mediate activation of a kinase, directly control its localization, or drive selection of substrates by enhancing kinase/substrate proximity (Dhanasekaran et al., Oncogene 2007). At the synapse, a scaffolding protein, Homer, can directly bridge metabotropic glutamate receptor 5 (mGluR5) to Erk to mediate kinase activation after stimulation of the receptor (Mao et al J Neursoci 2005). The scaffolding protein kinase suppressor of Ras 1 (KSR1), controls compartmentalization of MEK and Erk to the dendritic spine or shaft in a homeostatic fashion, such that Erk-induced phosphorylation of KSR1 drives exclusion of KSR1 and Erk from the spine (Canal et al., 2011). Moreover, active Erk binds to importins and translocates to the nucleus, where it is released to phosphorylate nuclear substrates including a variety of transcription factors and repressors and chromatin remodeling factors(Li et al., 2016; Wainstein et al., 2016; Plotnikov et al., 2011).

FRET imaging using biosensors for kinase or other enzymatic activity has been an extremely beneficial tool to observe spatial control of signaling activity in

neurons. Certain enzymes such as CaMKII and Cdc42 are activated strictly in synaptic spines exposed to glutamate uncaging, giving a long-lasting mechanism for spine differentiation from inactive synapses (i.e., synaptic tagging) (Lee et al., 2009; Hedrick et al *Nature* 2016). In contrast, other GTPases, including Ras, Rac1 and RhoA, can diffuse out of the activated spine, priming nearby spines for stronger response to sub-threshold stimuli (Hedrick et al., 2016; Yasuda & Murakoshi, 2011; Harvey et al., 2008). In the case of Erk1/2, recent work shows that its activity is highly diffusible between a single activated dendritic spine and both the associated dendrite and neighboring spines (Tang and Yasuda, 2017).

Downstream targets of Erk in synaptic plasticity

Erk supports rapid changes to synaptic transmission through phosphorylation of glutamate receptors mGluR1 and 5; the voltage-gated potassium channel Kv4.2; and scaffolding proteins of the post-synaptic density (reviewed by Thomas & Huganir, 2004).

Among Erk's other substrates in the spine are fellow kinases such as MSK1 (Correa et al., 2012) and MNK1. Activated MNK1 phosphorylates translation initiation factor eIF4E, increasing association between the initiation factor and mRNA granules, and promoting its translocation to the spine, thereby upregulating synaptic translation (Panja et al., 2014; Takei et al., 2001; Smart et al., 2003). MNK may also relieve individual transcripts from binding by the translational repressor complex CYFIP1/FMRP (reviewed by Bramham et al., 2016).

Erk activity also supports signaling to the nucleus through its own translocation and through activation of transcription factors including NFkB, Elk1 and CREB (reviewed by Thomas & Huganir, 2004). Erk-dependent BDNF target genes include both synaptic gene products such as Homer and Arc, and other genes such as long noncoding RNAs and primary microRNA transcripts (Messaoudi et al., 2007; Bluthgen et al., 2017; Jaitner et al., 2016).

Canonical miRNA biogenesis

Changes to cellular protein concentration can be achieved efficiently, and without requiring de novo transcription, by modulations to microRNA levels (Baek et al., 2008; Selbach et al., 2008). MicroRNAs are transcribed in the nucleus as pri-miRNAs, which are processed by Drosha and its cofactor DGCR8, a complex known as the microprocessor, before export into the cytoplasm in stem-and-loop pre-miRNA form. The nuclease enzyme Dicer, in complex with its cofactor TRBP, the Tar RNA binding protein, cleaves pre-miRNA into mature microRNAs in the cytoplasm. Mature miRNAs assemble into an Ago2-containing complex known as RNA induced silencing complex (RISC), which modulates translation of target mRNAs (See figure 1.2A).

Signal-responsive changes to miRNA biogenesis

To control mature miRNA level and repressive activity, Microprocessor and Dicer activity are required. Post-translational regulation of microRNA biogenesis factors is increasingly appreciated as a mechanism for tuning miRNA

biogenesis (Ha & Kim, 2014). For example, DGCR8 phosphorylation by MAPK signaling can alter miRNA output (Herbert et al., 2013). Moreover, post-translational modification of RISC components can occur at the synapse; such modifications can provide a link between signaling and the rapid proteome changes observed at the synapse (Sambandan et al., 2017).

miRNA changes in synaptic plasticity

Given the importance of local translation within the dendrite to LTP described above, it is increasingly appreciated that microRNA biogenesis in the dendrite can exert control of the genes translated there. Inducible deletion of Dicer in the forebrain of adult mice leads to significant upregulation of BDNF, PSD95 and GluA1, indicating that microRNAs play a significant role in modulating protein expression and synaptic responses (Konopka et al., 2010).

There is considerable evidence for changes to specific microRNAs resulting from coordinated changes to transcription and RISC activity. Activity-induced transcription is a key contributor to synaptic pre-miRNA availability. BDNF activates Satb2, a forebrain specific chromatin remodeling protein, to upregulate transcription of both protein-coding and miRNA-encoding genes (Jaitner et al., 2016). BDNF induces Erk- and CREB-dependent upregulation of miR-132, which represses a GTPase activating protein, prolonging Rac1 activation (Vo et al., 2010; Kawashima et al., 2010; Huang et al., 2012). In addition to inducing repression of specific protein targets, BDNF-induced miRNA modulation can also relieve repression of protein translation. For example, miR-

134 acts post-transcriptionally on plasticity associated enzymes including actin polymerizing lim kinase 1 (Schratt et al., 2006). At baseline, miR-134 represses LIMK1; treatment with BDNF allows LIMK1 to be translated. Similarly, miR-134 represses Ras palmitoylating enzyme DHHC9 in neurons (Chai et al., 2013). The net effect of miR-134 is to suppress dendritic spine size and synaptic plasticity factors (Gao et al., 2010), and it may be upregulated after synaptic activity, perhaps supporting a homeostatic function (Bicker et al., 2014).

Another example of relief of repression downstream of BDNF involves the Let-7 family. This group of 13 coordinately regulated microRNAs is highly abundant in the brain (Roush & Slack, 2008). Deep sequencing indicates that almost half of small RNAs expressed in rat hippocampus belong to the let-7 family (Shinohara et al., 2011; Juhila et al., 2011). Laser-capture dissection experiments indicate that several let-7s may be differentially regulated in the neurite and soma (Kye et al., 2007). Let-7 miRNA levels are rapidly reduced in response to BDNF activity, enabling rapid up-regulation of translation from target mRNAs such as CamKII alpha and Arc (Huang & Ruiz et al., 2012). More comprehensive reviews of miRNA function in synaptic plasticity have been written by Aksoy-Aksel et al. (2014) and McNeill and Van Vactor (2012).

TRBP: a microRNA biogenesis cofactor

TRBP, the Tar RNA binding protein, is a cytoplasmic cofactor to Dicer and aids in processing of pre-miRNAs to mature microRNAs. As its name suggests, this protein was discovered in connection with the HIV genome component Tar

RNA; TRBP overexpression potentiates HIV replication, because TRBP represses the interferon inducing, dsRNA-stimulated protein kinase R (PKR) (reviewed by Daniels and Gatignol, 2012). TRBP can also bind to and inhibit a fellow dsRNA binding protein, the protein activator of PKR (PACT) (Daher et al.,2009). TRBP exerts PKR-independent cellular effects in complex with Dicer, where TRBP is believed to feed pre-miRNAs into the Dicer active site and facilitate RISC loading (Wilson et al., 2015).

Post-translational modifications to TRBP

TRBP is highly regulated in response to signaling, with studies identifying up to ten phosphorylated residues (Kim et al., 2014). Posttranslational modifications govern the protein's stability and affinity for various binding partners; some of these modifications have been shown to mediate changes in miRNA processing.

Phosphorylated TRBP is present in the RISC, and Erk overexpression enhances, while inhibition diminishes, its abundance in this complex (Paroo et al., 2009). A phosphomimic construct, mutated at four serines identified by mass spectrometry, enhances Dicer binding and miRNA maturation (Paroo et al., 2009). Of those four residues (serines 142,152, 283, and 286), two in the C terminus of the protein have subsequently been shown to be substrates of S6 kinase 2, a protein kinase generally activated downstream of mTor. (Warner et al., 2016). The authors of the latter study postulated that concurrent phosphorylation of TRBP by Erk, presumably in the linker region between

double-stranded RNA binding motifs (dsRBMs) 1 and 2, and S6K2 in the C-terminal domain may collaborate to increase TRBP/Dicer binding and miR maturation downstream of the receptor tyrosine kinase for angiopoietin (Warner et al., 2016). Erk phosphorylation also enhances SUMOylation of TRBP, which may contribute to improved RISC formation, and which reduces TRBP ubiquitination and degradation (Chen et al., 2015).

In contrast, TRBP is hyperphosphorylated by JNK during mitosis, a modification independent of Erk activity that does not affect Dicer binding but does enhance binding to, and inhibition of, protein kinase R (Kim et al., 2014). This phosphorylation, independently confirmed in a constitutively active JNK1 setting, can be reduced by S-to-A mutation at serine 142 and abolished by combining S142A and S152A mutations (Nakamura et al., 2015).

The residues in TRBP that are MAPK substrates are incompletely elucidated but, taken together, the data (Paroo et al; Kim et al; Nakamura et al) suggest that serines 142 and 152, located in the linker region between TRBP dsRBM1 and dsRBM2, may be regulated by both JNK and Erk. These kinases are known to share overlapping substrate motifs in other proteins; for example, specific serines in the transcription factors Elk1 and JunD have been observed to be phosphorylated by both JNK and Erk (reviewed by Bogoyevitch and Kobe, 2006).

TRBP phosphorylation regulates its stability and binding partner selection, mediating signaling in various physiological and disease contexts: it promotes HIV infection of T cells (Sanghvi et al., 2011), stress-response signaling (Daniels

& Gatignol, 2012) and obesity (Nakamura et al., 2015), and as has been recently shown, can control microRNA regulation through simultaneous binding to Dicer and lin28a in hippocampal synaptic plasticity (Amen et al., 2017).

Lin28a- a pluripotency-mediating protein

Lin28a is a pluripotency factor critical for numerous developmental and cellular signaling pathways (Jiang & Baltimore, 2016). It represses Dicer processing of the let-7 family of microRNAs (miRNAs) and several related miRNAs by binding to the stem-loop structure of pre-miRNAs. After binding, Lin28a recruits one of two terminal uridyltransferases (TUT4 or TUT7) to pre-let7 miRNAs to reduce availability for Dicer processing (Hagan et al., 2009, Heo et al., 2012, Thornton et al., 2012). Although monouridylation potentiates microRNA biogenesis, polyuridylated miRNAs cannot be processed by Dicer into mature form (Heo et al., 2008). Moreover, the 3'-5' exonuclease DisL32 degrades polyuridylated RNAs preferentially (Chang et al., 2013, Viegas et al., 2015).

Lin28a has been reported to localize in ribonucleoprotein complexes in the cytoplasm including in RNA-processing bodies (P bodies), where it colocalizes with translation-associated proteins such as elongation factors eIF3B and eIF4E and RNA helicase A (Balzer and Moss, 2007; Jin et al., 2011).

While it inhibits let-7 miRNA processing, Lin28a is itself translationally repressed by mature let-7 miRNAs (Rybak et al., 2008). Therefore, Lin28a and let-7 microRNAs form a bistable switch; upregulation of either reduces levels of the other (Viswanathan et al., 2008; Heo et al., 2008; Newman et al., 2008). A

change in switch state from high Lin28a protein level to high mature let-7 microRNA level is associated with the transition from stem or progenitor cell to adult tissue, and generally occurs at the late embryonic stage (Thomson et al., 2004; Wulczyn et al., 2007; Sempere et al., 2004).

Numerous biochemical studies have investigated the functional domains of Lin28a and the precise mechanism by which they recognize and inhibit processing of the protein's miRNA precursor targets. The protein has two conserved dsRNA binding domains: a cold-shock domain (CSD), from aa 39-112; and an RNA-binding CCHC zinc knuckle domain (ZKD), from aa 136-176 (figure 1.2b). A crystal structure of truncated Lin28a in complex with a pri-let-7 shows interfaces at the terminal loop of the microRNA, with the Lin28a CSD inserted into the precursor loop and the ZKD binding double-stranded sequence ancillary to the terminal loop (Nam et al., 2008). Subsequent work demonstrated that lin28a binding specificity is driven by a GGAG motif in the terminal loop of pre-miRNAs in the let-7 family, and also substrates such as miR-143 and miR-107 (Heo et al., 2009). Both Lin28 proteins contain a cold-shock domain (CSD) and two CCHC-type zinc-finger domains that bind respectively to the GNGAY consensus sequence (Y, pyrimidine; N, any base) in the let-7 preE loop and a conserved GGAG motif near the 3' end of the let-7 preE bulge (Ali et al., 2012; Heo et al., 2009; Loughlin et al., 2012; Mayr et al., 2012; Nam et al., 2011; Piskounova et al., 2008; Wang et al., 2017). Truncation experiments indicate that either the cold shock domain, or the zinc knuckles in isolation, may suffice to bind to miRNA precursors. Remodeling of the pre-miRNA terminal loop to occlude

Dicer cleaving site is mediated by the lin28 CSD, which may also drive multimerization of lin28 on pre-let-7s (Mayr et al., 2012; Desjardins et al., 2014). On the other hand the ZKD can also bind pre-miRNAs, with affinity partly driven by miRNA identity (Nowak et al., 2017). Expressed in isolation, the zinc knuckles are adequate to bind a microRNA stem-loop, recruit TUT4, and mediate oligouridylation (Wang et al., 2017)

Lin28a can bind to mRNA as well as microRNA, targeting a GGAGA motif in mRNAs; Lin28a binding is believed to mediate mRNA splicing and translation (Wilbert et al., 2012; Lei et al., 2012). Lin28 binding has been reported to directly enhance translation of target genes by driving their inclusion in polysomes (Jin et al., 2011; Peng et al., 2011; Polesskaya et al., 2008), as well as to suppress translation by an unknown mechanism (Cho et al. 2012). Its reported mRNA targets include its own mRNA and numerous fellow RNA binding proteins, signaling proteins, and cyclins in progenitor cells of various tissues (Hafner et al., 2013; Polesskaya et al., 2008; Xu et al., 2009). Relative contributions of lin28a mRNA binding and pre-miRNA binding to the total physiological effect of lin28a are debated.

Moreover, a recent publication adds a layer of complexity by demonstrating that Lin28a has the capability to bind dsDNA, and might bind to single-stranded promoters with a purine-rich motif, distinct from but similar to its GA-rich RNA targets, to regulate gene expression (Zeng et al., 2016)

Lin28B: a lin28a paralog with subtly distinct function

Mammalian Lin28a has a homolog, Lin28B. The two proteins share high sequence similarity especially from the start of the CSD to the ZKD terminus, with nonhomologous sequence concentrated at the N and C termini. The proteins differ in primary function: Lin28B tends to act in the nucleus, by sequestering pri-let-7 miRNAs far from the microprocessor complex, within the nucleolus (Piskounova et al., 2011). However, describing lin28a as cytoplasmic and B as nuclear would be an oversimplification. Both proteins can be found in both compartments, and each binds, albeit with varying affinity, to both pri-let-7s and pre-let-7s (Shyh-Chang & Daley, 2013).

Post-translational modifications to lin28a

Lin28a methylation, phosphorylation and N-acetylation have been reported (Bienvenut et al., 2012; Rigbolt et al., 2011; Van Hoof et al., 2009; Kim et al., 2009). Of these modifications, methylation and phosphorylation have documented effects on protein function.

Lin28a methylation at lysine 135 drives lengthened protein half-life, nucleolar localization, multimerization and a preference for binding pri-let-7s over pre-let-7s (Kim et al., 2014). This modification drives a striking degree of functional overlap between Lin28a and Lin28B. Methylation may extend stem cell pluripotency by tightly controlling let7 generation at the primary miRNA stage. (Kim et al., 2014).

Recent studies have shown that Lin28a can be phosphorylated by Erk kinase at a serine residue in the C terminal unstructured region, a modification

which increases the stability of the protein, whereas a corresponding phosphodeficient mutant is less stable (Tsanov et al., 2017; Liu et al., 2017). While the effects of this phosphorylation event on miRNA and mRNA targets of lin28a remain in dispute, both groups agree that Lin28a phosphorylation is associated with maintenance of pluripotency (Tsanov et al, 2017; Liu et al., 2017).

Lin28a in endogenous and induced pluripotency

Overexpression of Lin28a, with several other pluripotency factors, can drive reprogramming and de-differentiation of adult cells into induced pluripotent stem cells (Yu et al., 2007; Hanna et al., 2009). As a driver of pluripotency, lin28 is also a potent oncogene; aberrant expression of the protein is associated with numerous human malignancies, reviewed by Jiang & Baltimore (2016).

In normally developing mammalian embryos, Lin28a expression is high at very early developmental stages. As noted above, over the course of development, Lin28a protein is reduced to undetectable levels in most adult tissues. Deletion of Lin28a does not abrogate pluripotency, as Lin28a knockout mice can develop past the pluripotent blastocyst stage (Zhu et al., 2010). However, data suggest that the protein may be required for self-renewal of pluripotent cells (Tanabe et al., 2013; Shyh-Chang & Daley, 2013). Forced overexpression of Lin28a delays puberty and drives overgrowth in mice (Zhu et al., 2010).

Lin28a expression remains detectable in the neural tube and neural crest after its expression declines in other cell types (Balzer et al., 2010). Much as described on an organismal level, neural-specific reduction of lin28a yields a smaller brain, while overexpression drives overgrowth (Yang et al., 2015). The protein is required for proliferation of neural progenitor cells (NPCs), and its deletion drives cell cycle exit through target mRNAs (Cimadamore et al., 2013, Yang et al., 2015). Conversely, injury to the mammalian retina promotes transcriptional activation of lin28a, which drives glial proliferation and neurogenesis to promote tissue regeneration (Yao et al., 2016). A few recent publications have demonstrated other roles for lin28a in adult brain tissue.

Lin28a in differentiated tissues: regulation of metabolism

The lin28a/let-7 axis is increasingly recognized as a regulator of growth and metabolism. In general, higher levels of lin28a improve glucose tolerance and insulin signaling, and vice versa. Inducible overexpression of lin28a in the skeletal muscle of transgenic mice improves glucose tolerance and lean body mass through derepression of various genes in the PI3K/mTor signaling pathway (Zhu et al., 2011). Meanwhile, mice overexpressing let-7 exhibit diminished glucose-induced pancreatic insulin secretion driven by numerous let-7 target genes in the insulin response signaling pathway (Frost et al., 2011, Shinoda et al., 2013). Lin28a protein level is significantly depressed in induced stem cells derived from obese adipocyte tissues compared to healthy controls; overexpressing lin28a can rescue glucose tolerance, reducing let-7 levels and

inflammatory signaling in these stem cells (Perez et al., 2013). In brain tissue, hypothalamic Lin28a regulates metabolism (Kim et al., 2017). Overall, there are a number of interesting hints that the receptor tyrosine kinase (Rtk) that recognizes insulin may upregulate lin28a through the same paths as the Rtk recognizing BDNF.

TRBP/lin28a binding- a case of signal responsive miRNA changes

Recently, it was demonstrated that TRBP binds to and stabilizes lin28a and Dicer concurrently in a manner enhanced by Erk activity and TRBP phosphorylation (Amen et al., 2017). This interaction acts as a selective force in signal-responsive miRNA biogenesis, whereby stabilized lin28a reduces the level of let-7 miRNAs while phospho-TRBP, in complex with Dicer, enhances maturation of a majority of miRNAs. (Amen et al., 2017). Circumstantial evidence suggests that this interaction may occur in neurons, and that downregulation of let-7 microRNAs may provide a mechanism for local translation changes downstream of BDNF (Daniel Pham, unpublished). Moreover, a species believed to represent lin28a increases by Western blot in response to receptor tyrosine kinase-mediated growth factors in various cell lines and tissue types, hinting at a widespread role for this protein/protein interaction in growth regulation in various contexts (Amen et al., 2017). The recent demonstration of Lin28a phosphorylation by Erk opens the possibility that signaling downstream of growth factors may also affect Lin28a directly, in addition to being transduced through TRBP.

Figures and legends.

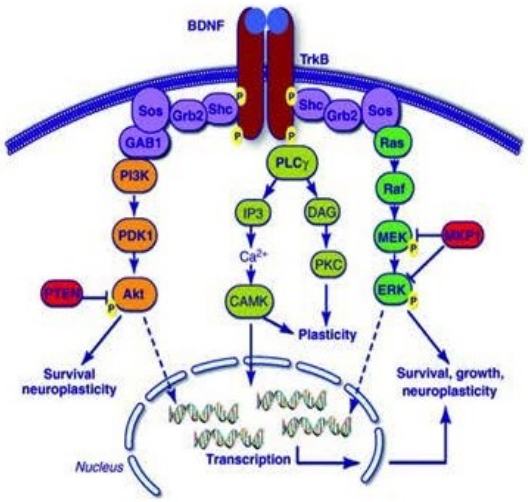

Figure 1.1 Signaling through BDNF. Reproduced by permission from Duman and Valeti, *Trends in Neurosciences* 35(1), 2012 (doi: 10.1016/j.tins.2011.11.004). Copyright Cell Press 2012.

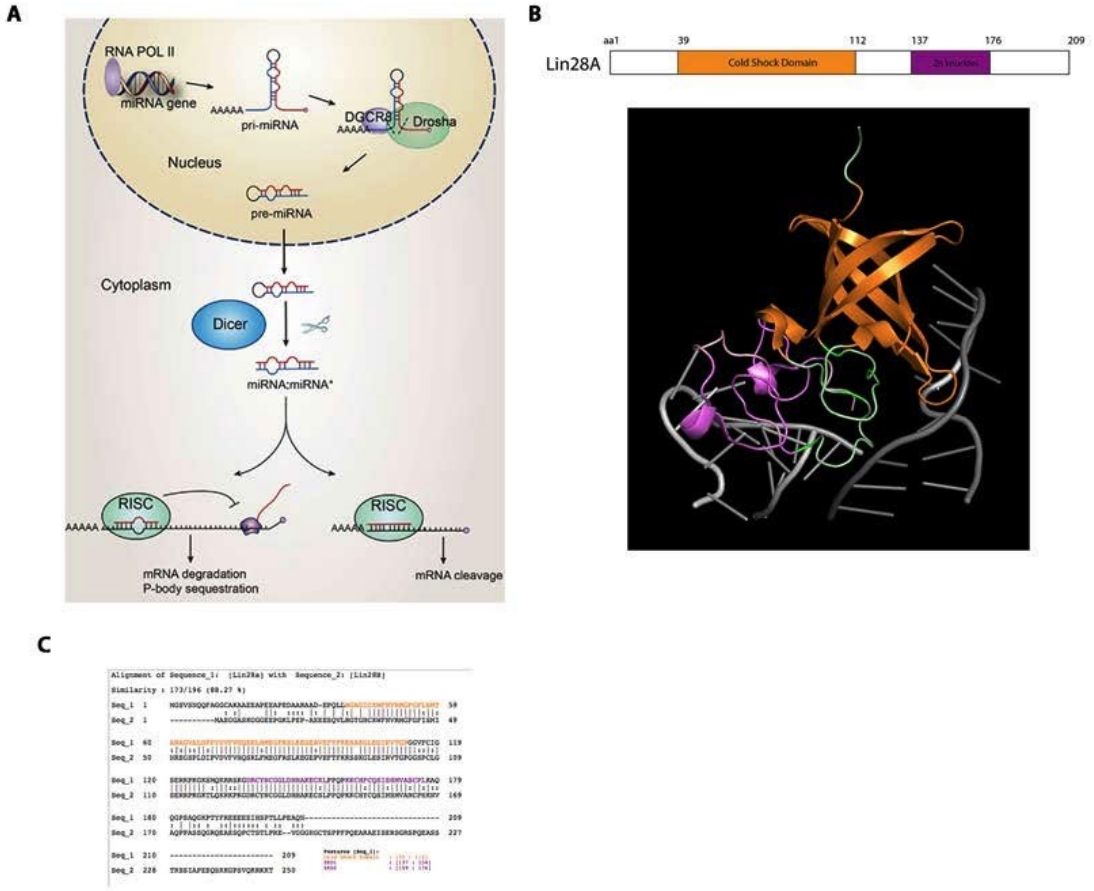

Figure 1.2. MicroRNA biogenesis factors. (A) MicroRNA biogenesis schematic. Reprinted under a Creative Commons license from Barca-Mayo and Lu (2012) Fine-tuning oligodendrocyte development by microRNAs. *Front. Neurosci* 6:13. Doi: 10.3389/fnins.2012.00013. (B) Linear schematic of Lin28a protein, with crystal structure showing cold shock domain (orange) and zinc knuckles (violet) binding to two separate dsRNA structures (gray). (Adapted from PDB 5UDZ (Wang et al. *Cell Reports* 18 2664-2675 (2017)) (C) Alignment of Lin28a (top) with Lin28B (bottom), showing high sequence identity within structured domains and minimal alignment at N and C termini.

Chapter 2. Characterization and dynamic visualization of Lin28a interaction with TRBP

Abstract:

Intracellular levels of the RNA-binding protein and pluripotency factor, Lin28a, are tightly controlled to govern cellular and organismal growth. Lin28a is extensively regulated at the post-transcriptional level, and can undergo mitogen-activated protein kinase (MAPK)-mediated elevation from low basal levels in differentiated cells by phosphorylation-dependent stabilizing interaction with the RNA-silencing factor HIV TAR-RNA-binding protein (TRBP). However, molecular and spatio-temporal details of this critical control mechanism remained unknown. In this work, we dissect the interacting regions of Lin28a and TRBP proteins and develop a sensor to visualize this interaction. We identify truncated domains of Lin28a and of TRBP that are sufficient to support co-association and mutual elevation of protein levels, and a requirement for MAPK-dependent phosphorylation of TRBP at putative ERK-target serine 152 in mediating increase of Lin28a protein by TRBP. The phosphorylation-dependent association of Lin28a and TRBP truncated constructs is leveraged to develop a FRET-based sensor for dynamic monitoring of Lin28a and TRBP interaction. We demonstrate response of this FRET sensor to growth factor stimulation in living cells, with coimaging of Erk activation to achieve further understanding of the role of MAPK signaling in Lin28a regulation.

Introduction:

Lin28a is a pluripotency-associated RNA-binding protein that exerts post-transcriptional effects to govern many developmental and cellular signaling pathways (Jiang et al., 2016). Lin28a promotes pro-growth gene expression in part by repressing maturation of the Let-7 family of microRNAs (miRNAs), and undergoes reciprocal translational repression by Let-7 miRNAs (Rybak et al., 2008). Lin28a also controls gene expression through regulation of mRNA translation (Cho et al., 2012). Appropriate control of Lin28a protein levels is necessary for correct organismal development. Mice deficient in Lin28a suffer perinatal lethality (Shinoda et al., 2013). Conversely, Lin28a overexpression can lead to abnormal growth and metabolic phenotypes (Zhu et al., 2011, Shyh-Chang et al., 2011), and Lin28a is upregulated in numerous human cancers (Viswanathan et al., 2009, Shyh-Chang & Daley, 2013). Despite a growing appreciation for the necessity of tight control of Lin28a in producing appropriate gene expression programs, the signaling that regulates dynamic changes in Lin28a protein levels remains incompletely understood.

Recently, we reported rapid signal-dependent induction of Lin28a through post-translational regulation of Lin28a protein stability. MAPK pathway activation was shown to enhance phosphorylation and binding of the Dicer cofactor, TRBP, as well as Dicer itself to Lin28a in a stabilizing interaction (Amen et al., 2017). This complex exerts selectivity in miRNA biogenesis, allowing Lin28a to reduce the level of Let-7 miRNAs while Dicer enhances maturation of many miRNAs not

targeted by Lin28 (Huang & Ruiz et al., 2012). A Lin28a/TRBP/Dicer protein complex was described initially in cultured neurons, but MAPK-dependent TRBP phosphorylation and Lin28a elevation were also observed downstream of trophic factors in other primary cell types, indicating a widespread role for this interaction in regulating growth responses (Amen et al., 2017). However, molecular details of the Lin28a/TRBP interaction, including its timescale and spatial distribution in cells, were relatively unexplored. In this work we characterize the biology of Lin28a and TRBP interacting domains. We identify a TRBP phosphorylation site crucial for signal responsive interaction with Lin28a and leverage this characterization to develop a genetically-encoded optical sensor for Lin28a/TRBP binding, allowing quantification and spatiotemporal visualization of Lin28a/TRBP binding in living cells.

Results:

A TRBP truncation sufficient to interact with full-length Lin28a.

To investigate TRBP-induced elevation of Lin28a protein levels, we first identified the region of TRBP required for this response. Truncation mutants of TRBP, TRBP A (1 – 105), TRBP B (98 – 234), TRBP AB (1 – 234) and TRBP C (228 – 366) (Figure 1A), developed by the Gatignol lab (Daher et al., 2009), were tagged with the myc epitope. When co-expressed in HEK 293T cells with flag-tagged lin28a (FL-Lin28a), TRBP-A and TRBP-B both elevated FL-Lin28a, while TRBP-C had no effect. (Figure 1B-C). Expression of TRBP-C was low, even with high DNA transfections (Figure S1A). Dose titration showed that elevation of FL-

Lin28a protein by TRBP-A and TRBP-B was most readily detected at low FL-Lin28a expression levels (Figure S1B-C). Expressed TRBP-A and TRBP-B could also elevate levels of endogenous TRBP protein (Figure 1D), in line with a previous demonstration that dsRNA binding motifs (dsRBMs) in these two truncations mediate TRBP dimerization (Kok et al., 2007). To distinguish effects on Lin28a elevation due to the TRBP truncation alone from effects that might result from heterodimerization of a TRBP truncation with endogenous TRBP, we next carried out experiments in TRBP knockout cells.

Coexpression of TRBP-A and TRBP-B with FL-Lin28a in mouse tail epithelial fibroblast cells (TEFs) lacking endogenous murine TRBP (*Tarbp2* KO) (Daher et al., 2009) revealed that TRBP-B, but not TRBP-A, could elevate FL-Lin28a levels; TRBP-B increased FL-Lin28a comparably to full length TRBP expression (Figure 1E-G). Across a range of expression levels in TRBP KO TEFs, full length TRBP and the TRBP-B truncation construct produced approximately linear FL-Lin28a protein elevations, while no increase in FL-Lin28a was observed with TRBP-A (Figure 1G). These results strongly suggested that TRBP-B retained the capacity to interact with Lin28a, while effects of TRBP-A were absent when endogenous full-length TRBP could not be recruited.

In previous work, we demonstrated that TRBP can directly bind Lin28a in a stabilizing complex (Amen et al., 2017). Thus, we next compared the association of truncations TRBP-A, TRBP-B, and TRBP-AB with FL-lin28a. Immunoprecipitation of FL-lin28a from 293T cells showed that TRBP-AB coimmunoprecipitated with FL-Lin28a, as did TRBP-B (albeit more weakly), while

TRBP-A did not coimmunoprecipitate with FL-Lin28a (Figure 1H). Collectively, these results are consistent with binding and increase of Lin28a by the TRBP-B segment of TRBP, but not by the N-terminal or C-terminal segments TRBP-A and C.

TRBP phosphorylation at S152 potentiates lin28a elevation

TRBP phosphorylation has been shown to increase its stability (Chen et al., 2015) and enhance binding to Dicer and other binding partners (Paroo et al., 2009, Kim et al., 2015). In addition, we previously showed that a phosphomimic TRBP mutant, with four serines mutated to aspartates, exhibited enhanced binding to Lin28a in purified protein interactions (Amen et al., 2017). These findings implicated MAPK pathway-mediated phosphorylation of TRBP in Lin28a binding, without indicating which of the four serine residues was involved. We identified an 'FXF' putative Erk docking motif (Gonzalez et al., 1991) within TRBP-B, beginning at aa 112. Two of the serines mutated in the full-length phosphomimic construct, S142 and S152, are present in TRBP-B; both serines are candidates for proline-directed kinase phosphorylation, but S152 is a closer match to an Erk phosphorylation consensus sequence (Figure 2a, PXSP) (Jacobs et al., 1999).

Immunoblot of lysates from 293T cells expressing myc-TRBP-B revealed a multi-banding pattern between 20 and 25 kDa when probed with an antibody raised and purified against phospho-S152 TRBP (Figure S2A). Consistently, exposure of myc-TRBP-B lysates to lambda phosphatase treatment collapsed

the myc-reactive bands to a singlet at the expected molecular weight of TRBP-B (Figure 2B). Phorbol 12-myristate 13-acetate (PMA) increases TRBP phosphorylation through the MAPK signaling cascade (Paroo et al., 2009). Treating 293T cells expressing myc-TRBP-B with PMA led to an increase in phospho-S152 TRBP immunoreactivity, which was reduced in lysates from cells treated with MAPK/Erk kinase (MEK) inhibitor U0126 (Figure 2C). We conclude that TRBP-B can be phosphorylated within living cells in a MEK dependent manner. To evaluate the role of this TRBP phosphorylation site in producing Lin28a elevation, we immunoblotted lysates from 293T cells which were co-expressing FL-Lin28a and myc-TRBP-B, and treated with either vehicle control, PMA, or PMA plus U0126. Immunoblot showed that FL-Lin28a protein levels were increased by myc-TRBP-B expression, and that PMA treatment further enhanced Lin28a elevation in a manner blocked by U0126 (Figure 2C-D).

We next conducted experiments in TRBP KO TEFs to evaluate the role of the putative ERK phosphorylation site TRBP S152 in conferring stimulus-mediated Lin28a elevation by TRBP-B. A phosphomutant myc-TRBP-B with S152 was mutated to alanine was generated; reactivity of the TRBP-B band with anti-phospho-TRBP antibody was abolished in cells expressing TRBP-B S152A (Figure 2E,S2C). In TRBP KO TEFs co-expressing FL-Lin28a and either myc-TRBP-B or phosphomutant myc-TRBP-B-S152A (at similar levels, Figure S2B), TRBP-B or TRBP-B S152A expression could each produce some basal Lin28a elevation, but cells expressing TRBP-B S152A were unable to respond to PMA (Figure 2F). PMA produced a modest Lin28a induction in the absence of TRBP-

B expression, an effect which might be due to direct Lin28a phosphorylation (Tsanov et al., 2017, Liu et al., 2017) or an alternative unknown interacting protein. Collectively, these experiments indicate that the TRBP-B region is sufficient to bind and elevate Lin28a protein levels, and support a role for TRBP S152 in transducing MAPK pathway activation through TRBP to regulate Lin28a.

Lin28a-3, a truncation sufficient to bind to TRBP

To address which region of Lin28a protein interacted with TRBP, we generated three domain-based truncations of Lin28a (Figure 3A). Since Lin28b, a paralog with 86% amino acid identity between Lin28A amino acid 19 and 177, fails to bind to TRBP (Amen et al., 2017), we reasoned that amino acid sequences unique to Lin28a at the amino- or the carboxyl- terminus of the protein might participate in TRBP interaction. Truncations were designed to correspond to functional domains of Lin28a revealed by its crystal structure (Nam et al., 2011, Mayr et al., 2013). Lin28a-1, aa 1-112, included the structurally uncharacterized N-terminus and the cold-shock domain (CSD). Lin28a-2, aa 75-154, encompassed half of the CSD, extending to the end of the CCHC Zn knuckles. Lin28a-3 began at the N-terminus of the CCHC, extending to the structurally uncharacterized C-terminus of the protein (Figure 3A).

Full-length FL-Lin28a and FL-Lin28a-3 levels were each elevated above baseline by myc TRBP co-expression in 293T cells (Figure 3B-C). In some experimental replicates, we observed mild increases in FL-Lin28a-1 by TRBP. We tested whether, like full length FL-Lin28a, either FL-Lin28a-1 or FL-Lin28a-3

could be elevated by treatment with PMA (24 hours) in 293T cells co-expressing TRBP-B. FL-Lin28a-1 was not significantly changed either with TRBP-B alone or with TRBP-B plus PMA, while FL-Lin28a-3 levels were robustly increased by TRBP-B expression and further enhanced by PMA treatment (Figure 3E,F).

Lin28a-3 binds to TRBP-B in a phosphorylation-inducible manner

The identification of Lin28a-3 and TRBP-B as interacting truncated proteins which reproduce the induction observed with full length TRBP and Lin28a proteins, presented an opportunity to create a physiological sensor for this pathway. We assayed FRET efficiency between TRBP constructs tagged with the CFP variant, Cerulean, and Lin28a constructs tagged with a circular permutation of the Venus YFP, cpVenusE172. FRET was measured in living 293T cells by bleaching the FRET acceptor, YFP, and measuring dequenching of the donor, CFP. As a benchmark for high FRET efficiency in our imaging system, we used a FRET sensor for calmodulin (Figure S3A) (Romoser et al., 1997). We confirmed YFP bleaching to 75% or greater reduction of signal in each cell (Figure S3B-D).

We tested full-length TRBP and each truncation against a panel of YFP-tagged Lin28a constructs coexpressed in 293T cells. When coexpressed with full-length TRBP, both Lin28a-1 and Lin28a-3 showed non-zero FRET efficiency, indicative of significant interaction (Figure 4A). In congruence with our previous findings, FRET efficiency of Lin28a-3-YFP with CFP-TRBP was highest, followed by Lin28a-1-YFP, with no FRET between Lin28a-2-YFP and CFP-TRBP (Figure

4A). Consistent with its failure to elevate Lin28a protein levels, TRBP-A displayed no FRET-detectable interaction with any Lin28a-YFP truncation (Figure 4B). In contrast, TRBP-B showed significant CFP recovery when coexpressed with Lin28a-1-YFP, Lin28a-3-YFP, or full length Lin28a-YFP (Figure 4C). We noted that full length Lin28a, which is capable of direct binding to TRBP (Amen et al., 2017), did not show significant CFP recovery after photobleaching (Figure 4A). This is consistent with a risk of false negative results from FRET analyses based on fluorophore orientation (Miyawaki, 2011). Based on these results, we concluded that TRBP-B can interact with Lin28a-3, and also to a lesser degree with Lin28a-1. Further, observed FRET efficiency of the Lin28a-3-YFP and CFP-TRBP-B was higher than that between full length Lin28a and TRBP, suggesting that the truncated constructs produce a preferred conformation for a FRET biosensor.

To determine whether TRBP binding by Lin28a-1 or Lin28a-3 could be increased by phosphorylation, we treated 293T cells expressing CFP-TRBP-B and either Lin28a-1-YFP or Lin28a-3-YFP with either epidermal growth factor (EGF, a MAPK pathway activator) or vehicle and measured donor dequenching 60 minutes after treatment (Figure 4D). FRET between CFP-TRBP-B and Lin28a-3-YFP increased significantly after EGF treatment (Figure 4D), consistent with the stimulus-dependent increase in protein levels observed in Figure 3E and F. In contrast, EGF treatment did not alter FRET efficiency of Lin28a-1-YFP and CFP-TRBP-B. Notably, there was no detectable FRET between Lin28a-3-YFP and the S152A phosphomutant CFP-TRBP-B S152A, indicating a critical role for

this serine residue in interaction of the Lin28a/TRBP FRET sensor (Figure 4E). In cells treated with EGF for variable time prior to acceptor bleaching, CFP-TRBP-B and Lin28a-3-YFP demonstrated a time-dependent increase in FRET with a maximal plateau by 60-90 minutes (Figure 4E). This corresponded with a similar time-dependent increase in the ratio of phosphorylated TRBP-B to total myc-TRBP-B observed by immunoblot after EGF treatment (Figure 4F-G).

Optimization and validation of a sensor for Lin28a/TRBP binding

Based on the observation that FRET between TRBP-B and Lin28a-3 was increased within 90 minutes by EGF, and absent with phosphomutant TRBP-B, we performed time-lapse experiments to characterize the stimulation kinetics in more detail. We expressed CFP-TRBP-B and Lin28a-3-YFP, in 293T cells and calculated the ratio of sensitized YFP fluorescence emission, determined using the NFRET formula, to CFP fluorescence (Xia & Liu, 2001). Baseline emission ratios were measured in individual cells for ten minutes, followed by imaging for thirty-five minutes after EGF treatment. Under these conditions, EGF induced a modest average change in NFRET (Figure 5A,B, “Cer/E172”), indicating that further optimization would be required to generate a more useful sensor for TRBP-Lin28a interaction. To enhance the dynamic range of the sensor, we tested a panel of FRET pairs, a strategy that has improved previous sensors (Zhou et al., 2015) (Figure 5A). Optimization resulted in a marked improvement, with the new FRET pair showing higher average response to EGF (Figure 5B, “Cer3/L194”). We tested the dependence of the Cer3/L194 Lin28a/TRBP FRET

sensor on MEK activity. Consistent with previous Lin28a/TRBP interactions, MEK inhibition with U0126 (30 min) blocked EGF-induced NFRET increases, while 293T cells pretreated with vehicle retained an EGF-stimulated increase in NFRET (Figure 5C).

To investigate the temporal relationship between Erk activation and Lin28a/TRBP binding, we co-expressed an intensitometric Erk activity sensor (EKAR) based on dimerization dependent RFP (Ding et al., 2015) with the optimized Lin28a/TRBP sensor. The spectral separation between Cerulean3/Venus and RFP permitted us to monitor signal-induced changes in single cells at these two different steps within the EGF response pathway. Representative images of cells before and for 80 minutes after EGF treatment are shown in Figure 5D. Consistent with our earlier demonstration that S152A TRBP-B failed to show detectable FRET with Lin28a-3, we observed that NFRET/CFP ratio between the phosphomutant and Lin28a-3 did not increase after EGF treatment, even though EKAR activity indicated rapidly peaking Erk activation (Figure 5E). In contrast, 293T cells expressing the sensor using WT-TRBP-B demonstrated NFRET response to EGF (Figure 5F). Erk activity reached a plateau within 15 minutes of EGF on average, and remained at peak activity for the duration of imaging (Figure 5F, red curve). The NFRET signal from the optimized Lin28a/TRBP sensor increased more gradually, showing slower kinetics than Erk activity (Figure 5F, black curve). This slower Lin28a/TRBP FRET response compared to EKAR was reproduced in cells treated with PMA (Figure S5A-B). We noted that cells with stronger EKAR response also showed

greater increases in Lin28a/TRBP NFRET, and analyzed the correlation between response magnitudes of the two signals. Comparing the increase in EKAR intensity at 30 minutes of EGF, to the increase of NFRET at the same timepoint, we observed a positive correlation between these two readouts (Figure 5G). We conclude that this sensor is a reliable tool for imaging ongoing changes in Lin28a/TRBP binding in real time within cells, and enables visualization of variability and temporal dynamics in signal-dependent events that regulate miRNA biogenesis.

Use of the sensor in neurons.

We were interested in the mechanism for BDNF-induced let-7 downregulation, and wondered whether it might reflect stabilization of Lin28a through localized phosphorylation and TRBP binding (Huang & Ruiz et al, Amen et al). Measuring FRET based on acceptor photobleaching would allow us to image lin28a/TRBP binding at high resolution in these dendritic structures. We expressed the sensor and mCherry in hippocampal pyramidal neurons (2.6a) and selected regions of interest in spiny apical dendrites. By confocally imaging the recovery of the FRET acceptor, TRBP-B, in hippocampal dendrites treated with BDNF for 30 minutes, we observed no higher FRET efficiency on average in the WT than the S152A sensor even though EKAR, a positive control, showed fairly high FRET efficiency (2.6b). We hypothesized that this might be driven by high basal differences in expression level between neurons, and so tried a different approach, observing FRET efficiency in paired dendrites from the same neuron

before and after 30 minutes of EGF treatment. In one cell out of four examined expressing the WT sensor, FRET efficiency increased approximately sixfold. In the aggregate, however, no significant difference was observed between FRET efficiency before and after treatment in cells expressing either the WT or S152A sensor. The EKAR positive control showed a significant FRET effect, indicating that BDNF treatment was effective and imaging conditions were appropriate for observing a change in FRET (2.6c).

Unimolecular sensor cloning and validation

Given that binding between overexpressed lin28a and endogenous TRBP has been observed in hippocampal neurons (Amen et al., 2017), we hypothesized that the null FRET result in these cells might result from our specific experimental conditions. In particular, low FRET could be partly driven by differences in expression and localization of the two sensor components. The CFP-tagged TRBP-B component, especially, reached distal dendrites and dendritic spines at much lower efficiency than the YFP-tagged lin28a-3 component (figure 2.6a). To drive congruent localization, we generated a unimolecular version of the lin28a/TRBP sensor. By Western blot, we observed an increase in phosphorylation of the unimolecular sensor after EGF treatment (figure 2.6d). By confocal measurement of FRET efficiency in untreated or EGF-treated HEK 293T cells, the unimolecular sensor showed a smaller dynamic range, compared to the bimolecular sensor (figure 2.6e). Higher basal FRET and lower absolute changes in response to treatment are expected from a transition

from bimolecular to intramolecular FRET sensor format; see chapter 4. Validation of the unimolecular sensor in non-neuronal cells is ongoing.

Discussion

Signal-responsive regulation of miRNA biogenesis factors allows rapid changes to miRNA content in different cellular and signaling contexts (Baek et al., 2008, Selbach et al., 2008). In this work, we dissected a MAPK-dependent mechanism for enhanced binding between two miRNA binding proteins, Lin28a and TRBP, believed to modulate miRNA biogenesis in synaptic plasticity (Huang & Ruiz et al., 2012, Amen et al., 2017). We found that a middle region of TRBP (amino acids 98-234, TRBP-B), containing the second dsRBM, was sufficient to bind and elevate levels of Lin28a protein in a manner indistinguishable from full length TRBP. Expression of another TRBP truncation containing this same middle region (TRBP-AB) also increased Lin28a protein levels (Figure 1E, 1F), while truncations lacking this region did not. Interestingly, the Dicer binding domain of TRBP covers the third dsRBM located at the carboxyl-terminus of TRBP (Daniels et al., 2009, Wilson et al., 2015), perhaps enabling simultaneous association of full length TRBP with both Dicer and Lin28a as has been previously demonstrated (Amen et al., 2017). A structural model of TRBP in complex with Dicer (Wilson et al., 2015) supports the premise that the TRBP-B region may remain available to interact with other binding partners, such as Lin28a, when TRBP is bound to Dicer.

Of the three domain-based Lin28a truncations tested only Lin28a-3, which begins at the CCHC zinc knuckles and terminates at the C terminus of the protein, exhibited elevated protein levels when co-expressed with full length TRBP or with TRBP-B (Figure 3B, 3D). Further, only the Lin28a-3 truncation exhibited signal-induced elevation in cells co-expressing TRBP-B. While FRET pairs containing either the amino-terminal Lin28a truncation (Lin28a-1) or Lin28a-3 with TRBP-B exhibited FRET, FRET with Lin28a-3 was strongest FRET at baseline and capable of stimulus-mediated FRET increase (Figure 4). Low basal FRET between Lin28a-1 and TRBP-B could occur due to a secondary interface between the two proteins. These data suggest that the C terminal Lin28a-3 truncation contains a minimal unit for signal-inducible binding to TRBP. Since full length Lin28a can co-associate with TRBP, while the highly homologous Lin28b does not, (Amen et al. 2017), we suspected that the signal-inducible binding region of Lin28a might share scant homology with Lin28b; this is true for the C-terminal ~20 amino acids of Lin28a-3.

We identified a role for TRBP phosphorylation at serine 152, an ERK consensus site proximal to a putative ERK docking site, in enhancing Lin28a interactions after cellular MAPK pathway activation with EGF or PMA. While phospho-mutant TRBP-B S152A remained able to stabilize full-length Lin28a over baseline (Figure 2d,f), it was unable to participate in signal-enhanced elevation of Lin28a protein or FRET efficiency. Likewise, a full length phospho-mutant TRBP, with 4 S-to-A mutations including S152A, retains a weakened basal co-association with full length Lin28a (Amen et al., 2017). These findings

highlight a role for TRBP S152 in signal-dependent enhancement of TRBP-Lin28a interactions and induction of Lin28a protein. The dsRBMs of TRBP, including the motif within TRBP-B, participate in binding to other proteins, most notably PACT and PKR (Daher et al., 2001, Laraki et al., 2008), and could also play a role in basal binding to Lin28a.

The Lin28a/TRBP FRET sensor leverages the utility of FRET imaging approaches for probing complex protein/protein interactions to provide spatiotemporal information about specific binding interactions. We observed that FRET signal, indicative of Lin28a and TRBP binding, exhibited slower kinetics relative to Erk phosphorylation read out from the EKAR sensor. We did not find a condition that induced return of the FRET signal to baseline levels, suggesting that signal-induced binding of sensor may persist despite dephosphorylation, or that the truncation constructs included in the sensor lack a sequence involved in dissociation or dephosphorylation. The TRBP literature implicates multiple proline-dependent MAPKs, chiefly Erk and JNK, in TRBP regulation (Warner et al., 2016, Chen et al., 2015; Kim et al., 2014), including additional residues within TRBP-B. This FRET sensor may be of future use in probing the function of these phosphoregulatory sites, as well as investigation of compartmentalized TRBP and Lin28a interactions in a variety of physiological contexts. For example, both TRBP and Lin28a have roles in protein translation and silencing in the peri-endoplasmic reticulum region (Stalder et al., 2013, Cho et al. 2012).

We had hoped that the sensor could be used to gain spatio-temporal information regarding TRBP interaction with Lin28a occurring downstream of

neurotrophins, which may exert effects on synaptic plasticity and protein synthesis in a variety of neuronal compartments. However, unpublished data establishing Lin28a upregulation in neurons have been difficult to validate, and preliminary experiments with the sensor suggest that, if TRBP/Lin28a interaction occurs in neurons, it is comparatively weak.

Materials & Methods

Cloning

TRBP truncations (as published (Daher et al., 2001) were N-terminally tagged with myc (MEEQKLISEEDL), or fluorescent proteins Cerulean (Rizzo et al., 2004), Cerulean-3 (Markwadt et al., 2011), or ECFP (Llopis et al., 1998). Lin28a truncations were derived from FL-Lin28a (Amen et al. 2017) by PCR and tagged with flag (DLYDDDKD) at the N terminus or YFP variants Venus (Nagai et al 2002), Citrine (Griesbeck et al., 2001), cpVenus-E172 and cpVenus-L194 (Nagai et al 2004) at the C terminus. Phosphomimic and phosphomutant versions of all TRBP and Lin28a constructs were derived from wild-type versions of these constructs, using a QuickChange kit (Agilent) per manufacturer protocols. EKAR ratiometric Erk sensor was a gift from R. Campbell (Addgene plasmid #60974).

Cell culture

HEK 293T cells were cultured and transfected as described (Amen et al., 2017). When multiple truncations of the same protein were expressed for the same experiment, transfection levels were optimized to equalize affinity tag level in lysates from different truncations. Total DNA transfected was equalized between conditions using empty pcDNA vector. Mouse tail epithelial fibroblast cells (TEFs) lacking endogenous murine TRBP (*Tarbp2* KO) (gift of A.Gatignol, (Daher et al., 2009)) were cultured in DMEM with 10% FBS supplemented with penicillin and streptomycin. Cells were seeded at 15,000 cells per well in 24-well

plates, followed by lipofectamine LTX Plus transfection per manufacturer protocol.

Immunoblotting

Cultured cells were washed in cold PBS and harvested on ice with lysis buffer (50 mM HEPES, 150 mM NaCl, 10%Glycerol, 1 mM EDTA, 1% Triton X-100, 0.2% SDS) plus protease inhibitor cocktail (Roche 11836170001), and phosphataseinhibitors (sodium orthovanadate 0.2 mM, sodium pyrophosphate 1 mM). Protein concentration was determined by Bicinchoninic acid (BCA) assay and equal protein amounts resolved on SDS-PAGE gels and electrotransferred to PVDF membrane. Membrane was blocked with 5% BSA in Tris-buffered saline tween 20 (TBST 0.1%) for 1-3 hr and probed with primary antibodies: c-Myc (Lifetech 132500), FLAG (Sigma M2, F3165) TRBP (Abcam ab72110,or Proteintech 15753-1-AP), Phospho-TRBP (custom), Hsc70 (Santa Cruz sc7298) All immunoblots were scanned and quantified without image adjustment. For representative image figures, image levels were uniformly and minimally adjusted for visual clarity in some instances.

Immunoprecipitation

For FL-Lin28a co-immunoprecipitation of TRBP and its truncations, mouse anti-flag M2 antibody (Sigma) was adhered to protein G sepharose beads overnight after blocking with 5% BSA for 1 hour. HEK 293T cells coexpressing

the constructs of interest were harvested in coIP lysis buffer (100 mM KCl, 4 mM MgCl2, 10 mM HEPES (pH 7.3), 50 uM ZnCl2, 0.5% NP-40) with protease inhibitor cocktail (Roche), and phosphatase inhibitors (Sigma, phosphatase inhibitor cocktail 2 and 3). Insoluble material was first removed by centrifugation (10,000 g) and lysates pre-cleared by rotation (4 °C, 1 hr) with unblocked sepharose beads. Equal masses of protein in pre-cleared lysates were brought to equal volume, added to flag antibody-coated beads, and rotated (4 °C, 3-4 hr). After washing 3x with coIP wash buffer (150 mM NaCl, 1 mM MgCl2, 50 mM HEPES (pH 7.8), 50 uM ZnCl2, 0.05% NP-40), immunoprecipitated material was eluted at room temperature using 1x flag peptide (Sigma F3290) diluted in coIP wash buffer.

Epifluorescence Imaging:

Live cell fluorescence and FRET imaging were conducted on a Zeiss Axiovert 200M microscope controlled by Metafluor 6.2 software. Cells seeded on poly(L)lysine coated glass-bottom imaging dishes (MatTek Corporation) were incubated at 37 C in Hank's Balanced Salt Solution (HBSS), and imaged at 40x magnification with 50% neutral density filters, illuminated by an arc lamp and captured on a cooled charge coupled device (Photometrics). Fluorescence emission was collected from cyan fluorescent protein (420DF20 excitation filter, 500 ms excitation, 475DF40 emission filter); yellow fluorescent protein (420DF20 excitation for 50 ms, 535df25 emission filter); sensitized YFP emission (CFP

excitation and YFP emission); and red fluorescent protein (568DF55 excitation filter, 50ms, 600DRLP dichroic mirror, 653DF95 emission filter).

For endpoint FRET imaging, cells expressing CFP-tagged TRBP or a truncation and YFP-tagged lin28a or a truncation were serum starved for approximately fifteen minutes in imaging media. Several images were taken to establish a baseline, followed by 90 second, 3 minute and 5 minute illumination at 504 nm to bleach YFP. Images were quantified using MetaFluor 6.2 software (Universal Imaging). FRET efficiency was calculated based on the recovery in background-corrected CFP brightness after YFP bleaching, using the following formula:

$$FRET\ efficiency = 1-F_{da}/F_{d}$$

where F_{da} is the CFP fluorescence observed when both donor and acceptor are active, and F_{d},is the fluorescence observed after YFP photobleaching. To confirm complete photobleaching, percent change in YFP intensity was calculated, using the formula:

$$\%\ photobleaching = [(intensity\ final-intensity\ initial)/intensity\ initial] * 100\%$$

Only dishes with an average reduction of 80% or more in YFP signal were used for FRET efficiency calculation in epifluorescence experiments.

For time-course FRET imaging, cells expressing CFP-tagged TRBP-B with YFP-tagged Lin28a-3 were serum starved (0.5-2 hrs) in imaging media, then imaged every 30 s. CYFRET, CFP, YFP and RFP intensity in each ROI were measured over time using MetaFluor software and, after background subtraction, used to calculate the normalized FRET emission ratio, a measure that adjusts for

expression level and spectral bleedthrough of donor and acceptor fluorophores (Xia & Liu, 2001).

$$NFRET = FRET\ intensity - [YFP\ intensity \times a] - [CFP\ intensity \times b]$$

$$NFRET\ ratio = NFRET/CFP$$

Bleedthrough value “a” was determined using cells expressing only YFP, then imaged in both the CYFRET and YFP channels. “A” was defined as the signal in the YFRET channel as a percent of YFP signal; on this system, the value used was 0.14. Bleedthrough value “b” was calculated using the same approach with CFP alone, and came to 0.32. Representative images shown in figure 5E have had NFRET value calculated using the Image Calculator function in ImageJ to perform the same series of calculations (i.e., mean background subtraction in each channel, followed by subtraction of estimated bleedthrough from CFP and YFP direct channels, applied to CYFRET channel).

Statistical analyses

All quantified data represent mean +/- SEM. Statistical analysis included one-way ANOVA for independent samples with a Bonferroni *post hoc* test, $\alpha = 0.05$, comparing to Lin28a alone or comparable condition. Where noted, two-tailed student’s *t* tests were used for pairwise comparison of untreated and treated conditions (Figure 2C, 2F). Linear regression analysis and slope significance testing were carried out using a Graphpad Prism protocol equivalent to ANCOVA. Before linear regression was performed, independent variables were subjected to a Grubb’s test with $\alpha = 0.05$. The result was used to justify

removing one statistically significant outlier from TRBP-full regression analysis (Figure 1H).

Author Contributions
MKM & JZ conceived of the project and supervised its execution. LO planned and carried out experiments and analyses in fig 1-4, 5a-b, 5e-f. KG carried out experiments in 5c-g, S5D-F, and assisted with image preparation. LO, MKM & JZ wrote the manuscript.

Acknowledgements/Notes
Laboratory of Anne Gatignol (and Aïcha Daher) for TRBP truncation constructs and TRBP KO TEFs; Alexandra Amen for assistance with experimental troubleshooting and stimulating discussions, Sohum Mehta for imaging and data-handling assistance.

Funding: This work was supported by the Braude Foundation, NIH MH098016 and MH109341 (to M.K.M.), by NIH GM111665 (to JZ), by NIH T32 GM007445 supporting LO), and by MH084020 (to the Neuroscience Multiphoton Facility).

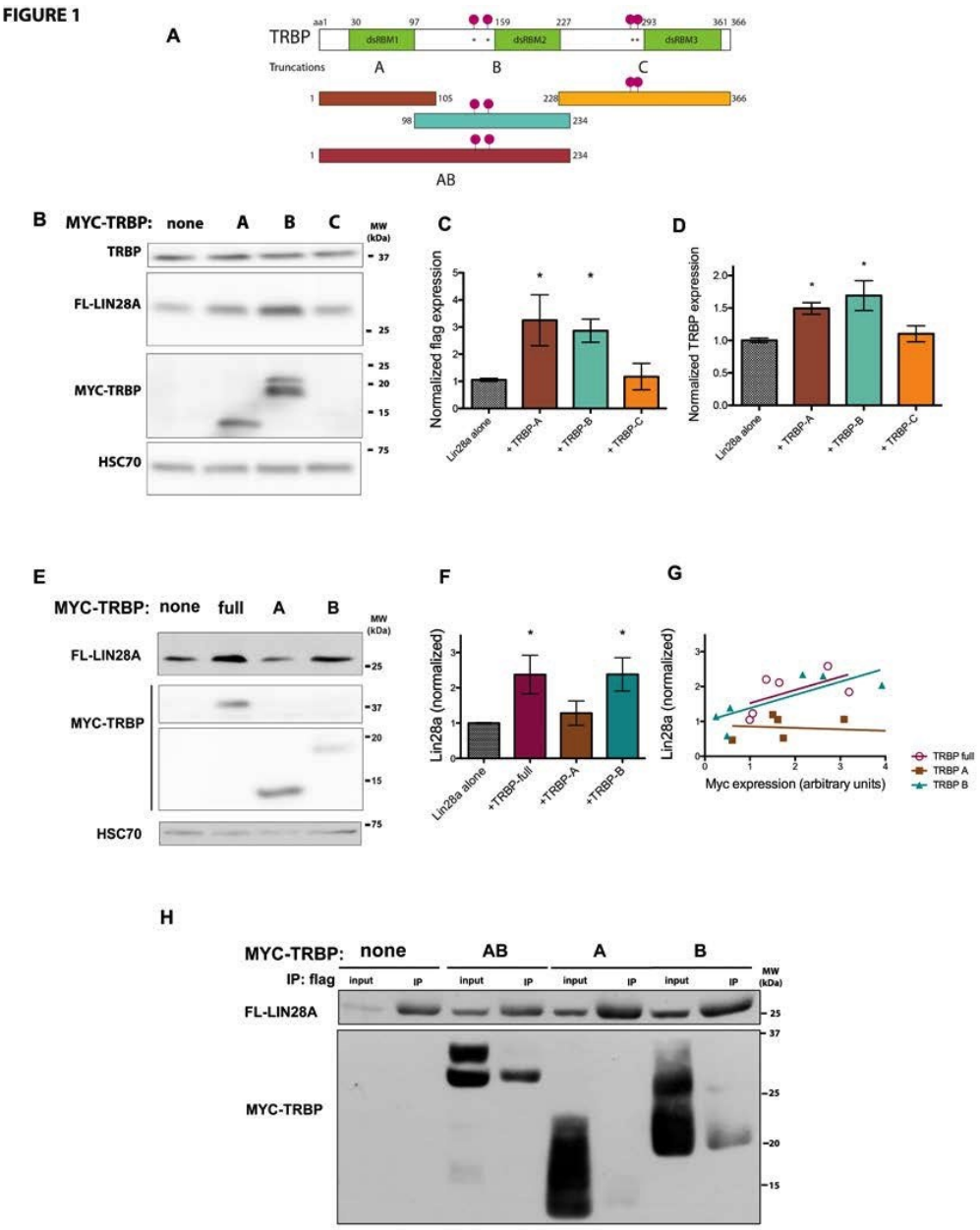

Figure 1. A TRBP truncation sufficient to bind and elevate Lin28a levels. (A) Domain map of TRBP, with truncations TRBP A, B, C and TRBP AB. Phosphorylation sites (pink) as described (Paroo et al., 2009) (B,C) TRBP A and B stabilize FL-Lin28a in 293T cells (n=7-14) (D) Increase in endogenous TRBP level with TRBP truncation vs. Lin28a alone (n=5-8) (E,F) Full length TRBP and TRBP B, but not TRBP A, elevate Lin28a levels from baseline in Tarbp2-/- MEF cells (n=9) (G) Regression analysis on the effect of expression level of full length TRBP, TRBP A, or TRBP B on FL-Lin28a, in Tarbp2-/- cells, plotted relative to FL-Lin28a plus empty vector. The regression line for TRBP full has a correlation coefficient (r) of 0.51 (p=0.114 for deviation from zero slope). One statistically significant outlier was removed (Methods). Myc TRBP A regression r=0.06 (p=0.638) and Myc TRBP B regression r=0.62 (p=0.06) (H) Coimmunoprecipitation of FL-Lin28a with myc-TRBP-AB and B, but not TBRP-A. (A-F) * p<0.05, ANOVA

FIGURE 2

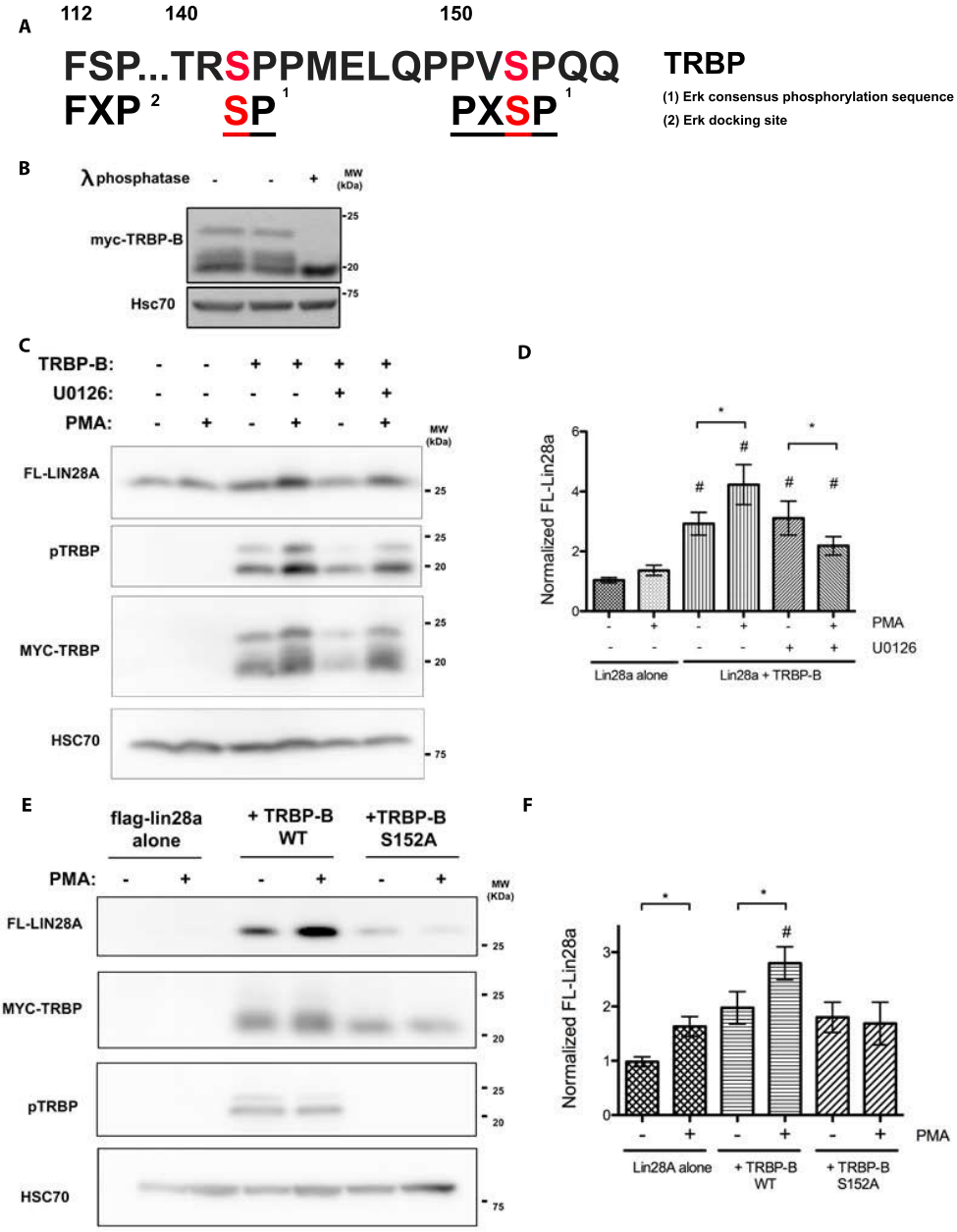

Figure 2. TRBP-B phosphorylation at S152 enhances binding to Lin28a. (A) Putative ERK substrate sequence of TRBP at serine 152, including FSP docking site. Weaker candidate ERK substrate at serine 142 (B) Immunoblot from 293T cells expressing TRBP-B shows two or more phosphorylated species exist and can be collapsed by lysate treatment with lambda phosphatase. (C,D) Representative blot and quantitation showing levels of FL-Lin28a, phospho-TRBP and myc-TRBP-B proteins from 293T cells pretreated with U0126 (20 uM), with or without PMA treatment (50 ng/mL) (n=15) (E,F) Representative blot and quantitation showing effect of PMA on FL-Lin28a level in Tarbp2-/- MEF cells coexpressing TRBP-WT or S152A and treated with PMA (n=8) (D,F) # $p<0.05$, ANOVA; * $p<0.05$, paired t-test.

FIGURE 3

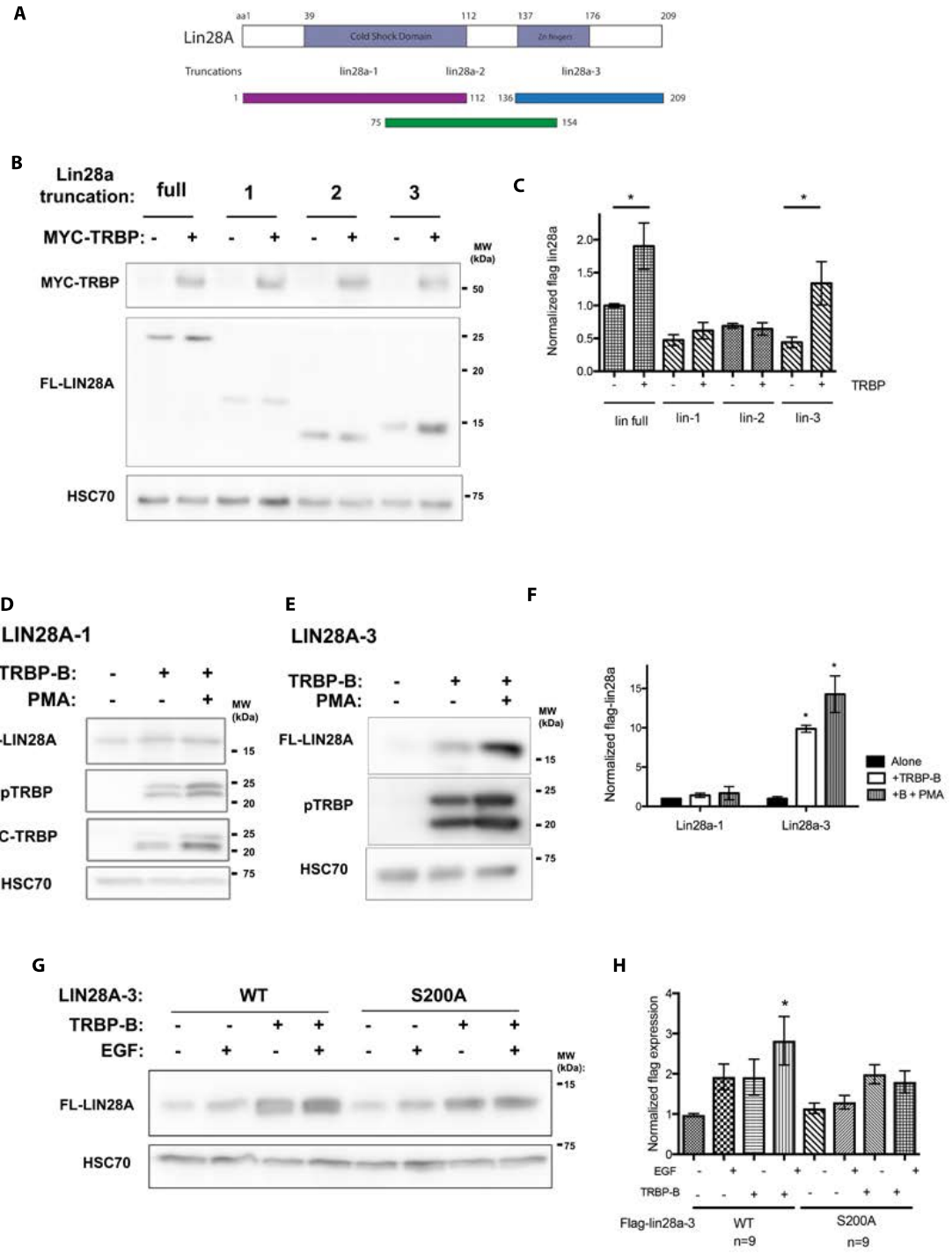

Figure 3. A C-terminal Lin28a truncation sufficient to respond to TRBP and TRBP-B. (A) Domain map of Lin28a, with truncations Lin28a-1, 2 and 3. (B,C) Coexpression of FL-Lin28a and truncations with full length TRBP in 293T cells increases Lin28a and Lin28a-3. (* $p<0.05$, ANOVA, n=4) (D-F) Effect of coexpression of TRBP-B and treatment with PMA on protein level of

FL-Lin28a-1 (D) and FL-Lin28a-3 (E). (* p<0.01, two-way ANOVA, n=3-5) (G-H) Effect of coexpression of TRBP-B on WT or S200A mutant of FL-Lin28a-3 (* p<0.05, ANOVA, n=9)

FIGURE 4

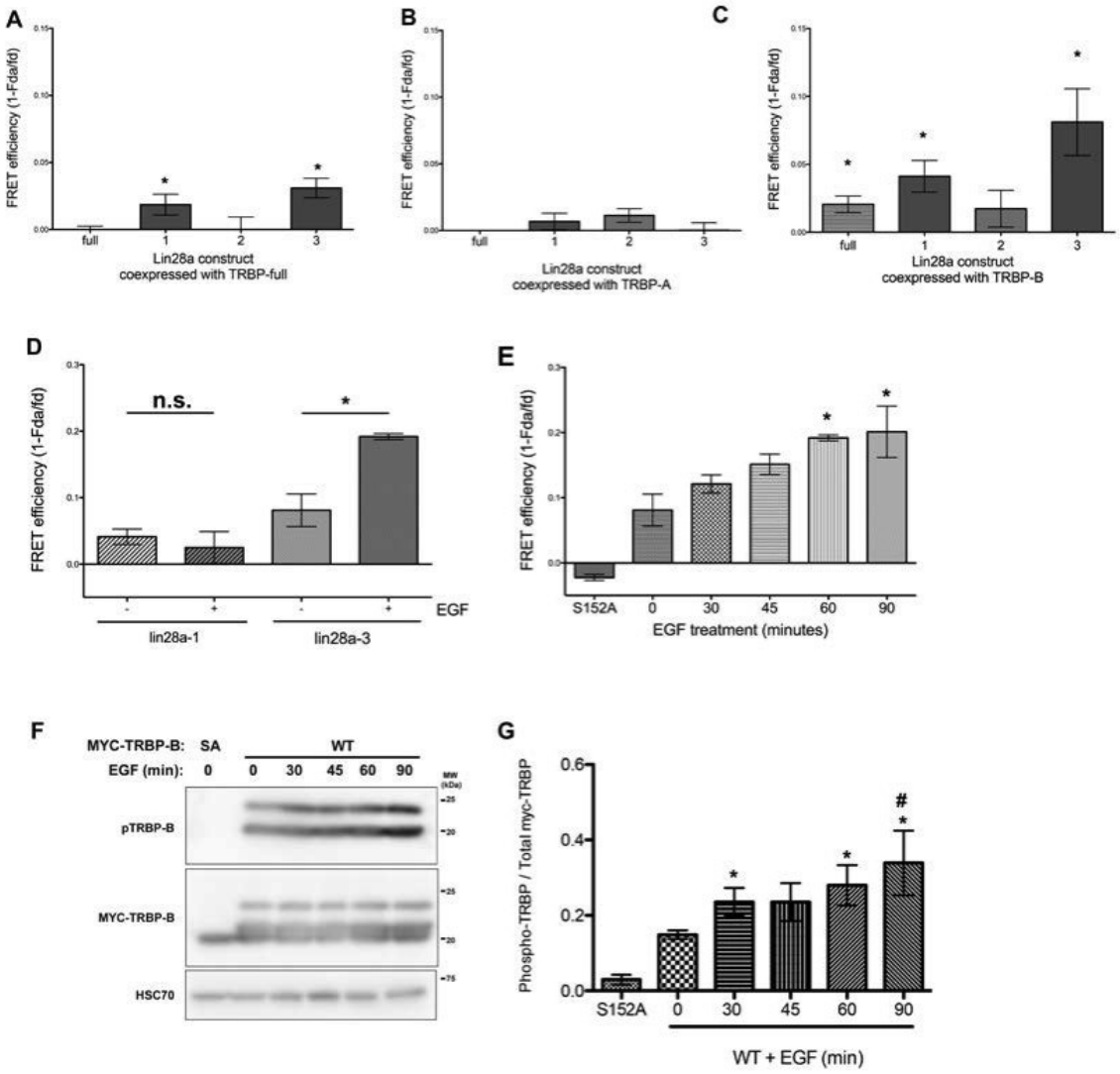

Figure 4. Lin28a-3 interacts with TRBP-B in a phosphorylation inducible manner. (A) FRET efficiency of C-terminal cpVenusE172-tagged Lin28a and truncations with full-length N-terminal Cerulean3-tagged TRBP (B-C) FRET efficiency of Lin28a and truncations with TRBP-A and B. (A-C) *p<0.05 vs. 0, t test (D) FRET efficiency of Lin28a-1 and 3 with TRBP-B after treatment with 100 ng/mL EGF for 60 minutes. (E) FRET efficiency of Lin28a-3 with TRBP-B after EGF treatment. “S152A” indicates efficiency of Lin28a-3 with phosphomutant TRBP-S152A (D-E, * p<0.05 vs. untreated, ANOVA) (A-E) n=15-75 cells per column from at least two dishes. (F, G) Increase in phospho-TRBP-B, measured by immunoblot, after EGF treatment. (#p<0.05, ANOVA, * p<0.05, paired t test; n=6)

FIGURE 5

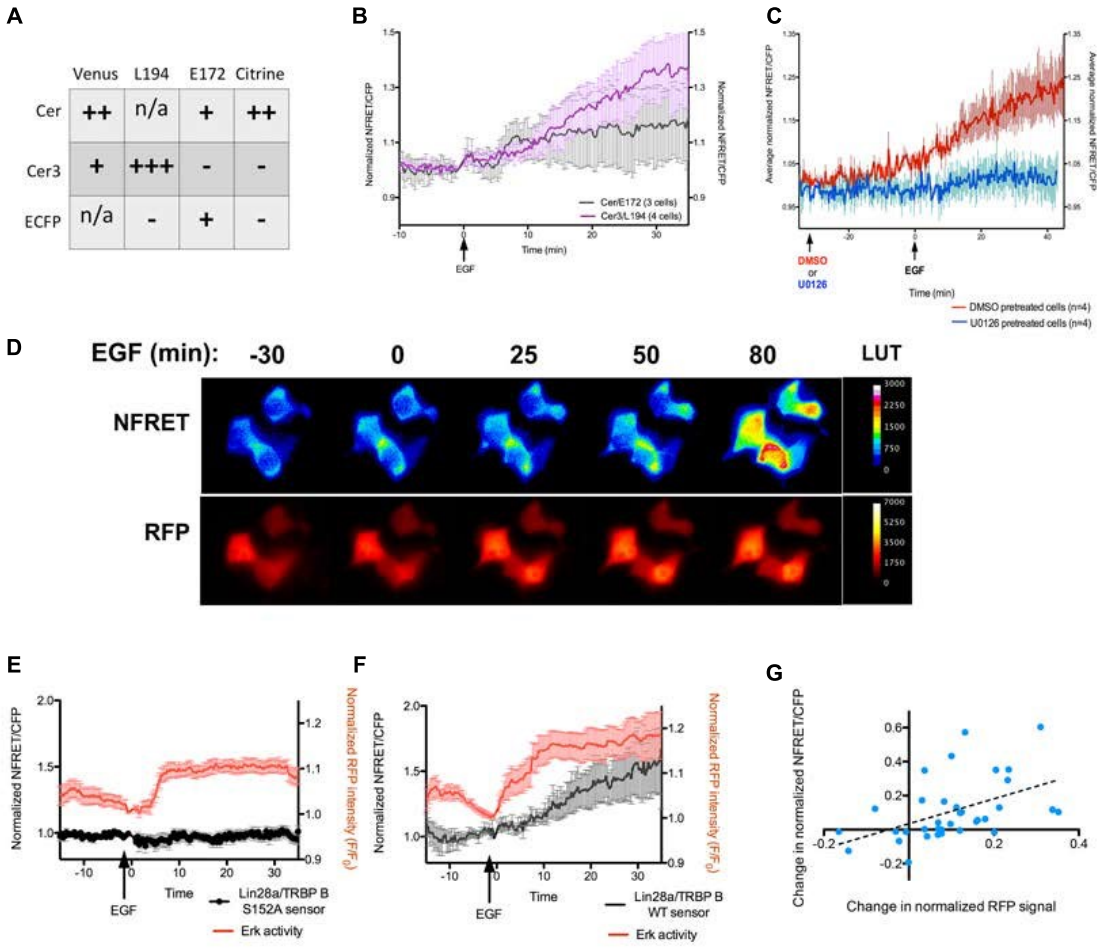

Figure 5. Optimization of a sensor for phosphorylation-induced Lin28a/TRBP binding. (A) Qualitative assessment of Lin28a/TRBP FRET pairs, scored based on flat baseline and magnitude of response (n=2-6 dishes/pair). (B) Comparison of NFRET ratio change, normalized to T0, between representative 293T cells expressing sensor with original FRET pair ("Cer/E172") or optimized sensor ("Cer3/L194") after EGF treatment. (C) Optimized sensor FRET response to EGF in 293T cells pretreated with vehicle (red) or U0126 (blue) (n=4 cells per condition). (D) Pseudocolor image series of Cer3/L194 sensor signal ("NFRET") and EKAR sensor intensity ("RFP") in 293T cells pretreated with DMSO and then treated with EGF. (E-F) Representative curves showing change in NFRET (black) coimaged with increase in Erk activity (red) in response to EGF in cells expressing S152A sensor (E, n=7) or WT sensor (F, n=6) (G) Regression analysis of EKAR intensity change and NFRET intensity change, measured 30 minutes after EGF treatment (n=35 cells from 7 dishes). Regression line r = 0.23 (p=0.004)

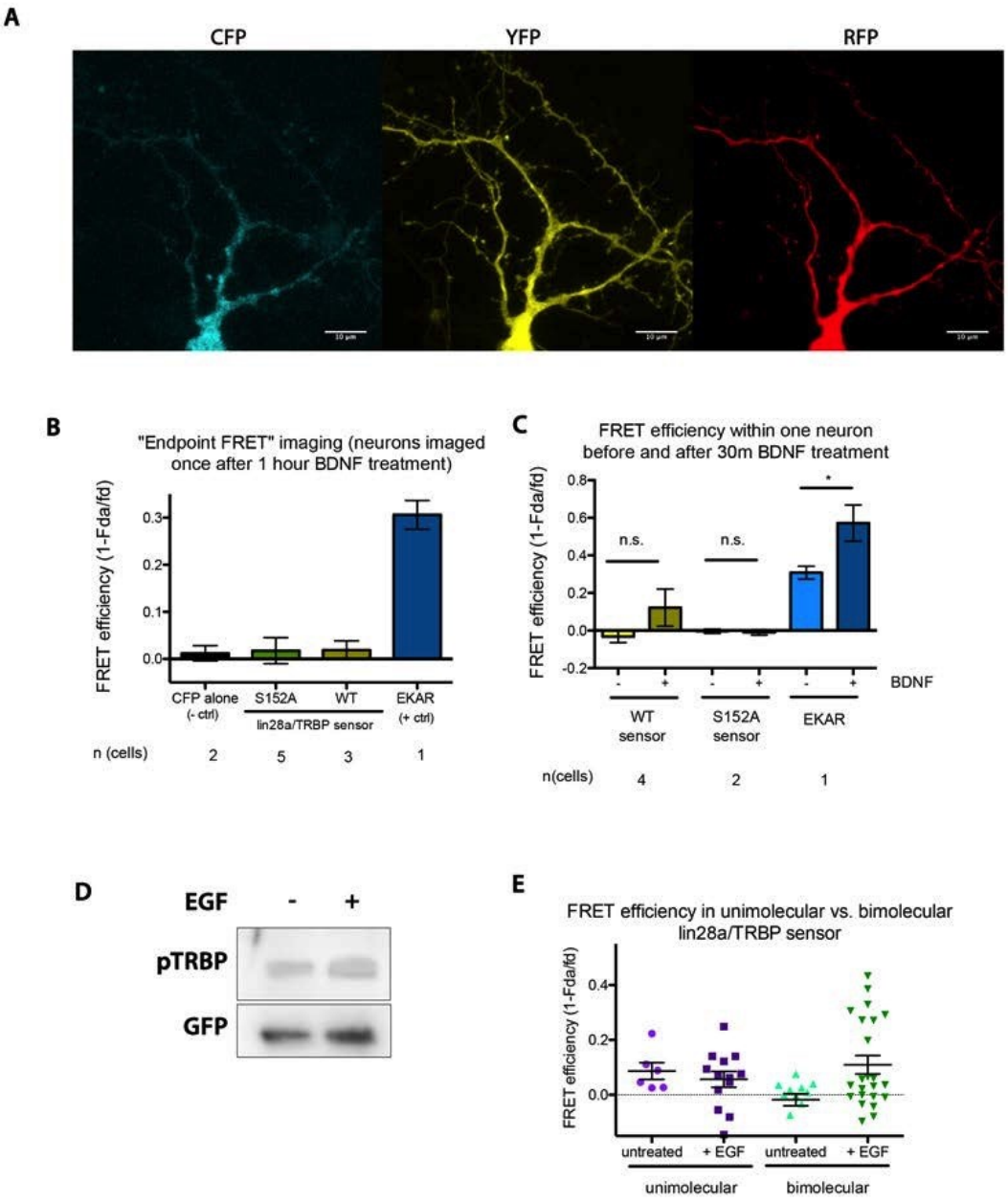

Figure 6. Toward neuronal imaging of Lin28a/TRBP interaction. (A) Representative images of a hippocampal pyramidal neuron coexpressing Cerulean-TRBP-B (CFP), Lin28a-3-L194 (YFP), and mCherry filler. Note restricted CFP distribution. (B) FRET efficiency in hippocampal pyramidal neurons expressing CFP alone, WT sensor, S152A sensor, or EKAR, treated with BDNF for one hour prior to photobleaching. (C) FRET efficiency in paired dendrites from single neurons before and after 30m BDNF treatment. (D) Increase in TRBP phosphorylation relative to GFP in unimolecular sensor after 30m EGF treatment. (E) FRET efficiency in 293T cells expressing bimolecular sensor (green) or unimolecular sensor (purple) with and without 30m EGF treatment.

SUPPLEMENTARY FIGURE 1, RELATED TO FIGURE 1

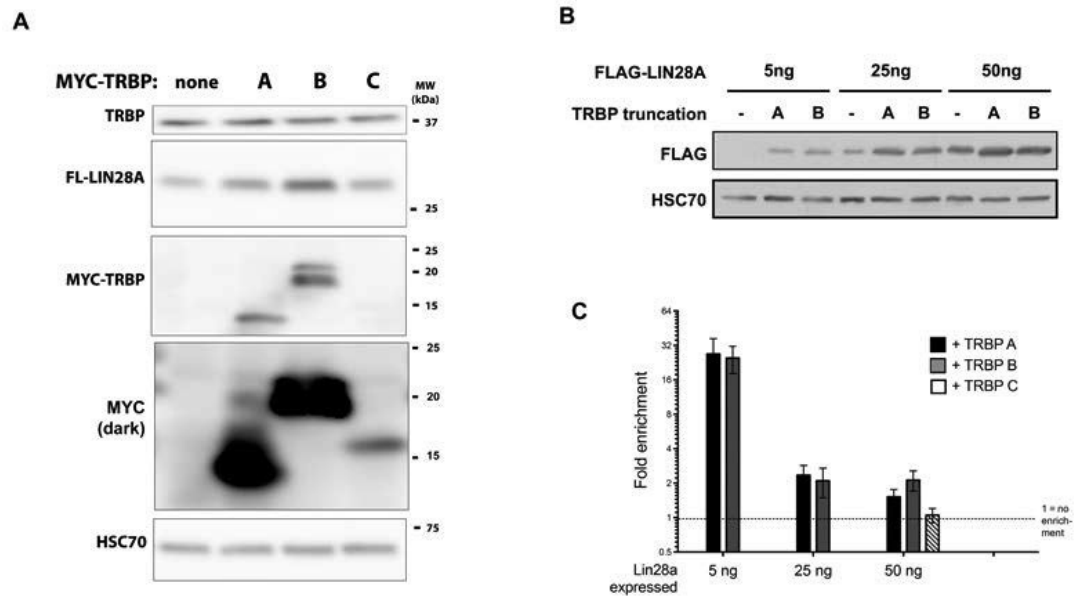

Figure S1. Increasing Lin28a transfected reduces fold stabilization by TRBP. (A) Overexposure of lysates expressing myc TRBP A, B and C, showing weak myc TRBP C signal. (B-C) Effect of expression of equal amounts of TRBP A or B on the stability of 5, 25 or 50 ng of transfected Lin28a in 293T cells (n=3-5)

SUPPLEMENTARY FIGURE 2, RELATED TO FIGURE 2

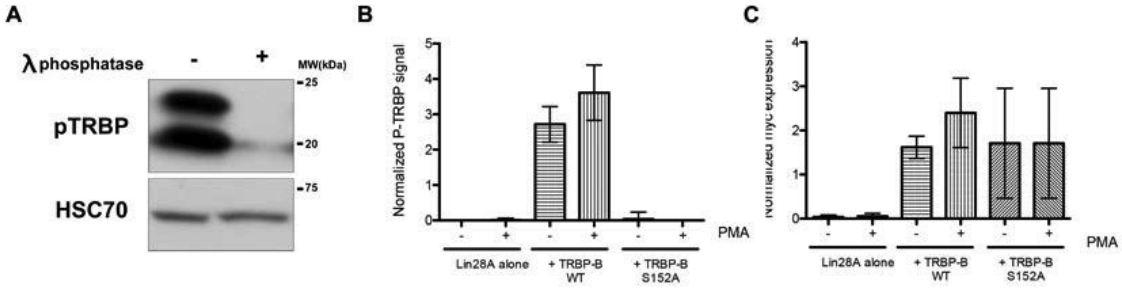

Figure S2. TRBP-B phosphorylation level in Tarbp2-/- MEF cells. (A) Validation of p-TRBP S152 antibody using phosphatase-treated lysates expressing myc TRBP B, as in Figure 2B. (B-C) Related to Figure 2E-F. Quantitation of level of myc TRBP-B (n=6-8) (C) and phospho TRBP-B S152 (n=9) (B) in Tarbp2-/- cells expressing FL-Lin28a and a WT or S152A TRBP-B, treated with PMA or vehicle.

SUPPLEMENTARY FIGURE 3, RELATED TO FIGURE 4

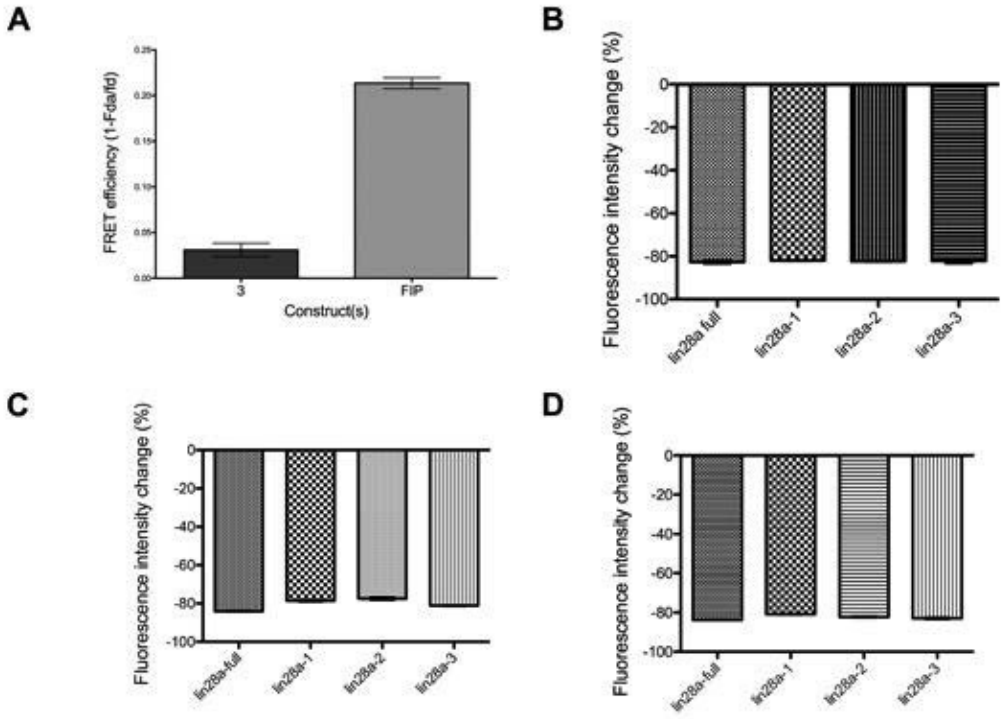

Figure S3. Comparable YFP photobleaching across FRET efficiency experiments. (A) FRET efficiency of a positive control construct, FIP, compared to Lin28a-3 + TRBP B (Romoser et al., 1997) (B-D) Percent reduction in YFP intensity in photobleaching experiments using full-length CFP-tagged TRBP (B), TRBP A (C), and TRBP B (D). Comparable YFP reduction was attained across all construct pairs. N=15-75 cells per column, from at least two independent dishes.

SUPPLEMENTARY FIGURE 4, RELATED TO FIGURE 5

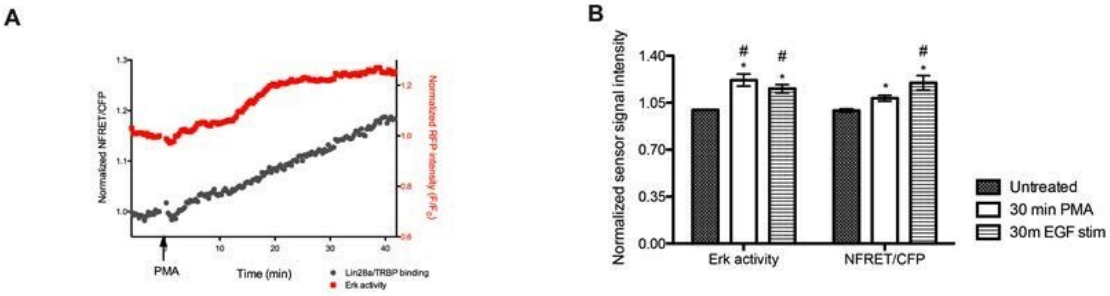

Figure S4. Supporting data from FRET sensor development. (A) Representative curves showing response of Lin28a/TRBP sensor (gray) and EKAR (red) in a single cell treated with PMA. (B) Average normalized change in Erk activity and NFRET/CFP ratio in cells treated with PMA (n=12) or EGF (n=15) * p<0.05, t-test; # p<0.05, ANOVA

Chapter 3: Genetically encoded fluorescent biosensors for live-cell visualization of protein phosphorylation

Introduction

From the first use of fluorescently-tagged antibodies to image fixed cells through the present, scientists have wanted to visualize and thus better understand various molecular systems inside the cell. One tool that has gained traction for real-time analysis of these systems is the fluorescence-based, genetically encodable biosensor.

Early optical sensors included small molecules that bound to analytes, such as fura2 to calcium (Williams et al., 1985). Expanding the scope of biosensors to detect targets that are not easily bound by small molecules, a cAMP probe was developed in 1985 based on the dissociation of the catalytic and regulatory subunits of protein kinase A (PKA) when the kinase is activated (Adams et al., 1991). The two subunits were purified separately, tagged with the fluorophores rhodamine and fluorescein, and finally reintroduced to cells by microinjection. The dissociation of the subunits when cAMP was present caused a change in energy transfer between the two fluorophores, enabling visualization of where and when cAMP was produced for the first time. However, the probe was labor-intensive to produce and cumbersome to introduce into cells.

The advent of GFP and other fluorescent proteins solved both of these difficulties at once, and has inspired subsequent decades of optical probe design. Fluorescent proteins have proven to be a good tool for measuring in-cell activity

because they are genetically encodable, bright, and available in many colors, enabling monitoring more than one target. Their genetic encodability is especially desirable in order to take advantage of the cell's own protein-synthesis machinery, introduce fluorophores with minimal disruption to the cell, and target probes to subcellular regions of interest. Furthermore, fluorescent proteins, having evolved in a cellular environment and been extensively engineered for use in mammalian cells, are compatible with cellular pHs, redox properties, and other characteristics.

After early development of genetically encoded reporters for calcium (Miyawaki et al., 1997) and cAMP (Zaccolo et al., 2000), a wide range of biosensors has been developed for monitoring different cellular events. Sensors for changes in pH and redox state; accumulation of second messengers; and activation of enzymes like kinases and phosphatases have all been reported. Kinases constitute a key class of signaling proteins, mediating information flow between external and internal environments or between subcellular compartments. Because of the broad reach of each activated kinase and the complex signaling cascades that lead to its activation, many kinases are key nodes in cell signaling networks.

This chapter aims to introduce the reader to biosensor development and application, focusing on those developed for kinases and their upstream second messengers. In the effort to understand signaling as it occurs *in vivo*, non-destructive technologies for monitoring signaling over time are required; biosensors are uniquely positioned to fill this need. In recent years, kinase

activity reporters have been used to address a variety of systems-level questions in increasingly complex model systems.

In their conception and optimization, in-cell fluorescent biosensors have a great deal in common with development of small-molecule probes. Like such probes, genetically encodable biosensors are used for studies of basic biology and also to investigate the activities of many different disease-relevant signaling pathways. These tools are effort-intensive in terms of conception, development and optimization; however, the resulting benefit of these tools especially in furthering our understanding of signaling biology outweigh the costs associated with the design process. Like any good technological product, probes are subject to quality control and are often modified based on user feedback. Thus, we introduce the "pipeline" of biosensor development and application (see figure 1). We will begin by addressing some common considerations and frequently-used blueprints for biosensor design, then report as a case study the ongoing effort to develop a sensor for I kappa B kinse (IKK). We will conclude with considerations for the use of biosensors once they are developed, and the outlook of the field as a whole.

Biosensors: the pipeline

Genetically encodable probes

The general blueprint for a kinase/second messenger biosensor includes a sensing unit that senses the change of interest, and a reporting unit to indicate

the sensing unit's state. To visualize a signaling event of interest, the designer of a sensor often needs to identify or engineer a molecular switch wherein a change in conformation occurs in response to signaling. The reporting unit typically contains one or more fluorescent proteins. A wide variety of genetically encodable kinase activity biosensors and second messenger indicators have been developed along these lines (summarized in table 1).

Sensing

One approach to generating a molecular switch is to regard the cell as a molecular toolkit—the approach used in developing the first PKA-based sensor for cAMP. The switch can be a protein or protein fragment that changes its conformation upon binding to a second messenger molecule; or it may change conformation after being enzymatically modified by the signaling enzyme of interest. Probes designed along these lines include a FRET-based sensor for the conformational change of NFAT after dephosphorylation by calcineurin (Newman et al., 2008) and a split-luciferase sensor for activity-related conformational changes in Abl kinase (Zhou et al., 2009).

If no suitable change occurs within one protein, the designer may repurpose domains from several proteins to develop an engineered switch. In the case of a kinase activity reporter, for example, a common blueprint involves the consensus substrate sequence, separated by a linker from a phospho amino acid binding domain that binds to that sequence when it is phosphorylated. The phospho amino-acid binding domain (often designated PAABD in schematic

diagrams) is usually adapted from a conserved domain such as the 14,3,3 proteins; forkhead-associated (FHA) domain; two-tryptophan (WW) domain; or Src homology (SH2) domain. Sensors for activity of PKA (Zhang et al., 2001), Erk (Harvey et al., 2008), and a wide variety of other kinases use this scheme.

Switches derived from two endogenous proteins may also be left separate, in order to form a bimolecular sensor. The bimolecular sensor class is quite large and includes many sensors designed on an ad-hoc basis for studies to determine when and where two proteins of interest interact, including heteromeric binding of receptors for peptide hormones (Almabouada et al., 2013), various neurotransmitters (Borroto-Escuela et al., 2012), SNAREs (Degtyar et al., 2013) and immune signaling molecules (Hashimoto-Tane et al., 2010). In addition to providing information about the location and timing of protein interactions, bimolecular sensors can be used to determine what portions of the proteins are required for interaction (Borroto-Escuela et al., 2012) or to characterize the dissociation kinetics of the two proteins (Song et al., 2012).

Occasionally, to solve problems such as very high basal FRET, sensors initially designed in a single-polypeptide unimolecular format have been broken into bimolecular sensors by removing the linker to generate two separate proteins (Herbst et al., 2011). This modification can yield sensors with greater dynamic range, owing to better separation of FRET partners in the “off” state, but it can also introduce difficulties in data interpretation. In bimolecular versions of a probe, the donor/acceptor stoichiometry is not fixed, which can affect the signal (Jares-Erijmen and Jovin, 2003). This added variable requires the experimenter

either to ascertain that the two subunits are expressed at equal levels or to use one of several correction algorithms that correct for nonhomogeneous subcellular distribution or uneven labeling before calculating FRET (Hachet-Haas et al, 2006; Deplazes et al, 2012). It has also been observed that bimolecular versions are much more sensitive to off-target binding. For example, a bimolecular version of the calcium sensor Cameleon was based on calcium induced binding between calmodulin and the calmodulin-binding domain of myosin light chain kinase (MLCK). The bimolecular version of Cameleon was suggested to have a higher tendency to bind to endogenous components (Miyawaki, 2003). In this case, even the unimolecular version was influenced by binding of endogenous components, showing very low optical activity when endogenous calmodulin was abundant. This problem led to an effort to rationally re-engineer calmodulin and calmodulin binding peptides that bind to one another and to calcium, but clash sterically with endogenous calmodulin, based on a “bump and hole” modification of binding surfaces (Palmer et al., 2006).

If a desired switch cannot be assembled from naturally-occurring proteins or domains, it is possible to engineer a switch or part of a switch such as a binding domain. For example, in the absence of a strong and specific binding protein for phosphorylated IκBα, which is usually degraded following phosphorylation, one group used SELEX, a technique for directed evolution from a starting RNA library, to obtain a peptide that bound specifically to phospho-IκBα (Olson et al., 2008). This binding domain was tested in the context of an

engineered molecular switch for an activity reporter for IKK (inhibitor of NF-κB kinase) and was found to be functional in vitro.

The conformational change of the switch can be engineered using different designs. For instance, a switch could be engineered using the design of a pseudo-ligand, which ideally binds only when the true ligand is absent. For example, an Akt-based probe for the presence of 3' phosphoinositides used the pleckstrin homology (PH) domain from Akt, fused with an acidic peptide pseudo-ligand that bound to the PH domain with low affinity. When phosphoinositides are present, the pseudo-ligand is displaced, changing the switch conformation (Ananthanarayanan et al, 2007). Based on a similar pseudoligand design, some switches are engineered to be a hybrid of genetically encoded and synthetic domains. "Snifit" is a transmembrane probe composed of a glutamate receptor with two "self-labeling" peptide tags added to the extracellular terminus. These peptides can be covalently labeled with fluorescent dyes bearing moieties that react specifically with cognate groups on the peptides (Gautier et al., 2008). In the case of Snifit, one synthetic fluorophore and another synthetic fluorophore conjugated with a glutamate mimic as the pseudoligand are added to label cells expressing Snifit such that FRET occurs between two fluorophores in the absence of glutamate. The pseudoligand, however, is displaced by endogenous glutamate, resulting in reduced FRET when glutamate is present in the extracellular space (Brun et al., 2012). Other synthetic strategies for kinase activity visualization have been reviewed by Rothman et al (2005).

Reporting

Once a molecular switch is selected, it must be placed within a sensor so that its binding or conformational change produces a change in optical properties. A number of design principles exist, ranging from simple intensity changes to ratiometric methods (see figure 2). Reporting domains may consist of one fluorescent protein, two peptides that combine to reconstitute a fluorescent or luminescent protein, or two fluorescent proteins.

Single fluorescent protein-based biosensors typically use a fluorescent protein with its protective beta-barrel broken, engineered so that the conformational change of the embedded molecular switch is transduced to also change the fluorescent protein's conformation and allow fluorescence to recover. This strategy has been used to create sensors for calcium, including GCAMP (Nakai et al., 2001). In one case, it has been used to indicate tyrosine phosphorylation (Kawai et al, 2004).

Bimolecular fragment complementation-based probes, feature two complementary fragments of a fluorescent protein, able to fluoresce only if they are brought into proximity, or two fragments of luciferase that reconstitute a functional luciferase when brought into proximity. These probes have been used for analysis of protein/protein interactions and kinase activity (Herbst et al., 2011); between the two, luciferase fragment complementation is more favorable for tracking reversible processes because fluorescent protein complementation is irreversible (Rebois et al., 2008).

Sensors using two fluorescent proteins typically rely on fluorescence resonance energy transfer (FRET). FRET is the non-radiative transfer of energy from one fluorophore to another via dipole-dipole interactions, resulting in reduced fluorescence from the shorter-wavelength and higher-energy "donor" fluorophore and increased emission from the longer-wavelength and lower-energy "acceptor." Because FRET is highly distance and orientation dependent, with a sharp decrease in efficiency at nanometer-scale distances much shorter than the diffraction limit of light, it is a useful biophysical process for sensing proximity on a scale too small to be visualized as co-localization.

Flanking a molecular switch with a fluorescent protein pair competent for FRET enables monitoring of the conformation of the switch by the changes in FRET. One popular measure is FRET intensity ratio, a ratio of acceptor emission to donor emission after excitation at the donor wavelength. In addition to intensity, FRET can be measured by donor fluorescence lifetime (Padilla-Parra et al, 2012) or fluorescence anisotropy (Piston and Rizzo, 2008); these techniques, along with advantages and disadvantages of each, have been reviewed at length in the reviews listed above, as well as by Day and Davidson, 2012; Periasamy et al., 2008; and Sun et al., 2013.

Biosensor quality control and optimization

A successful probe needs to be both sensitive to and specific for the species of signaling molecule under study. Specificity for the kinase of interest

needs to be verified, and the sensitivity and dynamic range of the probe generally require empirical optimization.

Once a probe is developed, and shows a satisfactory change in optical properties in response to the signal of interest, it is important to confirm that the optical change is specific to that signal. For probes based on kinase substrates, generating a quality control to rule out artifactual changes can be as easy as mutating the phosphorylated residue of the sensor to ensure that signal changes are abolished (Herbst et al., 2011). Another approach, which ensures that phosphorylation stems from the kinase of interest, is to stimulate cells expressing the kinase biosensor in the presence of an inhibitor specific to the kinase to ascertain that no spurious signal is observed (Eisler et al., 2012). The optical change may also be compared with traditional biochemical techniques like western blotting if phospho- and total protein antibodies are available for the target kinase or its substrates (Newman et al., 2008).

Many phosphorylation reactions are carried out by a large family of related kinases with subtly different selectivity and activity; therefore, another consideration in a probe's specificity is whether it is selective to the specific enzyme. Kajimoto et al. (2010) specialized a pre-existing protein kinase C (PKC) sensor (Violin et al., 2003) based on a consensus PKC phosphorylation site, using sequences from PKCδ substrates. When the new probe was expressed alongside a panel of FP-tagged PKC isoforms, it responded specifically to PKCδ. An alternate approach to enhancing specificity is to add a selectivity-enhancing module to the sensor backbone; for example, Fosbrink et al. (2010) generated a

probe selective for JNK over Erk1/2 by adding a docking domain to the shared substrate sequence. This type of optimization enables investigation of differences between closely related but differentially regulated kinases.

Once specificity has been established, a probe's sensitivity can be characterized using in vitro assays. For example, a dose-response curve showing optical changes in response to increasing analyte concentrations can be used to determine both dynamic range of the probe, in terms of response amplitude, and the concentration range of analyte that can be sensed accurately (Tantama et al., 2012). In some cases, this *in vitro* step is bypassed in the development of kinase sensors because of the relative difficulty of purifying kinases in their active form; instead, the magnitude of response to a known strong stimulant of the kinase is measured. For probes with a low dynamic range or small FRET change, only very large changes in kinase or phosphatase activity can be detected. Because responses to strong stimuli in cultured cells usually far exceed responses to physiological stimuli *in vivo*, such probes require optimization in order to detect subtler changes. Optimization can be carried out on a semi-rational basis by tuning various factors that affect the FRET efficiency, including orientation of and distance between the two fluorophores.

Because effective energy transfer depends on alignment at an optimal orientation of the two fluorophores, minor changes during the optimization of biosensors can lead to unpredictable changes in dynamic range. One common strategy for biosensor optimization is to switch between spectrally similar fluorescent proteins in order to alter the orientation of the donor and acceptor

fluorophores. For example, introduction of circularly permuted Venus, whose N and C termini are at different positions relative to the central fluorophore, can be a useful strategy to increase the dynamic range of probes (Nagai et al., 2004; Allen et al., 2006).

Distance between the fluorophores can be modulated by changes to the length of a peptide linker in a unimolecular sensor, often yielding changes in dynamic range. The linkers of unimolecular sensors have been the target of extensive optimization efforts. Several groups have worked to optimize a generic backbone using a flexible linker, which allows the fluorescent protein pair to sample many different orientations and limits signal induced changes to those dependent on distance. Although the process of adjusting linker length for optimal FRET efficiency takes time, once a suitable linker is found, it may be used for different substrate/recognition domain pairs. Komatsu et al. (2011) developed a backbone with a flexible 116 amino acid linker that improved the dynamic range for a number of kinase and GTPase sensors and was used to rapidly develop several new kinase sensors. Ibraheem et al. (2011) used a library approach to optimize linker length, comparing basal and maximally-stimulated states in replica-plated bacterial colonies. This approach allowed rapid assessment of dynamic range in a large number of variants of the probe. An alternate approach, especially useful for probes with highly structured components, is to rationally design rigid linkers to optimize fluorophore distance (Lissandron et al., 2005).

However, distance dependency of FRET may not always be easily deconvolved from orientation dependency. For example, while developing a unimolecular sensor for glutamate based on the conformational change of a glutamate-binding protein, one group observed a four-fold change in dynamic range between versions that differed in length by only one amino acid (Hires et al., 2008). They ascribed this change to the sensitivity of energy transfer to minute differences in orientation and distance, which were enhanced by the rigidity of the peptide in between the fluorescent proteins.

Publication to report on the development of a sensor is rarely the final word in its optimization (see figure 3.1). Even after a sensor has been introduced, updated versions are frequently released. The groups or individuals who developed a probe often continue to improve it, while users also adapt probes for their needs. In many cases, dynamic range remains relatively small, with continued optimization a desirable and ongoing process (Marvin et al, 2013; Depry et al., 2011; Kajimoto et al., 2010). Adaptations to prior probes include changing optical readouts, for example converting a probe optimized for ratiometric FRET for FLIM imaging, (Oliveira and Yasuda, 2013), and reducing sensitivity to pH and other off-target variables. Thus, optimization is most effective with specific applications in mind.

Sensor expression in primary culture and live animals

The payoff for the lengthy work of biosensor development is the ability to use the finished product to address a wide range of questions in many cell types. The fundamental question sensors uniquely answer is how various kinases function in a cellular context; although antibodies may be available to give insight into phosphorylation state, they can provide only snapshots of kinase activity. Biosensor approaches offer enhanced spatiotemporal resolution.

Often the first generation of a sensor is used to inquire into how the kinase of interest behaves in a cell line. The use of sensors to better understand such signaling has been reviewed extensively (Sipieter et al, 2013; Miyawaki, 2003; Mehta et al., 2011). Briefly put, a novel sensor can be used to explore the role of a kinase in cell activities, to study how absence or overexpression of interactors affects activity of the kinase, the location of kinase activation, and circuit analysis of interacting pathways, among other questions.

There are many cell-type-specific processes that are known to involve the activity of one or more kinases, but wherein the exact function of the kinase in question is incompletely described. In order to get that missing information in a more physiologically relevant context, primary cells and live animals are used. We will describe in detail how sensors have provided valuable information about neuronal cell biology, then examine the emerging field of transgenic, biosensor-expressing animals.

Biosensor imaging in transgenic animals

While most of the biosensor experiments described above were carried out in transiently transfected primary cell cultures, studies of PKA in neurons have recently become available in a whole-brain context in live, behaving animals. One study used a fly line inducibly expressing AKAR, which was imaged via two-photon FLIM, to understand why the mutants *rutabaga* and *dunce* have defects in aversive learning (Gervasi et al., 2010). The authors found that rutabaga, a calcium-sensitive adenylyl cyclase, is a coincidence detector for octopaminergic and dopaminergic stimuli that are both below threshold levels, facilitating associative learning; mutations in *rut* slowed the accumulation of PKA activity. On the other hand, mutations to dunce, a phosphodiesterase, caused a slightly higher PKA response than the wild-type; the phosphodiesterase plays a role in restriction of dopamine-responsive PKA activity to specific brain regions.

This is a good example of the potential of kinase and phosphatase studies *in vivo* to further our understanding of the connections between subcellular signaling circuits and behavioral output. For translational purposes, mammalian systems such as mouse are appealing targets for similar *in vivo* studies. However, there are a number of challenges for *in vivo* kinase studies, particularly in living mice. Because of the propensity of tissue to scatter light, special imaging techniques may be needed for effective kinase activity visualization *in vivo*. Many studies use two-photon fluorescence imaging on surgically exposed tissues. Two-photon imaging, which uses two long-wavelength beams to excite only within a focal spot, offers better tissue penetration and reduced photobleaching compared to shorter wavelength illumination.

Expression level is a constant challenge in the development of biosensor-expressing animals. Sensors can be silenced or recombined out of the genome (Yamaguchi et al., 2011), and they sometimes appear unpredictably in only a few tissues. For example, in a double-transgenic mouse line carrying two halves of a bimolecular reporter, both driven by the same ostensibly ubiquitous reporter, one was expressed reasonably brightly in a number of tissue types, whereas the second appeared only in testes (Audet et al., 2010). When expression is too low, effective FRET studies cannot be carried out because of extremely low signal-to-noise ratios. Overexpression, however, may cause embryonic lethality or perturbation of the signaling system beyond physiological relevance (Hara et al., 2004). Although transgenic calcium-sensing mice, including some that express FRET-based sensors such as Cameleon (Hara et al, 2004), have existed for some time, mice expressing kinase sensors have only recently became available.

A recent effort using cytoplasmic mRNA injection yielded mice ubiquitously expressing AKAR, EKAR and nucleus-targeted EKAR (Kamioka et al., 2012). These were used for several proof-of-principle studies, including comparative analysis of PKA and Erk responses to laser ablation of epidermal tissues. The authors propose that these mice may be useful for studying pharmacodynamics in vivo.

The same mouse lines have also proven useful, albeit in a tissue-culture explant system, for studying relationships between signaling circuits. Gut explants from AKAR and EKAR mice were used to study the relationships

between pro-migration and anti-migration signaling circuits in organ-cultured enteric nervous system progenitor cells (Goto et al., 2013). By watching the relationship between location and kinase or GTPase activity in real time in a network of neural progenitor cells advancing along the gut, the authors determined that Rac1 and Cdc42 activity were highest toward the leading edge, both within and between cells, whereas PKA activity was lower in the migrating cells and higher in the stationary network cells. The authors were also able to show that some kinases, such as JNK, that were purportedly required for migration, do not seem to affect its velocity or direction.

Blending activity-based biosensing with two-photon techniques for chronic in-vivo neuron imaging, Mower et al. (2013) showed that CaMKII, mentioned above for its role in spine signaling in dissociated cultures, also plays a key role in spine and synapse maintenance in living brains. In ferrets expressing the CaMKII sensor Camui, delivered by viral vector, the authors determined that irrespective of starting spine size, dendritic spines with low basal CaMKII activity were more likely to be lost after sensory deprivation than spines with higher starting CaMKII.

Case study: developing a sensor for I kappa B Kinase (IKK)

Background

NFκB is a family of immunomodulatory transcription factor, and one of the earliest demonstrated examples of signal-responsive modification of gene

transcription. In unstimulated cells, the transcription factor is found in dimer form in the cytoplasm, retained there by binding of one of a family of proteins known as the inhibitors of κB. For our purposes, the most relevant is IκBα. Binding between NFκB dimers and IκBα is thought to occlude the nuclear localization sequence of NFκB (Beg et al., 1992). When phosphorylated by one of two IκB kinases, IKKα or IKKβ, IκBα is recognized and polyubiquitinated by a ubiquitin E3 ligase complex containing beta-TRCP, the beta transducin repeat containing protein (Traenckner et al., 1995; Suzuki et al., 2001). Polyubiquitination enables proteasomal degradation of IkBa (Chen et al., 1995). This frees NFκB to translocate to the nucleus, where it binds DNA and facilitates the transcription of target genes (Roff et al., 1996). Among its transcriptional targets, are cytokines, membrane proteins, transcription factors and apoptosis inhibitors. NFκB activity also targets IκBα and other suppressors of NFκB activation, which mediate negative feedback to the NFκB signaling circuit (Arenzana-Seisdedos et al., 1995).

IKK activity is a necessary precursor to translocation and transcriptional activation of NFκB, and can further control the dynamics of NFκB signaling (Behar & Hoffmann, 2013). The two major IKKs, IKKα and IKKβ, exist in a high-molecular weight complex with one another and the regulatory subunit NEMO; however, they target different substrates, and are active in different cellular contexts. IKKα is primarily a regulator of adaptive immune responses (for example, lymphocyte activation), whereas IKKβ governs innate immunity (Hacker & Karin, 2006). In the canonical pathway for IKK activation, IKKβ is activated in

response to cytokines such as TNFa or IL-1B, which are generally recognized by "death receptors" in the TNF receptor superfamily (see figure 3.3a). Two serines in the IKK activation loop can be phosphorylated by self-transphosphorylation or by a variety of upstream kinases, including NFκB inducing kinase NIK, several MAPK kinases, and TGFβ activating kinase 1, in response to a variety of inflammatory signals (reviewed by Hosel & Schmid, 2013).

Single-cell imaging, usually focused on IKKβ signaling induced by TNFa, indicates that NFκB nuclear translocation is induced somewhat stochastically, with dramatic variation between individual cells exposed to the same stimulus. The percentage of mouse fibroblasts responding to a TNF stimulus increases with dose, but even at a high dose, not all cells respond (Tay et al., 2010). Given the complex system of feedback loops regulating this switchlike behavior, and the key role NFκB plays in cellular decision-making, the pathway has evoked a great deal of interest from computational biologists. In a B cell receptor response pathway, it has been demonstrated that positive feedback at the IKK activity step may account for some of the switchlike nature of NFκB signaling (Shinohara et al., 2014). There is also some computational evidence that persistent IKK activity can mediate longer term NFκB signaling (Witt et al., 2009). A sensor to directly monitor IKK activity would be advantageous for use in this system in order to better characterize the signaling mechanisms controlling NFκB activation, and to test the predictions of various computational models.

Strategies for IKK sensor design

The IκBα protein has many motifs conferring dynamic regulation. Most salient for a sensor is the IKK phosphorylation motif, including substrate serines 32 and 36 and the region surrounding them (DiDonato et al., 1997). After IKK phosphorylation, the phosphorylated motif is recognized by an E3 ligase which polyubiquitinates lysines 21 and 22 (Scherer et al., 1995, Baldi et al 1996). The ankyrin repeat domain, located C-terminal to the kinase substrate domain, confers binding to p65 (Huxford et al., 1998). A sequence known as the PEST domain, C-terminal to the ankyrin repeats, is required for IκBα turnover, in collaboration with the proteasome (Mathes et al., 2008). This region can be phosphorylated by casein kinase II, an alternate route to stimulus-induced IκBα degradation (McElhinney et al., 1996; Kato et al., 2003). Another degron, described more recently, overlaps with ankyrin repeat 6 (Fortmann et al., 2015). The relative importance of ankyrin repeats and PEST for protein turnover in response to signaling has been debated for some time, but is outside of the scope of this work.

Figure 3.4a shows a linearized schematic of full-length IκBα, along with the truncated sequences used in efforts by our group and others to optimize the IKK activity reporter (IKKAR). In the unimolecular sensor and the initial bimolecular sensor, we included amino acids 22 to 41, in keeping with a previous sensor effort (Olson et al) (figure 3.4a-A). Then we expanded our strategy to include a PEST domain from the endogenous protein (3.4a-B). Another construct, which was tested only preliminarily and not reported in this work,

included both the PEST domain and ubiquitin/SUMO modified lysines 20 and 21 (3.4a-C). Figure 3.4b shows a crystal structure of the ankyrin repeat domain of IκBα (teal) in complex with an NFκB dimer of p65 and p50 (grays) (PDBe 1ikn, Huxford et al. *Cell* 1998).

In a 2008 study, Olson and colleagues generated a phospho-IkBa binding protein derived from fibronectin through mRNA affinity selection (Olson et al., 2008). This approach uses a puromycin linkage to prevent disassociation of mRNA and protein, such that transcripts encoding protein products with the desired properties can be enriched and re-amplified, in a pseudo-evolutionary process. The fibronectin variant that was finally selected bound specifically to phosphorylated IκBα (amino acids 22-41), demonstrated by immunoprecipitation. When these two protein fragments were ligated into a CFP/YFP FRET sensor backbone, FRET was significantly higher when mixed with catalytically active IKK *in vitro* (see figure 3.3b). However, tests of the responsiveness of the novel sensor to stimulus-induced IKK activity in living cells were not reported, and personal communication by the lead author indicated that pilot studies had been unsuccessful (Olson et al., 2008).

In selecting a phosphorylated amino acid binding domain, in contrast with earlier efforts to sense IκBα phosphorylation, we opted to use the endogenous phosphorylated IκBα sensing protein, βTRCP. βTRCP forms the substrate recognition domain of a ubiquitin ligase complex that regulates degradation of IκBα, β-catenin (Winston et al., 1999) and several cell cycle factors (Nakayama & Nakayama, 2005). Phosphorylated substrates are recognized by a repeating

motif known as the WD-40 domain, which positions nearby lysines for enzymatic transfer of ubiquitin (Wu et al., 2003). Tandem repeats of WD-40 assemble into a structure resembling a propeller, with substrate recognition at the center of the propeller (Wu et al., 2003; Evrard-Todeschi et al., 2008). The crystal structure of the 7xWD40 domain is shown in figure 3.4c, with a linear domain map below (figure 3.4d; PDBe 1p22, Wu et al., 2003). The section used for phospho-recognition included amino acids 287 to 605, starting with a short sequence N-terminal to the WD repeats and extending to the end of the endogenous protein.

Finally, we constructed a unimolecular sensor incorporating the WD phospho-recognition domain, using the same layout as the sensor developed by Olson et al. A schematic is shown in figure 3.4e.

Selection of a sensor format

In cells expressing the two sensors using the WDx7 domain for phospho-IκBα recognition, a unimolecular layout proved inferior to the bimolecular sensor. In Cos7 fibroblasts treated with the IKK-activating cocktail of 100 ng/mL TNFα with the phosphatase inhibitor okadaic acid (500 nM), no FRET response was observable in cells expressing the unimolecular sensor, whereas a small subset of bimolecular-expressing sensor cells showed a small increase in FRET (representative curves shown in figure 3.5a).

The unimolecular fibronectin-based sensor published by Olson *et al.* also proved inferior to the bimolecular WDx7-based sensor. In MEF cells, again treated with TNFα (100 ng/mL) and okadaic acid (500 nM), the unimolecular

sensor curves remained at flatline, whereas most bimolecular sensor-expressing cells responded, indicating that the bimolecular layout was preferable for detecting responses (figure 3.5b). Baseline increases in FRET ratio of the bimolecular sensor, as observed before time 0 in figure 3.5b, were an issue limiting interpretation of the fold change.

In line with the drifting FRET baselines, we observed significant phosphorylation of the IκBα portion of the bimolecular sensor even in untreated cells (figure 3.5c). High basal phosphorylation is likely to increase baseline FRET ratio and may limit the dynamic range of the sensor. We hypothesized that this high baseline phosphorylation derived from a lack of reversibility of sensor phosphorylation. Whereas many FRET sensors encode a kinase substrate domain that is also subject to reciprocal phosphatase activity, endogenous p-IκBα is not dephosphorylated, but it is subject to proteolysis. The NES-tagged IκBα truncation used lacks degradation motifs, which may have inhibited clearance of the phosphorylated protein.

Optimizing a bimolecular sensor to minimize baseline phosphorylation

In order to provide an avenue for degradation of phosphorylated sensor protein, we introduced a PEST sequence from endogenous IκBα, replacing the nuclear exclusion sequence in the initial bimolecular layout (see figure 3.4a-B). With this modification, the fold increase in phospho- IκBα was much more dramatic (figure 3.6a, p- IκBα strip, lanes 7-8 vs. 9-10). YFP expression was also reduced (figure 3.6a, YFP strip, lanes 1 vs. 3, 7 vs. 9).

Rapid degradation of phosphorylated sensor components, while useful for reducing the FRET at baseline, could also hinder FRET-based visualization of phosphorylation in real time. Therefore, we treated cells expressing the PEST-tagged sensor with the proteasome inhibitor MG132 at 20 uM for one hour prior to imaging (figure 3.6b). Pretreatment rescued average YFP intensity at the start of imaging from 1400 AFU in untreated cells to 6800 AFU treated cells in 3.6b; it also appeared to potentiate greater FRET responses to TNF alpha (figure 3.6b).

In keeping with the dramatically lower phospho- IκBα signal observed by Western blot in the degradable sensor compared to the NES-tagged sensor, we observed a significantly greater average FRET response in direct comparisons between PEST- and NES-tagged IKKAR variants exposed to the same TNFα stimulus and MG132 pretreatment (figure 3.6c).

Even with a more responsive sensor, apparent TNFα response was somewhat stochastic. Exposure to the strong IKK stimulant of bacterial lipopolysaccharide following TNFα treatment led to a plausible FRET response in about one in every five cells (figure 3.6d-e). It remained to be validated whether these cells with apparent IKK activity also displayed NFκB nuclear translocation in response to inflammatory stimuli.

Limitations to IKK sensor use

In preparation to test coimaging of p65 and the IKK sensor, we coexpressed each sensor component with RFP-tagged p65, an NFκB monomer. Coimaging indicated that expression of the two sensor components together was

associated with significantly higher basal p65 nuclear/cytoplasmic ratio than p65 expressed alone or with either sensor component in isolation (figure 3.7a). This was a concerning reminder that expressing signaling components can perturb the system. Similarly, in a small sample set imaging the nuclear to cytoplasmic ratio of p65 in cells expressing or failing to express IKKAR within the same dish, it was apparent that the presence of sensor components altered signaling dynamics (figure 3.7b).

To minimize baseline IKK signaling and optimize the number of cells responding, we tested a period of serum deprivation prior to TNF treatment, borrowing from the classic NFκB literature (e.g., Ozes et al., 1999). However, a more recent publication suggests that IKK may be activated by serum starvation (Kohno et al., 2012). Moreover, we observed that serum starvation dramatically affected localization of the WDx7 sensor domain (figure 3.7c). With increasing serum deprivation of Cos7 cells, perinuclear puncta appeared in the CFP channel, which we hypothesized could represent either autophagic body formation, or unfolded and aggregated CFP-WD proteins. Successful *in vitro* translation of catalytically active full-length βTRCP in a rabbit reticulocyte lysate model system, and purification and crystallization of the WD repeat domain alone, had suggested folding of this domain was robust (Wu et al., 2003; Evrard-Todeschi et al., 2008). In any case, efforts to find a less stressful pre-imaging course of treatment, although not exhaustive, were unsuccessful.

Conclusions

Although credible FRET responses to IKK stimulation were occasionally observed in our experiments, the drawbacks of the bimolecular IKK sensor remain significant. Problems encountered in the course of this research included high basal phosphorylation of the substrate component; poor cellular distribution of the phospho-substrate binding component; and apparent interference of sensor components with endogenous signaling.

Incorporating a degradation motif and then halting its degradation immediately prior to imaging appears to have solved the problem of high basal IκBα phosphorylation. Further experimentation might inform as to whether the same goal can be accomplished with the smaller, ubiquitin-only modification to the protein shown in figure 3.3a-C. Alternatively, recent work has shown that a domain distinct from the PEST may be important in IκBα degradation (Fortmann et al., 2016), indicating that greater turnover of the phosphorylated IκBα-YFP component might be possible. On the other hand, WDx7 domain folding and/or localization failed intermittently, apparently as a result of cell stress, and we were not able to resolve the problem satisfactorily. In particular, serum starvation to reduce NFκB activation at the outset of imaging seems to have worked against our goal on this front.

To optimize these problems intrinsic to the sensor, a more promising path forward may be to combine the optimized kinase substrate domain with a more easily-folded phospho-recognition domain: for example, using the PEST- tagged IkBa component with the fibronectin-based selex product in a bimolecular sensor

format. This combination may optimize both the fold change in phosphorylated IKK substrate from untreated to treated cells, and the ease of folding of the phospho-recognition component of the sensor.

Any future efforts to generate an IKK activity sensor, however, must remain mindful of the possible perturbation to activity of the signaling pathway when introducing excess substrate and binding domains. As shown in figure 3.7a-b, expression our intermolecular sensor introduced significant perturbation to NFκB level and stimulus response. It is reasonable to suppose that the components of the bimolecular sensor could bind to, and interfere with, the endogenous molecular signaling system. An observation-induced "buffering effect" on endogenous signaling has been described and kinetically modeled for GTPase activity sensors, and there is evidence that our model system may also suffer from interference by observation (Haugh et al., 2012). Perhaps an avenue for circumventing this problem would be to engineer an intramolecular sensor optimized for low binding to endogenous protein, along an approach comparable to that described for Cameleon, above.

Figures for Chapter 3

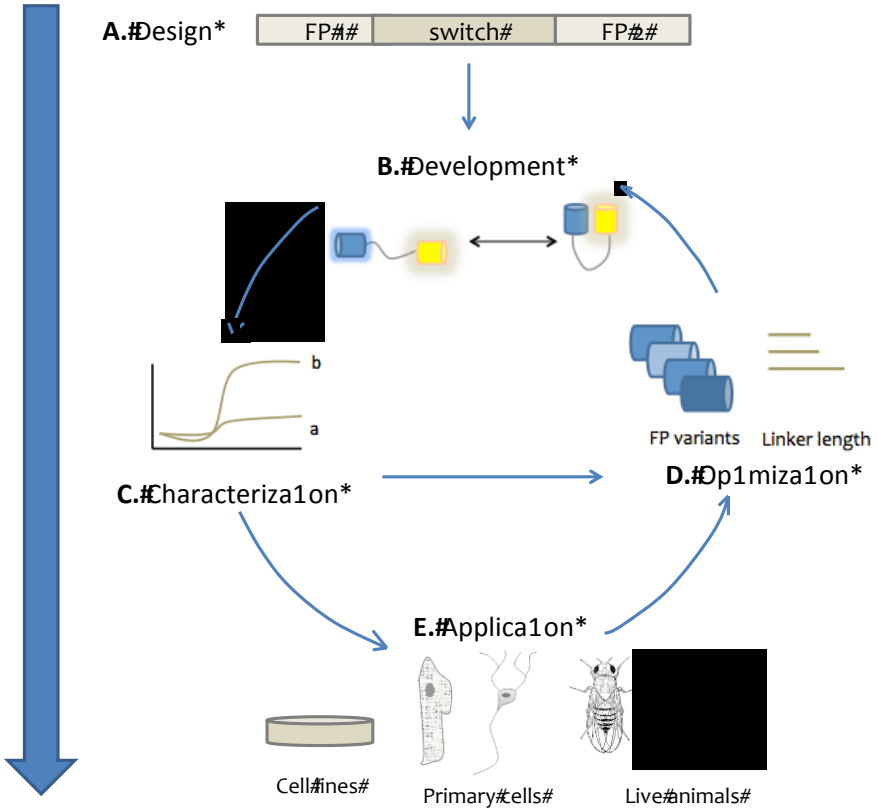

Figure 3.1 The pipeline for biosensor development. (A) Design. The majority of two fluorescent protein reporter layouts position the fluorescent protein pair around a molecular switch, either endogenous or engineered. (B) Development is typically an iterative process. (C) Initial characterization of a reporter involves measuring its response to a known stimulus of the kinase of interest; here, “a” represents an earlier version of a sensor with lower dynamic range, whereas “b” represents activity of an optimized version. (D) Optimization of a reporter may involve changing the fluorescent proteins, linker, or length/identity of the specific protein components recognizing the signal of interest. After optimization, new versions of a probe are compared to earlier versions. (E) Application of a probe in cell lines, primary cells and live animals can be both an end goal for development, and a spur to further optimization.

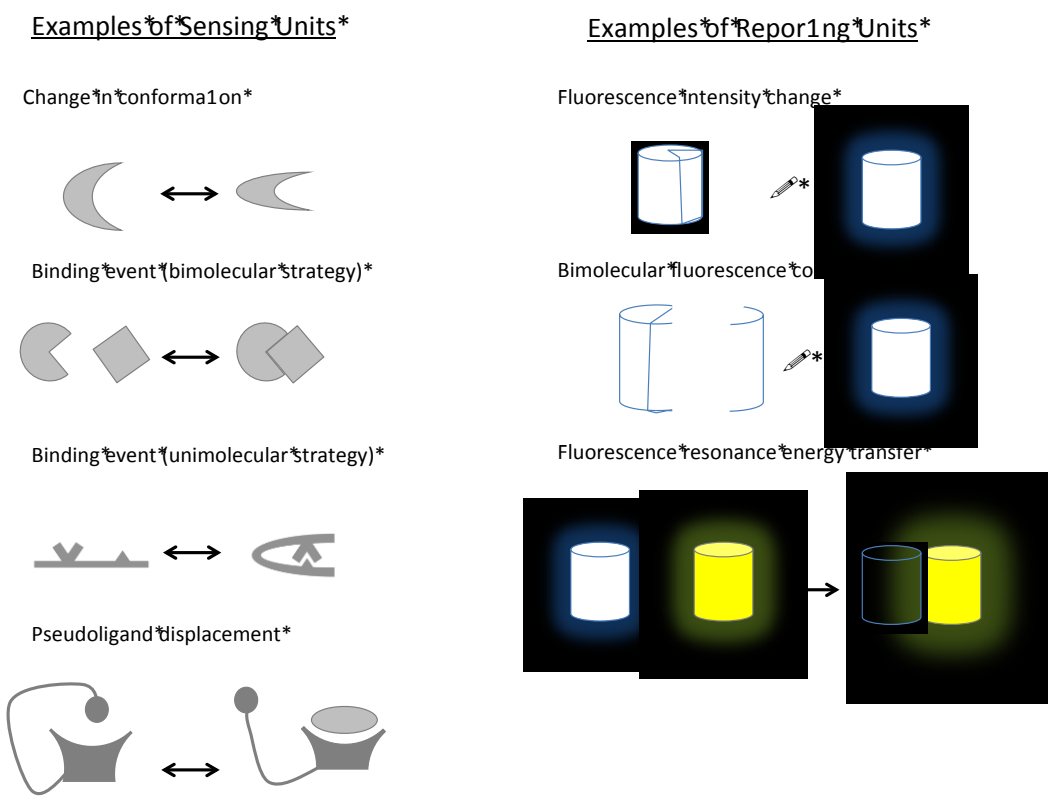

Figure 3.2 Visualizing a protein's conformational change using an engineered polypeptide sequence. (A) Sensing unit: a molecular switch, usually based on the endogenous sequence of a kinase or its substrate. On/off "switching" may occur endogenously, as in a conformational change or a binding event; or be engineered, as in a unimolecular adaptation of a binding event, or a pseudoligand displacememnt probe. (B) The reporting unit generates an optical readout, either through a change in single-color fluorescence, or by a change in resonance energy transfer. Dimerization-dependent fluorescent protein intensity changes are another visualization modality not shown here.

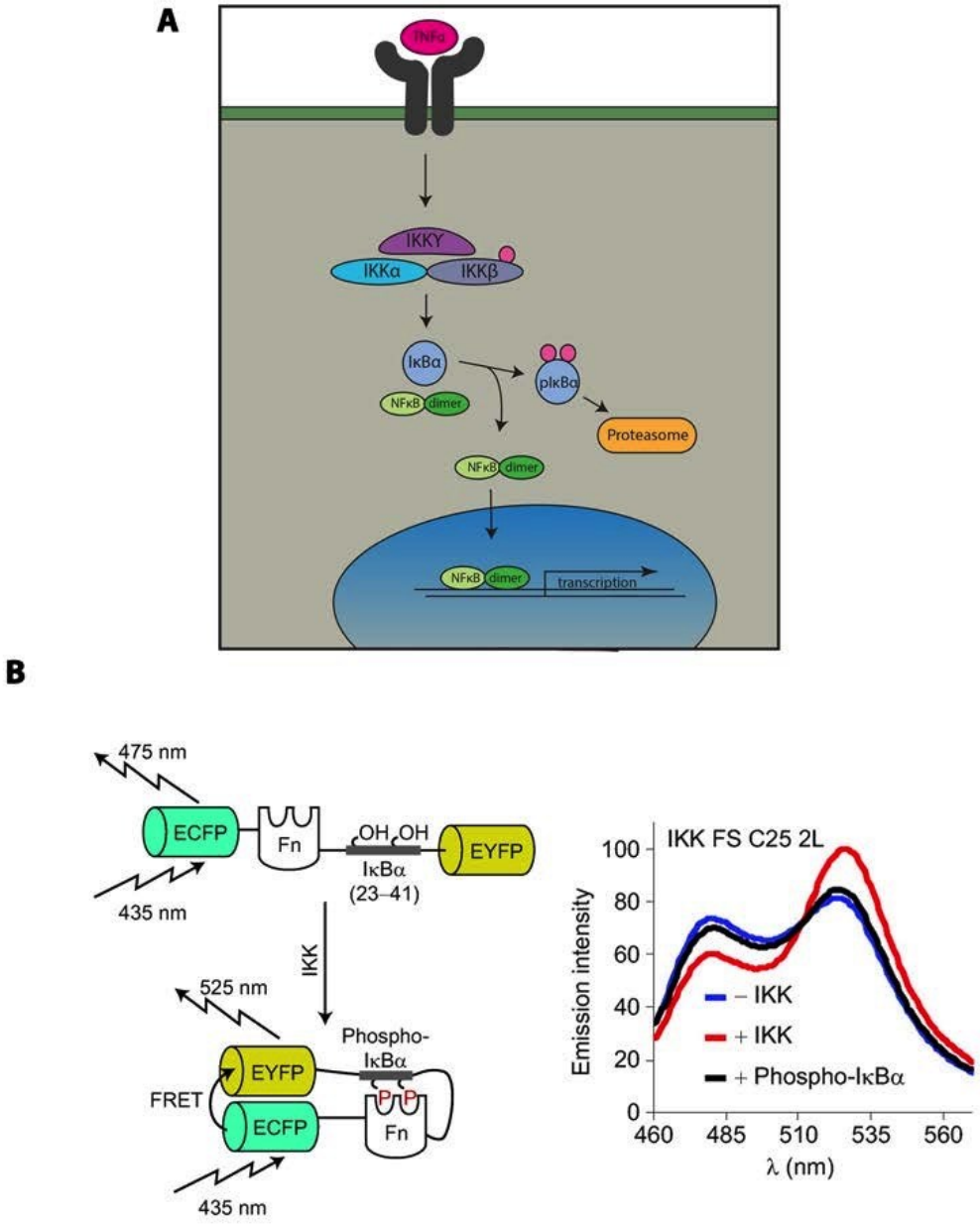

Figure 3.3. Pathways for IKK activation. (A) Canonical pathway for NFκB activation. (B) Conceptual schematic (left) and spectroscopic curves (right) of fibronectin-based IKK sensor. Reprinted with permission from Olson *et al.*, ACS Chemical Biology 2008. Copyright (2008) American Chemical Society.

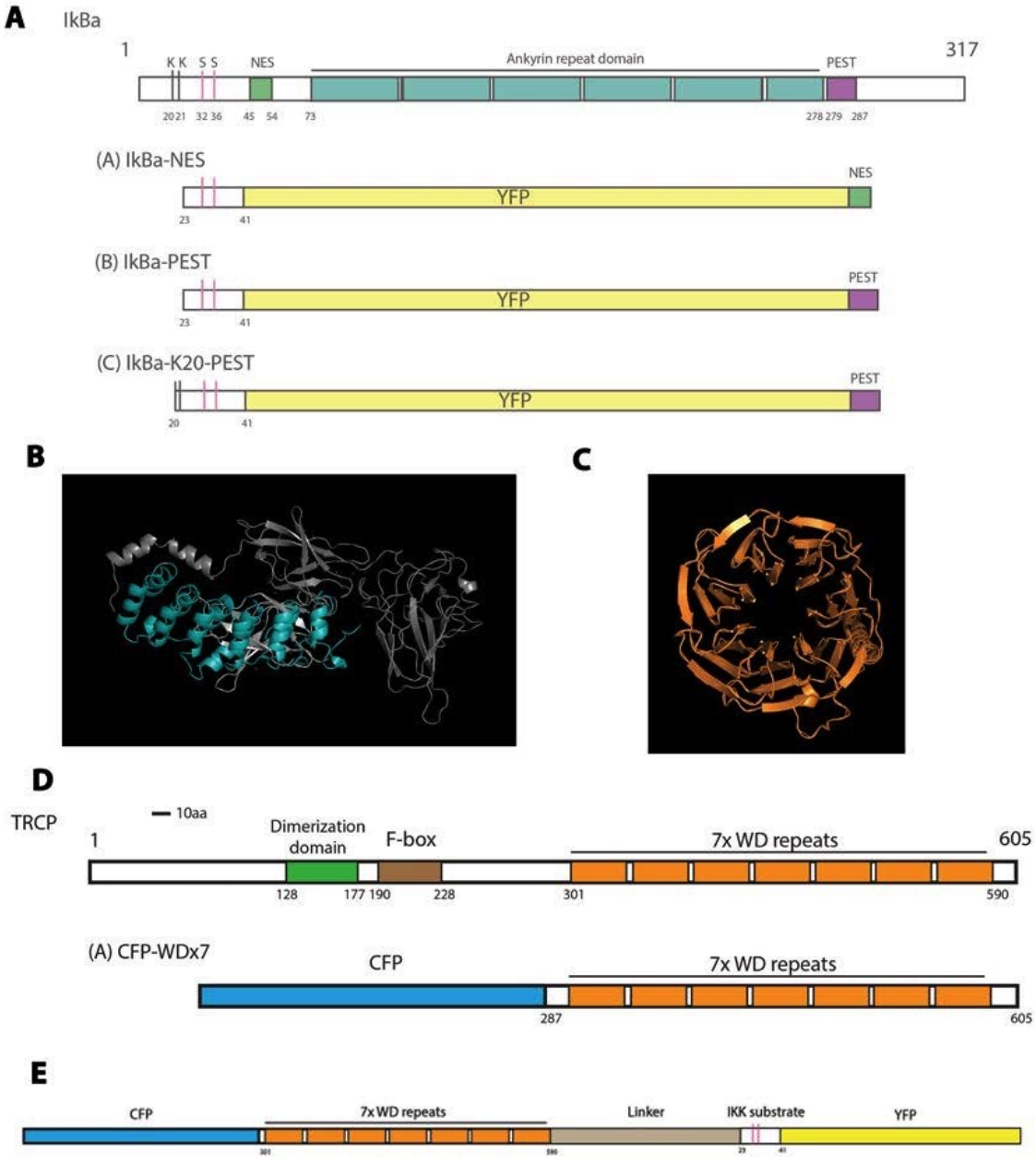

Figure 3.4. Endogenous components of an IKK sensor. (A) Domain map of IκBα and YFP-tagged truncations. (B) Crystal structure of IκBα (amino acids 70-282) in complex with NFκB heterodimer (gray) (PDB 1ikn). (C) Crystal structure of the beta-propeller sheet structure of βTRCP (orange) in complex with a phosphorylated fragment of beta-catenin (not shown) (PDB 1p22). (D) Domain map of βTRCP and CFP tagged truncation. (E) Domain map of a unimolecular IKK sensor based on βTRCP and IκBα.

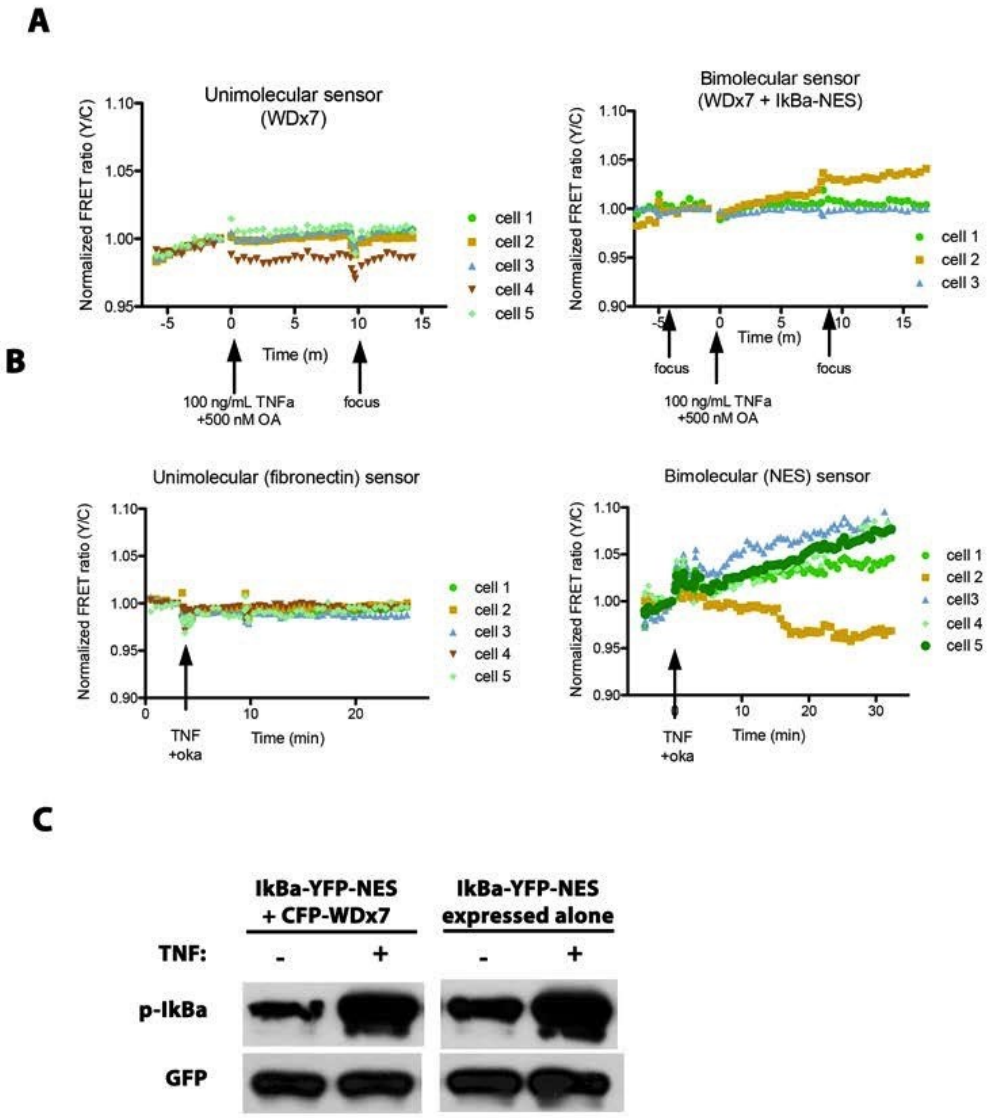

Figure 3.5. First steps toward a bimolecular IKK sensor. (A) Unimolecular sensor using IκBα -NES and βTRCP is inferior to bimolecular sensor using same components. Cos7 cells, treated with TNFα (100ng/mL) and okadaic acid (500 nM). (B) Unimolecular sensor using IκBα and SELEX-derived, fibronectin-based phospho- IκBα binding domain is inferior to bimolecular sensor using IκBα -NES and βTRCP. MEF cells, tnf 100 ng/mL, KOA 500 nM. (C) IκBα -NES is highly phosphorylated at baseline, with increases after TNFα stimulation.

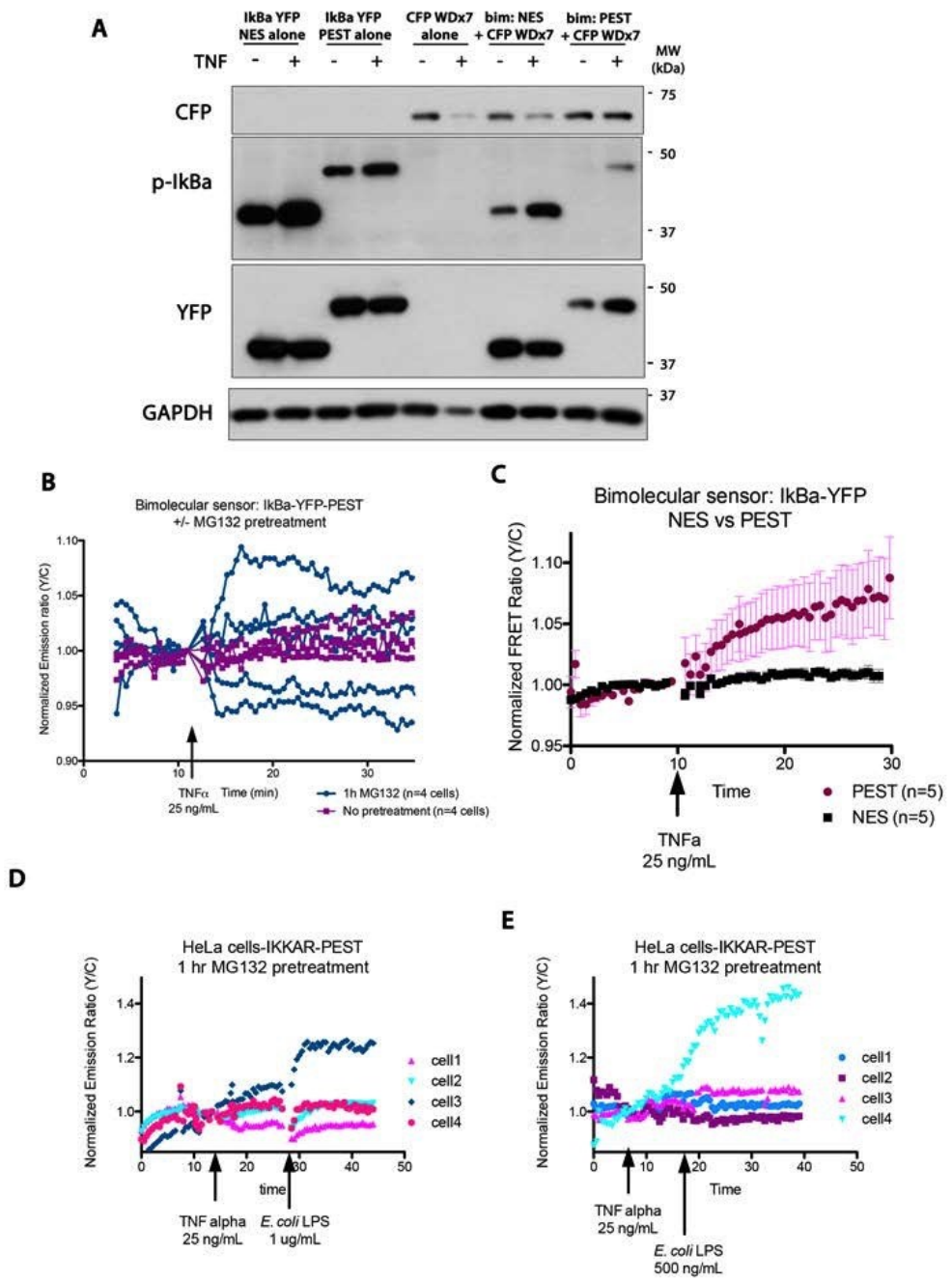

Figure 3.6. Incorporation of degradation domains. (A) Incorporation of a PEST motif reduces basal IκBα phosphorylation, driving a stronger fold increase in phosphorylation after TNFα treatment. (B) Cos7 cells expressing bim-IKKAR with a PEST domain show greater FRET response to 25 ng/mL TNFα when pretreated with MG132 (navy traces) than without pretreatment (purple traces). (C) Cos7 cells expressing bimolecular IKKAR with a PEST domain (maroon) show, on average, a stronger FRET response to TNFα than cells expressing bimolecular IKKAR with a nuclear exclusion sequence (NES, black). All cells pretreated with 20 uM MG132. (D-E) In separate experimental replicates, HeLa

cells tended to show a relatively modest response to TNFα, which could be potentiated by followup treatment with lipopolysaccharide (LPS).

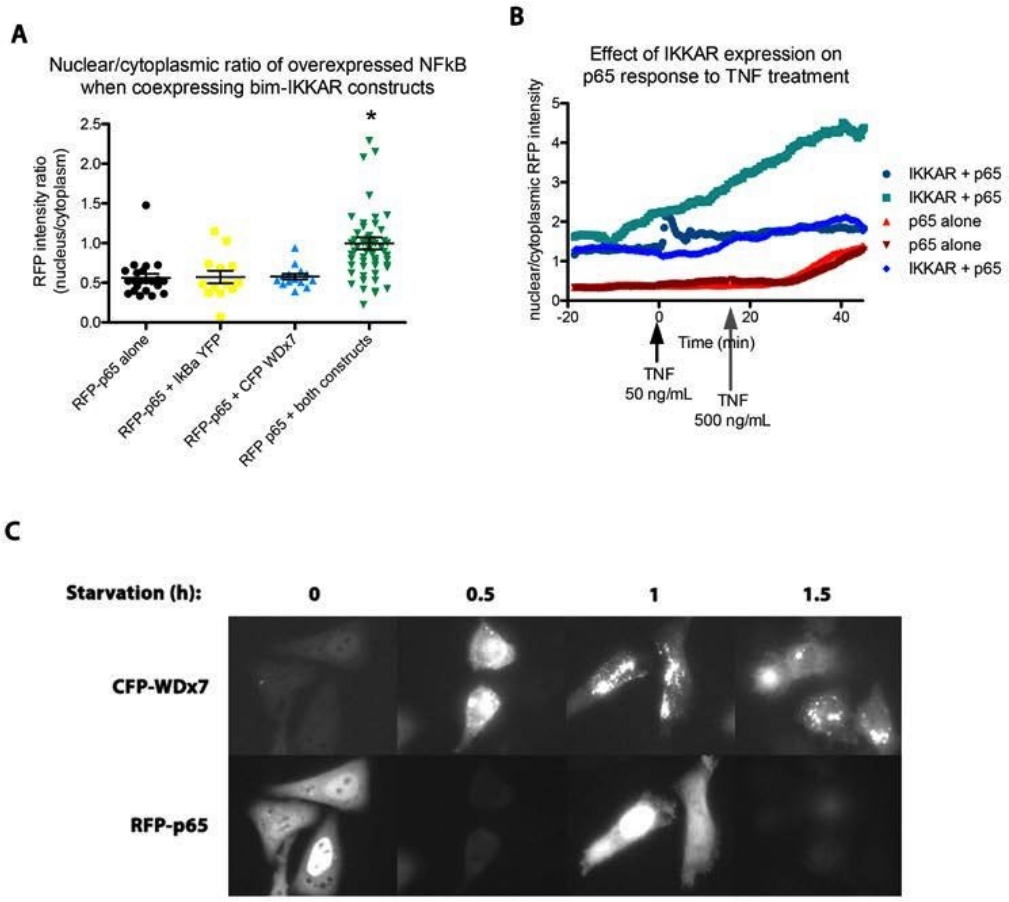

Figure 3.7. Limitations to IKKAR imaging. (A) Expression of paired IKKAR components correlates with high baseline nuclear p65 localization (* ANOVA, $p<0.05$). (B) Both starting nuclear/cytoplasmic ratio and signal-induced nuclear translocation of p65 are substantially altered in cells expressing both IKKAR components (blue traces), compared to cells expressing p65 alone in the same dish (red traces). (C) Serum starvation appears to drive formation of CFP-WDx7 puncta (Cos7 cells, no MG132).

Table 3.1 List of genetically encoded kinase biosensors for kinase activation (measured by conformational change) or activity (measured by substrate phosphorylation).

Target	Sensor name	References
Activation probes		
Akt	AktAR	Gao et al., 2008, Komatsu et al. 2011
	GFP-PKB-RFP	Calleja et al, 2007
	ReAktion	Ananthanarayan et al, 2007
B-Raf	Prin-BRaf	Terai & Matsuda, 2006
C-Raf	Prin-CRaf	Terai & Matsuda, 2005
Death associated protein kinase 1 (DAPK1)		Piljic et al., 2011
CamKII	Camui	Takao et al., 2005, Piljic et al., 2007, Kwok et al., 2008
Erk	Miu2	Fujioka et al., 2006
P21-activated kinase 1 (PAK1)	Pakabi	Parrini et al., 2009
Activity probes		
Protein kinase A	AKAR	Zhang et al., 2001… Komatsu et al., 2011
Abl kinase		Zhou et al., 2009
Akt	Aktus	Sasaki et al., 2003
	Akind	Yoshizaki et al, 2007
	BKAR	Kunkel et al, 2005
AMPK	AMPKAR	Tsou et al., 2011
Aurora B kinase	Aurora B sensor	Chu et al., 2011
ATM kinase	Atomic	Johnson et al, 2007
Protein kinase C	CKAR	Violin et al., 2003, Komatsu et al., 2011, Wu-Zhang et al., 2012
Cyclin-dependent kinase 1		Gavet & Pines, 2010
Cyclin-dependent kinase 2		Spencer et al., 2013
Protein kinase D	DKAR	Fuchs et al., 2009, Eisler et al., 2012
EGFR		Ting et al, 2001,
Erk	Erkus	Sato et al, 2007
	EKAR	Harvey et al. 2008, Komatsu et al., 2011
	REV	Xu et al., 2013
Focal adhesion kinase (FAK)		Seong et al., 2011
Inhibitor of kappa B kinase (IKK)		Olson et al., 2008
Insulin receptor	Phocus	Sato et al., 2004
	Sinphos	Kawai et al., 2004
c-Jun N-terminal kinase (JNK)	JNKAR	Fosbrink et al., 2010, Komatsu et al., 2011

MAPK- activated protein kinase 2 (MK2)	GMB	Neininger et al., 2001
Microtubule affinity regulating kinas (MARK)		Timm et al., 2010
Myosin light-chain kinase (MLCK)	exMLCK	Geguchadze et al., 2004
Phosphoinositide-dependent kinase 1 (PDK1)	GFP-PDK1-RFP	Calleja et al., 2007
Polo-like kinase 1	Plk sensor	Macurek et al., 2008
RSK	Eevee-RSK	Komatsu et al., 2011
S6K	Eevee-S6K	Komatsu et al., 2011
Stress-activated protein kinase kinase kinase	SAP3K activity reporter	Tomida et al., 2009
Src	Src biosensor	Ting et al, 2001,, Wang et al, 2005, Ouyang et al., 2008

Chapter 4. Conclusions and perspectives

Outlook for lin28a/TRBP interaction

We have characterized an interaction between Lin28a and TRBP that depends on Erk-induced phosphorylation of TRBP and also Lin28a phosphorylation. There is considerable precedent for the mediation of other TRBP binding partners through kinase activity: for example, in TRBP binding to Dicer, PACT and PKR (see chapter 1). The effect of Lin28a phosphorylation on its interactions is comparatively unexplored.

Preliminary phosphomutant experiments (figure 2.3H-I) suggest that the biosensor is in fact a dual sensor, with maximal interaction between Lin28a and TRBP mediated by phosphorylation of both proteins. It is counterintuitive to imagine that addition of a highly electronegative phosphate group to each of two small binding partners increases their attraction to one another. However, perhaps phosphorylation drives a significant conformational change in one or both sensor components, revealing a binding domain that is otherwise occluded. Dual phosphorylation adds a layer of complexity to any molecular model of the Lin28a/TRBP sensor: instead of a switch with two states, as described in the section of chapter 3 on designing a probe, the sensor now represents a switch with numerous possible conformations. That is, phosphorylation status of both Lin28a at serine 200, and TRBP at serine 152 may contribute to overall strength of binding. Experiments to test FRET efficiency in Lin28a phosphomutant and phosphomimic constructs are ongoing, and their results are anticipated with eager interest. One kinetic correlate of a sensor reporting two phosphorylation

events, is that if the two phosphorylation reactions proceed at different rates, a slower FRET increase might be expected compared to a single phosphorylation sensor. In effect, the sensor would report on a second-order rather than a first-order reaction. Indeed, we observed slow binding kinetics in the Lin28a/TRBP sensor compared to an Erk sensor. We wonder which is the rate-limiting Erk substrate, and whether factors beyond kinase activation and localization may affect phosphorylation rates. For example, does the RNA binding status of lin28a C terminus affect its availability to be phosphorylated?

From a more biological standpoint, we wonder about the relative importance of phosphorylation of each protein in the observed physiological output of heightened Lin28a levels downstream of Erk activity. Is there a meaningful difference between instances when lin28a alone is phosphorylated and stabilized, and those when TRBP phosphorylation coincides with lin28a stabilization? The modest increase in Lin28a level consistently observed in TRBP deficient cells after Erk activation with PMA (figure 2.2) suggests that Lin28a can respond to Erk stimulation in the absence of TRBP. In contexts where TRBP is not overexpressed, but present at endogenous levels, what is its quantitative impact on Lin28a level?

Another interesting question is whether the interaction between Lin28a and TRBP, and the increase in Lin28a protein levels it potentiates, primarily exerts downstream effects through upregulation of microRNA biogenesis, or through other modes of Lin28a activity. Endoplasmic reticulum associated translation is one system in which Lin28a and TRBP exert similar influences, and

may interact. TRBP phosphorylation in the peri-endoplasmic reticulum is known to increase JNK and PKR activity, reducing translation; while TRBP also potentiates microRNA biogenesis in the rough endoplasmic reiticulum (Nakamura et al., 2015; Stalder et al. 2013). Meanwhile, Lin28a has been shown to suppress translation through mRNA binding in the endoplasmic reticulum in the secretory pathway within embryonic stem cells (Cho et al., 2012) If heightened interaction between Lin28a and TRBP were observed in the peri-endoplasmic reticulum, it might suggest an interesting role for spatial control of this interaction in known functions of each protein.

A limitation of all of the experiments discussed in this dissertation is that they used overexpressed, affinity-tagged constructs, and therefore cannot be directly compared with endogenous cellular signaling systems. It is possible, although unlikely, that we may have measured ectopic interaction of two proteins that never in fact interact in a cellular context—for example, if they are confined in different cytoplasmic compartments. Moreover, the bimolecular protein/protein interaction sensor approach has limitations and drawbacks. For example, we could not observe Lin28a/TRBP interaction in a neuronal context; however, failure of the two halves of the probe to colocalize evenly throughout neurons makes this result inconclusive.

Further development of the Lin28a/TRBP biosensor might focus on the tradeoffs of intramolecular versus bimolecular sensor formats. In general, bimolecular sensors have higher dynamic range than their unimolecular counterparts (Depry et al., 2015). It is not yet clear whether the benefit a

unimolecular sensor offers for *in vivo* characterization of Lin28a/TRBP interaction, by forcing colocalization of both components, will outweigh the probable loss of dynamic range apparent from an increase in basal FRET efficiency (figure 2.6e). In either case, it is essential to ascertain that the final product is used in biologically meaningful settings by validating the expression of TRBP and, especially, Lin28a in any cellular context to be assayed.

Outlook for IKK sensing

Limited work on the problem of an IKK sensor suggests that the designer of a biosensor must be flexible in selecting from naturally-derived and engineered sensor components. The synthetic unimolecular probe developed by Olson *et al*., which restricts endogenous sequence to the IKK substrate, displays high basal FRET when expressed in cells; this problem had to be solved by introducing endogenous IκBα turnover mechanisms. On the other hand, the endogenously-derived phosphopeptide binding domain investigated in this work was not reliably expressed. As described in chapter 3, a reasonable compromise might be to combine the optimized IκBα peptides with the better-expressing phospho- IκBα binding protein derived from fibronectin. Future tinkerers with an IKK probe might benefit from trying such a combination.

That said, the need for a reversible mechanism of clearance for basal probe activity, such as the MG132-reducible turnover of the phosphorylated IKK substrate, introduces an additional perturbation of the system with treatment.

Another limitation to this study is the disruption of NFκB signaling that we observed (figure 3.8). Historically, observer-induced disruption to NFκB signaling has been ameliorated using knock-in NFκB-FP constructs rather than overexpressed transfected constructs. Preliminary data suggest that knock-in approaches may be feasible for biosensor imaging, and we anticipate interesting work in this arena.

Another option is to forego measurement of IKK substrate phosphorylation and focus instead on the phosphorylation status of the IKK activation loop. This approach would provide a readout of kinase activation, rather than kinase activity—a subtly distinct measurement (see chapter 3). Such reporters exist for a number of enzymes (see table 3.1), some of whose activity has not also been captured in activity reporter form.

Development of a functional sensor for IKK activity is far from complete, and experience indicates that the way forward may not be direct. However, the questions that such a sensor could address are numerous and interesting. For example, mathematical models indicate that different profiles of IKK activation may mediate changes in the dynamics of various IκB/NFκB pairs, allowing for varied responses to inflammatory stimulants (Alves et al., 2014). A sensor would help to test model-based predictions about the signaling that drives these IKK activity profiles.

Outlook for FRET biosensors of kinase activity

As a review of studies into well-studied kinases such as PKA, CaMKII and Erk makes clear, kinase activity reporters can be an extraordinarily useful tool for

understanding the target enzyme and its adaptors, modulators and cofactors. As new probes are developed, and existing probes optimized for primary culture and in-vivo imaging, we anticipate similarly diverse findings in many pathways. Progress is underway at many points in the biosensor development pipeline, from target selection through optimization to live-animal applications.

Our experience underlines the dual uses of a novel biosensor. In the absence of a well-characterized, structurally defined interaction between Lin28a and TRBP, it was initially possible to misinterpret FRET changes in the Lin28a/TRBP sensor as driven exclusively by TRBP phosphorylation, which had been previously described, and focus biosensor development on imaging in physiological contexts. Subsequent data suggest that phosphorylation of both sensor components is necessary, complicating our understanding of this interaction (figure 2.3H-I). The availability of the biosensor offers the potential to rapidly assay mutant constructs to test new hypotheses regarding post-translational modifications to Lin28a.

Work in this thesis highlights the challenges of minimizing perturbations while maximizing signal-to-noise ratio in visual readouts of cellular signaling systems. Surprisingly few publications have formally addressed this problem. However, our observation of IKKAR-associated perturbation of baseline NFκB localization suggests that overexpressing small functional domains of signaling proteins may be sufficient to change the dynamics of the whole system. A study concerned with biosensors that bind to third-party analytes found that, in a computational model, expressing an excess of biosensor would significantly alter

the accumulation and diffusion of the analytical target, while expressing too little biosensor would saturate the fluorescence readout (Haugh, 2012). While the buffering effect of a sensor made to be enzymatically modified itself, rather than binding an external molecule, may be less dramatic, based on the perturbations to NFκB ratio we observed, the disruptive principle evidently remains relevant.

Another theme in this work is the difference in signal using bimolecular compared to intramolecular sensors, even if these sensors are otherwise identical. In general, intramolecular sensors display greater baseline FRET, both because tethering increases the effective concentration of the binding components, and because the fluorophores start in closer proximity even without basal binding. However, intramolecular sensors may also potentiate faster FRET kinetics and reduced off-target binding to cell system components. Therefore, as noted in chapter 3, the best format for a sensor may depend on the use case.

For the purposes of optimization, structural studies of extant probes will be important to advance our understanding of sensor technology and settle open questions about how probes function. For example, a small-angle X-ray scattering (SAXS) study with the calcium sensor TN-XXL showed that distance played a greater role than orientation in the FRET efficiency of the calcium-free form of the sensor (Geiger et al., 2012). Further insight into what specific conformational changes lead to the greatest FRET change will be beneficial for future probe design; another recent study used SAXS assessment of the distance between fluorescent proteins in a probe's off-state and on-state to

predict the maximal expected FRET change (Mertens et al., 2012). Such information will enable rational design and modification of future probes.

Some genetically encoded biosensors have been used in high-throughput compound screens (reviewed by Robinson et al., 2014). Further enhancement of the dynamic range could facilitate this application in cellular contexts to complement FRET-based inhibitor screens using synthetic sensors outside of the cellular context (e.g., Gratz et al., 2011). Another application of genetically encoded sensors where we expect to see further advancement is kinase inhibitor candidate validation (e.g., Timm et al., 2011), including validation of inhibitors' isoform specificity (Tsalkova et al., 2012), and analysis of pharmacokinetics in *in vitro* or *in vivo* models (Nobis et al., 2013).

In vivo imaging of FRET biosensors within living animals is now a practical proposition (Day et al., 2016). The reduction in signal-to-noise ratio and dynamic range observed in many in vivo systems necessitates probe optimization and modification, for example, red-shifting of sensors (Lohse et al., 2012). It is important to keep in mind that improvements in one parameter may come at the cost of others, and that different versions of a sensor may be best suited to different applications. We look to the explosion of live animal studies with genetically encoded calcium indicators (reviewed by Palmer et al., 2011; Tian et al. 2012) as a model for the way forward with kinase sensors. In particular, iterative optimization has proven successful for genetically encoded calcium indicators, where often an early version shows very weak response in live animals, but subsequent versions are more effective. Advances in *in vivo*

imaging technology, used in combination with improved probes, will further expand the reach of kinase and phosphatase sensors. *In vivo* imaging that can be carried out over developmental time-courses, using lower illumination; in intact tissues, using higher-penetrance illumination techniques; and in freely behaving animals, using flexible optical devices, will be key to our understanding of signaling in the context of systems that are difficult to model *in vitro*.

In conclusion, fluorescence-based biosensors have come a long way, and continue to shine a light on cellular activity. We anticipate a fruitful future for these tools in expanded applications, yielding many more lessons about the regulation of kinase signaling.

Appendix 1: extended experimental methods

Restriction Cloning

TRBP truncations (as published (Daher et al., 2001) were N-terminally tagged with myc (MEEQKLISEEDL), or fluorescent proteins Cerulean (Rizzo et al., 2004), Cerulean-3 (Markwadt et al., 2011), or ECFP (Llopis et al., 1998). Lin28a truncations were derived from FL-Lin28a (Amen et al., 2017) by PCR and tagged with flag (DLYDDDKD) at the N terminus or YFP variants Venus (Nagai et al 2002), Citrine (Griesbeck et al., 2001), cpVenus-E172 and cpVenus-L194 (Nagai et al 2004) at the C terminus. EKAR ratiometric Erk sensor was a gift from R. Campbell (Addgene plasmid #60974).

PCR primers were designed using SerialCloner or Snapgene and checked for secondary structure, self-dimerization and heterodimerization using the OligoAnalyzer web tool provided by IDT. When restriction sites were added through PCR, PCR protocol was designed so that the first cycle matched the initial primer/template annealing temperature, and subsequent cycles matched the full-primer melting temperature. For example, a protocol frequently used to amplify fluorescent proteins was as follows:

Temperature	**Time**
98	0:30
95	0:10
51	0:30
72	0:45

98 *	0:10
64	0:30
72	0:45
Go to *	30x
72	5:00
4	forever

When subjecting PCR products to restriction digest, 40 uL kit-purified PCR product was digested with at least 2 uL FastDigest restriction enzyme in 1x Cutsmart buffer for 1-3 hours at 37C. Plasmid vectors were digested (1 ug) using 1 uL of each of two FastDigest restriction enzymes in 1x CutSmart buffer with at least 30 uL reaction volume. After 1 hour digestion, shrimp alkaline phosphatase (SAP, 1 uL) was added. Restriction fragments were resolved in a 1% agarose gel in SB buffer. Agarose was melted and fragments were recovered using a gel purification kit.

Plasmid/insert ligations were prepared using T4 DNA ligase in a 10 uL reaction volume. DNA needed for the specified molar ratio of vector:insert (usually 1:3; 1:1 and 1:10 were used to optimize recalcitrant reactions) was calculated using a web tool provided by the University of Dusseldorf Molecular Biophotonics Group. http://www.insilico.uni-duesseldorf.de/Lig_Input.html. Where possible, 50 ng vector was used. If combining adequate vector, insert and buffer exceeded 10 uL reaction volume, less vector was used. After 15 minutes-1 hour

ligation at room temperature, or overnight ligation at 16C, 5 uL ligation product was transformed into homemade transformation-competent bacteria (see below).

Site-Directed Mutagenesis

Phosphomimic and phosphomutant versions of all TRBP and Lin28a constructs were derived from wild-type versions of these constructs, using a modified version of the protocol presented by Huang and Zhang (2016).

Protocol: first, 100 uM primer was phosphorylated in the following mixture at 37C for 30 minutes to 1 hour.

Reagent	**volume**
100 uM primer	5 uL
10x T4 PNK buffer	5 uL
10 mM ATP	5 uL
ddH20	34 uL
T4 polynucleotide kinase (PNK)	1 uL
Total	50 uL

After phosphorylation, primer was used to make site-directed mutagenesis reaction mixture:

Reagent	**Volume**
Phosphorylated primer (from step 1)	1 uL
DNA template	0.2 ug in 1 uL
10x Pfu Buffer	1 uL
10x Taq Ligase Buffer	1 uL
2.5 mM dNTPs	1.5 uL
Pfu DNA polymerase	0.5 uL
Taq ligase	0.5 uL
ddH2O	To 20 uL

Mutant template was created by PCR using the protocol “QuickA.”

Temperature	**Time (m)**
65	5:00
96	0:30
96 *	0:30
55	1:00
65	8:00
72	10:00
Go to *	30x
10	forever

Remaining methylated template was digested for 1 hour at 37C using 1 uL Fast Digest (FD) Dpn1. Then the tube was returned to the thermocycler for PCR protocol “QB”:

Temperature	**Time (m)**
65	5:00
96	0:30
96 *	0:30
55	1:00
68	15:00
72	10:00
Go to *	2x
18	forever

Mutant products were transformed into commercially available highly competent cells.

Bacterial transformation

Aliquots of bacteria competent for transformation (stored at -80C) were thawed on ice, and up to 5 uL ligation product or plasmid prep was added to aliquot under flame-sterile conditions. After 15 to 30 minutes on ice, this mixture was heat shocked at 42 C for 45 seconds, then returned to ice for a two to three minute recovery period; warmed LB+ was added under flame-sterile conditions, and cultures were rotated for 30 minutes to an hour at 37C before plating onto antibiotic-supplemented LB agar plates.

Cell culture

HEK 293T cells were cultured in DMEM supplemented with 10% FBS and peneillin/streptomycin, and transfected as described (Amen et al., 2017). For stabilization experiments, 45,000 cells per well were seeded onto 24-well culture plates, and transfected using the calcium phosphate protocol 18 to 24 hours after plating. Media was changed 8 to 16 hours after transfection, and cells were harvested 36 hours after transfection (for experiments testing only coexpression) or up to 48 hours after transfection (for experiments requiring, e.g., 24 h treatment). When multiple truncations of the same protein were expressed for the same experiment, transfection levels were optimized to equalize affinity tag level in lysates from different truncations. Total DNA transfected was equalized between conditions using empty pcDNA vector.

Mouse tail epithelial fibroblast cells (TEFs) lacking endogenous murine TRBP (*Tarbp2* KO) (gift of A.Gatignol, (Daher et al., 2009)) were cultured in DMEM with 10% FBS supplemented with penicillin, streptomycin and amphotericin B. Cells were seeded at 15,000 cells per well in 24-well plates, followed by lipofectamine LTX Plus transfection according to manufacturer protocol.

For neuronal imaging experiments, murine hippocampal neurons were cultured as described (Amen et al., 2017). Briefly, hippocampi were isolated from neonatal ICR mice, then neurons were dissociated using papain and physical dissociation, and plated at 180,000-200,000 cells per dish in polylysine-coated

MatTek imaging dishes. Neurons were cultured in Neurobasal A medium supplemented with B27 and glutamine, with penicillin/streptomycin for the first 24 hours. After 13-14 days in vitro, neurons were transfected using lipofectamine 2000 according to manufacturer protocols. Imaging was completed 24-28 hours after transfection.

Immunoblotting

Cultured cells were washed in cold PBS and harvested on ice with lysis buffer (50 mM HEPES, 150 mM NaCl, 10%Glycerol, 1 mM EDTA, 1% Triton X-100, 0.2% SDS) plus protease inhibitor cocktail (Roche 11836170001), and phosphataseinhibitors (sodium orthovanadate 0.2 mM, sodium pyrophosphate 1 mM). Protein concentration was determined by Bicinchoninic acid (BCA) assay and equal protein amounts resolved on SDS-PAGE gels and electrotransferred to PVDF membrane. Membrane was blocked with 5% BSA in Tris-buffered saline tween 20 (TBST 0.1%) for 1-3 hr and probed with primary antibodies: c-Myc (Lifetech 132500), FLAG (Sigma M2, F3165) TRBP (Abcam ab72110,or Proteintech 15753-1-AP), Phospho-TRBP (custom), Hsc70 (Santa Cruz sc7298). All immunoblots were scanned and quantified without image adjustment. For representative image figures, image levels were uniformly and minimally adjusted for visual clarity in some instances.

Immunoprecipitation from cells

For FL-Lin28a co-immunoprecipitation of TRBP and its truncations, mouse anti-flag M2 antibody (Sigma) was adhered to protein G sepharose beads overnight after blocking with 5% BSA for 1 hour. HEK 293T cells coexpressing the constructs of interest were harvested in coIP lysis buffer (100 mM KCl, 4 mM MgCl2, 10 mM HEPES (pH 7.3), 50 uM ZnCl2, 0.5% NP-40) with protease inhibitor cocktail (Roche), and phosphatase inhibitors (Sigma, phosphatase inhibitor cocktail 2 and 3). Insoluble material was first removed by centrifugation (10,000 g) and lysates pre-cleared by rotation (4 °C, 1 hr) with unblocked sepharose beads. Equal masses of protein in pre-cleared lysates were brought to equal volume, added to flag antibody-coated beads, and rotated (4 °C, 3-4 hr). After washing 3x with coIP wash buffer (150 mM NaCl, 1 mM MgCl2, 50 mM HEPES (pH 7.8), 50 uM ZnCl2, 0.05% NP-40), immunoprecipitated material was eluted at room temperature using 1x flag peptide (Sigma F3290) diluted 1:30 in coIP wash buffer. Protocol is reproduced below.

Protocol for immunoprecipitation

Day Prior to Immunoprecipitation

1. Aliquot 30 uL 50% sepharose bead slurry per IP reaction
2. Block beads for 1 hour, rotating at 4C, in coIP buffer + 5% BSA
3. Pellet beads (spin 200rpm for 25 sec at 4C, suction off supernatant with thin-gauge needle or a p10 tip). Rinse with 1.5 mL chilled coIP buffer.
4. Pellet beads and resuspend in 30 uL per reaction, plus 5 ug antibody per reaction.

Day of Immunoprecipitation

Prepare beads

1. Aliquot beads for pre-clearing (20 uL 50% slurry per reaction)
2. Wash antibody-coated beads from day 1 and preclearing beads twice with 1.5 mL chilled NT2 (invert, spin 2000 rpm for 25 sec 4C, suction off buffer with needle & repeat)
3. Resuspend beads in 2x excess of NT2 + protease/phosphatase inhibitor + NEM (30 uL per 15 uL beads)

Lyse cells

1. Wash cells with ice-cold PBS + 0.9 mM MgCl2 (be very gentle; if cells lift off, pellet them and add back to lysis buffer later.)
2. Harvest cells in polysomal lysis buffer + protease inhibitors, phosphatase inhibitor, 1 mM DTT.
    1. For 24-well plates, use 50 uL per well (70 uL for first well)
    2. For 10-cm dishes, use 750 uL per dish
3. Let cells sit in lysis buffer on ice 10 min, scrape and rotate at 4 C 10 minutes
4. Centrifuge lysate at 13.2k rpm, 4 C for 15 minutes. Remove supernatant.
5. Begin pre-clearing on supernatant (less 1 uL for Bradford assay-see step 6). Pre-clear with 15 uL beads (=45 uL 33% suspension). Incubate, rotating, at 4C for as long as Bradford and calculations take.

6. Bradford assay to determine concentration. 1 uL lysate : 200 uL Bradford reagent, invert 2-3x and incubate RT 10 minutes.

Immunoprecipitate

1. Calculate volume for 1.5 mg protein per reaction; bring all samples to equal volume/concentration with extra lysis buffer (smaller volume = better IP!).
2. Spin cleared lysate 2000 rpm for 1 minute at 4 C and remove cleared lysate to a new tube.
3. Take two 2.5% input sample (2.5% of volume transferred, divided by 3 for 3x elution).
4. Add 45 uL antibody-bound beads (15 uL in 33% suspension) to appropriate volume of cleared lysate.
5. Incubate, rotating, 3½ hours at 4 C.

Wash

1. Spin down, take cleared lysate sample (2.5 % of (volume transferred + 30 uL), divided by 3 for 3x elution)
2. Wash 2x with 1.5 mL ice cold NT2 + protease and phosphatase inhibitors; after each wash, invert to resuspend, spin beads at 2000 rpm 4 C for 25 s.
3. Wash a third time with 1.5 mL ice cold NT2 + protease and phosphatase inhibitors – this time rotate at 4C 10 minutes before removing supernatant. *(NB: if adherence is low, skip this step).*

4. Wash 1x with cold NT2 **without** protease/phosphatase inhibitors; spin for 1 minute at 2000rpm at 4 C, and remove buffer entirely with vacuum suction. (err on the side of leaving buffer rather than suctioning up beads; may remove last 30uL or so with pipettor instead!)

Elute with Flag peptide

1. Add 30 uL of 1:30 dilution of Flag peptide in NT2; rotate 30 min at room temp
2. Spin 10 sec, 12000 rpm at room temp. Collect 30 uL eluent.
3. Repeat 2x (total 90 uL eluent)
4. Combine eluents and spin for 10 sec at 2000 rpm
5. Pipet off 30 uL eluent
6. Boil samples with loading dye for SDS-PAGE analysis.

In vitro immunoprecipitation of recombinant proteins

For in vitro characterization of binding between TRBP and lin28a truncations, full-length GST-TRBPdD or GST peptide only were harvested from BL21 *E. coli* (see protocol below) and purified over glutathione sepharose resin (GE Healthcare) according to manufacturer protocols, eluted with 10 mM glutathione at pH 7.4, and dialyzed to remove glutathione. 6x-histidine tagged lin28a and truncations were likewise harvested and purified using cOmplete His-Tag purification resin (Roche) according to manufacturer protocols and eluted with 100 mM imidazole, again followed by dialysis.

For *in vitro* immunoprecipitation, equimolar 6xHis-tagged lin28a truncations (equimolar to a 50 ug mass of lin28a-3) were bound overnight to Ni-NTA bead slurry, then mixed with 100 ug GST TRBP dD or equimolar GST peptide and rotated for 3 hours at 4C in PBS. Mixture was washed with 20x bead volume and then eluted with high concentration imidazole or by boiling in SDS gel loading buffer. Protocol for protein purification and binding assay are reproduced below:

Protocol for protein purification:

Day 1:

1) Inoculate 10ml TB plus antibiotic with 1 colony from BL21 bacteria transformed with plasmid of interest

    Note: Touch pipette tip to colony, then touch tip to 5ml LB/antibiotic liquid culture and eject tip in a second 5ml LB/antiobotic liquid culture

Day 2:

1) Inoculate 250ml TB/antibiotic with 10ml starter culture from Day 1. Grow at 37°C
2) Monitor bacterial growth until OD 600 = 0.75 (logarithmic phase, usually about 2 hrs of growth)
3) Once OD 600=0.75, add IPTG to final concentration of 1mM to induce plasmid expression, and grow for 2 - 4 hrs
4) Cool bacteria quick on ice water bath for 15-25 min

5) Spin down bacteria at 7700 x g for 10 min at 4°C
6) Resuspend bacterial pellet in 12.5ml cold PBS, pH=7.4

    Note: At this step, bacterial resuspension can be stored overnight at -20°C to aid lysis. Alternatively, experimenter can proceed immediately to the subsequent steps

Day 3:

Lysis

1) Quick thaw bacteria at 37°C
2) Add bacterial protease inhibitors to recommended concentration, and lysozyme to 0.5mg/ml
3) Incubate 30 min room temp
4) OPTIONAL: freeze bacteria and thaw at 37°C 2-3X to aid lysis
5) Sonicate: 20 sec pulses X 5, at 20% amplitude
6) Add Triton-X to 1% and incubate on ice 0-10 min
7) Spin 10,000 x g for 10 min at 4°C. Take supernatant for analysis.

    Note: If desired, save supernatant sample for analysis of protein expression

Pull-down

1) Wash 1200 uL 30% bead slurry with PBS, pH=7.4 (about 400uL bed volume of beads; glutathione sepharose beads for GST binding, or Ni-NTA beads for 6x His binding).

2) Allow beads to settle into a pellet on ice (approx. 15 minutes); resuspend beads as 25% slury in PBS, pH = 7.4 (i.e., 1200uL PBS to 400 uL bed volume of beads)

    To expedite, beads may be pelleted with a 30 second spin at 2500 rpm at 4 C.

3) Add 12.5ml lysed bacterial supernatant to 1600μl 25% slurry of appropriate beads
4) Rotate beads and supernatant at 4°C for 2hr-overnight

Ni-NTA column elution:

1) Spin down Ni-NTA beads at 500 x g for 5 min at 4°C and decant supernatant

    Note: Save supernatant sample for analysis of % protein pull-down

2) Re-suspend beads in small volume PBS, pH=7.4 (around 500μl) and apply to Biorad Poly-prep chromatography column
3) Wash with 8ml PBS + 25 mM imidazole, pH=7.4 (20X bead volume) and collect drainage

    Note: Save wash drainage sample to confirm protein is not lost

4) Elute using one bed-volume into 200μl fractions with freshly made 250 mM imidazole in 1x PBS, pH 7.4

    a. Plug column before addition of each elution fraction, and incubate 50-10 min before collecting elution

b. Add 1μl eluted fraction to 100μl Bradford reagent to preliminarily select for concentrated fractions.

NB: BCA reagent cross-reacts with both glutathione and imidazole.

5) Pool most concentrated fractions and subject to dialysis at 4°C to remove imidazole
    a. Dialysis buffer: 20mM HEPES pH=8.0, 20% glycerol, 0.2 mM EDTA, 1mM DTT
    b. Use slide-a-lyze tubes with 20K pore size
    c. Dialyze for 2 hours, change dialysis buffer, then let go overnight.
6) Quantitate protein concentration by BCA protein assay and snap freeze using ethanol and dry ice; store at -80C

Binding assay

1) Wash 60μl 30% Ni-NTA bead slurry with cold PBS, pH=7.4 and resuspend in 20μl to make 50% slurry
2) Rotate about 50μg of either GST-TRBPWT, GST-TRBPSΔD, or GST alone with 40μl 50% glutathione sepharose bead slurry, 2hrs-overnight at 4°C
3) Add about 25μg pure Lin28a protein to bead-bound GST-TRBPWT, GST-TRBPSΔD, or GST alone (approximately 2X TRBP per 1X Lin28a)
4) Rotate 2-4hrs, 4°C

5) Wash 3X with cold PBS, pH=7.4, by adding 1.5ml to each tube, inverting, centrifuging at 2000 x g for 30 sec, and suctioning off buffer
6) Add 60μl PBS with SDS loading buffer to each sample and boil for 8-10 min to elute. Analyze samples by immunoblot.

Note: use tube cap to prevent loss of volume while boiling

Epifluorescence Imaging:

Live cell fluorescence and FRET imaging were conducted on a Zeiss Axiovert 200M microscope controlled by Metafluor 6.2 software. Cells seeded on poly(L)lysine coated glass-bottom imaging dishes (MatTek Corporation) were incubated at 37 C in Hank's Balanced Salt Solution (HBSS), and imaged at 40x magnification with 50% neutral density filters, illuminated by an arc lamp and captured on a cooled charge coupled device (Photometrics). Fluorescence emission was collected from cyan fluorescent protein (420DF20 excitation filter, 500 ms excitation, 475DF40 emission filter); yellow fluorescent protein (420DF20 excitation for 50 ms, 535df25 emission filter); sensitized YFP emission (CFP excitation and YFP emission); and red fluorescent protein (568DF55 excitation filter, 50ms, 600DRLP dichroic mirror, 653DF95 emission filter).

For endpoint FRET imaging, cells expressing CFP-tagged TRBP or a truncation and YFP-tagged lin28a or a truncation were serum starved for approximately fifteen minutes in imaging media. Several images were taken to establish a baseline, followed by 90 second, 3 minute and 5 minute illumination

at 504 nm to bleach YFP. Images were quantified using MetaFluor 6.2 software (Universal Imaging). FRET efficiency was calculated based on the recovery in background-corrected CFP brightness after YFP bleaching, using the following formula:

$$FRET\ efficiency = 1-F_{da}/F_{d}$$

where F_{da} is the CFP fluorescence observed when both donor and acceptor are active, and F_{d},is the fluorescence observed after YFP photobleaching. To confirm complete photobleaching, percent change in YFP intensity was calculated, using the formula:

$$\%\ photobleaching = [(intensity\ final-intensity\ initial)/intensity\ initial] * 100\%$$

Only dishes with an average reduction of 80% or more in YFP signal were used for FRET efficiency calculation in epifluorescence experiments.

For time-course FRET imaging, cells expressing CFP-tagged TRBP-B with YFP-tagged Lin28a-3 were serum starved (0.5-2 hrs) in imaging media, then imaged every 30 s. CYFRET, CFP, YFP and RFP intensity in each ROI were measured over time using MetaFluor software and, after background subtraction, used to calculate the normalized FRET emission ratio, a measure that adjusts for expression level and spectral bleedthrough of donor and acceptor fluorophores (Xia & Liu, 2001).

$$NFRET = FRET\ intensity – [YFP\ intensity\ x\ a] – [CFP\ intensity\ x\ b]$$

$$NFRET\ ratio = NFRET/CFP$$

Bleedthrough value “a” was determined using cells expressing only YFP, then imaged in both the CYFRET and YFP channels. “A” was defined as the

signal in the YFRET channel as a percent of YFP signal; on this system, the value used was 0.14. Bleedthrough value “b” was calculated using the same approach with CFP alone, and came to 0.32. Representative images shown in figure 5E have had NFRET value calculated using the Image Calculator function in ImageJ to perform the same series of calculations (i.e., mean background subtraction in each channel, followed by subtraction of estimated bleedthrough from CFP and YFP direct channels, applied to CYFRET channel).

Confocal imaging

Live neuron FRET imaging was conducted on a Zeiss LSM 780 microscope at 63x magnification using an oil immersion objective, with NA of 1.4. Hippocampal neuronal cultures expressing the indicated fluorescent construct were allowed to equilibrate in Tyrode’s buffer and then imaged at 37 C after 24 to 30 hours of transfection (14 days in vitro). Where indicated, BDNF was added to 100 ng/mL in imaging media, either for thirty minutes prior to imaging (figure 2.6B) or after baseline imaging (figure 2.6C).

DsRed channel was excited with 2.0% laser intensity (DPSS 561), with wavelengths from 570-668 nm collected through a 58 nm pinhole to a gallium arsenide phosphide (GaAsP) detector. Gain settings were optimized for contrast of transfected cells against background. CFP/CYFRET channel was excited with 1.2% argon laser intensity at 458 nm, and collected through a 40.4 um pinhole with wavelengths 463-508 nm (CFP emission) sent to the GaAsP detector, and wavelengths 520-605 nm (sensitized YFP emission) collected in a photomultiplier

tube. YFP direct emission channel was excited using 0.6% argon laser intensity at 514 nm, collected once again through a 40.4 nm pinhole to the GaAsP detector, with wavelengths 520 to 615 nm. 109.4x109.4 um images (pixel size = 0.11 um square) were collected at scan speed 5, a dwell time of 6.3 usec per pixel.

Photobleaching was carried out on the confocal microscope using the 514 nm laser at 50% intensity at scan speed 4, a dwell time of 12.6 usec per pixel. Full Z-stacks were scanned three times with this paradigm, after which a bleached image was collected using the settings described above.

Epifluorescence Image analysis

When possible, image analysis was carried out using Metafluor imaging software. Regions of interest were selected by hand, and a screenshot was saved for future reference. When imaging region shifted in the XY plane, all regions of interest were shifted accordingly.

When Metafluor was unavailable, Metafluor output images were opened in Fiji (ImageJ) using the Bioformats Importer plugin. One stack was generated from each channel. To control for minor XY shifts, all stacks were registered with the StackReg plugin (using the ImageJ “StackReg” plugin, July 2011 distribution (Thevenez et al., 1998)) using the “rigid body transformation” setting. Regions of interest were selected in one channel and reproduced in other channels using the ROI Manager tool. Within each image, a background region of interest was chosen for baseline subtraction.

NFRET calculation

When reanalyzing Metafluor .log files to generate NFRET data shown in figure 2.5, a macro was written in Excel Visual Basic (VBA) to extract logged data. Code is reproduced in the Code Appendix, Macro 2.

Confocal image analysis

Neuron imaging datasets, saved as .czi files at “baseline” and “bleached” timepoints using Zen software (Zeiss, Oberkochen, Germany) were initially analyzed in three dimensions. Using Imaris image analysis software (Bitplane/Oxford Instruments, version 7.7.2), neuron images were masked with mCherry for processing. Threshold varied according to transfection efficiency. Regions of interest were selected in 3 dimensions to delineate dendritic shaft and spine; mean pre- and post-bleaching values per um^3 in YFP and CFP intensity within each region were used to calculate % YFP bleaching and FRET efficiency using the formulas described above. However, negative control cells expressing only CFP, which should show no FRET, tended to yield artificially high and extremely noisy apparent FRET efficiency values using this analysis strategy. The noise observed in apparent FRET efficiency in Imaris may have stemmed from a high degree of noise in CFP collection and a failure to replicate three-dimensional regions of interest accurately across timepoints. The reason for the positive average was not determined. However, analyzing a maximum intensity projection (MIP) of cells expressing CFP alone showed an appropriate average

FRET efficiency about zero. Therefore, images were condensed in ImageJ, using a custom ImageJ macro, which extracts pre- and post-bleach maximum intensity projections in each channel from .czi files composed of four channels (CFP, CYFRET, YFP, RFP). Code is reproduced (with comments) in the Coding appendix.

After construction and registration (using the ImageJ "StackReg" plugin) of maximum intensity projection images, an average of five dendritic regions of interest per neuron were generated and average intensity was measured at pre- and post-bleach timepoints in all channels. These values were used to calculate % YFP bleach and FRET efficiency as decribed above.

Statistical analyses

All quantified data represent mean +/- SEM. Statistical analysis included one-way ANOVA for independent samples with a Bonferroni *post hoc* test, $\alpha = 0.05$, comparing to Lin28a alone or comparable condition. Where noted, two-tailed student's *t* tests were used for pairwise comparison of untreated and treated conditions. Linear regression analysis and slope significance testing were carried out using a Graphpad Prism protocol equivalent to ANCOVA. Before linear regression was performed, independent variables were subjected to a Grubb's test with $\alpha = 0.05$. The result was used to justify removing one statistically significant outlier from TRBP-full regression analysis (Figure 2.1H).

Appendix 2: Image analysis macros

Macro 1: Generate multi-channel, multi-timepoint maximum intensity projections from XYZC .czi images (ImageJ)

When run using Fiji/ImageJ (Schindelin et al., *Nature Methods* 2012) this macro will open a pair of XYZC image stacks with the file names “baseline.czi” and “bleached.czi” saved in a user-defined directory (i.e., a folder) according to date and dish number. The macro will make a maximum intensity projection of each channel (up to 4 channels) from each image; concatenate the resulting single-frame MIPs, ordered as “channel1-baseline”, “channel1-bleached”, “channel2-baseline,” etc. The user is then presented with an opportunity to select regions of interest, which are measured in all channels; measurement outputs and ROI coordinates can be saved in user-defined files.

```
++++++

macro "define baseline & bleached" {

var path = getDirectory("Choose a directory") // user chooses a
directory for imaging date/dish/etc. from file storage location

var baseline = "baseline.czi" ;
var bleached = "bleached.czi" ;
print(path+baseline); //confirms location and name of files to be
condensed

// var datedish = file.directory.substring(path.lastIndexOf('/') + 1);
//non-operational code, tries to extract part of the file path that
gives date & dish information.

run("Bio-Formats Importer", "open=["+path+baseline+"] autoscale
color_mode=Composite concatenate_series display_metadata display_ome-
xml rois_import=[ROI manager] split_channels view=Hyperstack
stack_order=XYCZT"); //opens baseline.czi, as stacks separated by
fluorescence  channel
```

```
run("Bio-Formats Importer", "open=["+path+bleached+"] autoscale
color_mode=Composite concatenate_series display_metadata display_ome-
xml rois_import=[ROI manager] split_channels view=Hyperstack
stack_order=XYCZT"); // opens bleached.czi, as stacks separated by
fluorescence channel

// make MIPs of baseline images
for( i=0; i<4; i++ ) { // sets up a loop for 4-channel images
      selectWindow("baseline.czi - C=" + i); //chooses baseline stack
in channel (1:4)
      run("Z Project...", "projection=[Max Intensity]"); //makes MIP of
channel
      selectWindow("baseline.czi - C=" + i);
      close(); //closes source images, leaving MIP for each channel
open
}

// now do (bleached)

for( i=0; i<4; i++ ) {
      selectWindow("bleached.czi - C=" + i);
      run("Z Project...", "projection=[Max Intensity]");
      selectWindow("bleached.czi - C=" + i);
      close();
}

// concatenate a series of maximum intensity projections
var MIP = "MIP"
var array = split(path, "/") //splits file path by folder (e.g.,
"~/Documents/Imaging/Date/Dish" becomes a vector including "Documents",
"Imaging", "Date", "Dish"

var datedish = array[array.length-2]+"-"+array[array.length-1]
//expresses a unique file path for new MIP image

run("Concatenate...", "title=["+datedish+MIP+"]
image1=[MAX_baseline.czi - C=0] image2=[MAX_bleached.czi - C=0]
image3=[MAX_baseline.czi - C=2] image4=[MAX_bleached.czi - C=2]
image5=[MAX_baseline.czi - C=3] image6=[MAX_bleached.czi - C=3]
image7=[-- None --]");  // concatenates together MIPs pre and post
bleaching in CFP, YFP and RFP channels


saveAs("Tiff", ["/Desktop/Thesis/Imaging/MIPS/"+concat+MIP])
//write file: .tif of stack, i.e. "datedish

}

macro "measure all three with the same ROIs"
// open file : .tif of stack
//open ROI manager tool
roiManager("reset") //deletes ROIs from previous setup
//PAUSE FOR USER INPUT: ROIs of interest
roiManager("multi measure") //multi-measure ROIs in each, save output
roiManager("save,) //save ROIs- **user must input a file-path here! **
//close all files
```

+++++

Macro 2: Calculate NFRET from CYFRET/CFP/YFP/RFP measurements saved in Metafluor output .LOG files (Excel)

This macro was developed using the Excel visual basic editor to calculate NFRET (bleedthrough-corrected FRET value) from comma-separated .LOG datasets exported from Metafluor, with the following layout, which varied according to number of ROIs, with “R” indicating region number and “W” indicating wavelength.

Filename: (~/path/filename)								
Date								
Region 1: (coordinates)								
Region 2: (coordinates)								
…								
Region n: (coordinates)								
Time(sec)	R1 W1 AVG	R1 W2 Avg	R1 W3 avg	R1 W4 avg	R1 W1/W2 ratio	R2 W1 avg	R2 W2 avg	Etc…
001	##	##	##	##	##	##	##	
002	##	##	##	##	##	##	##	

The data layout varied according to number of regions specified in Metafluor (with the last defined ROI always chosen to cover a background region) and the number of timepoints collected. Therefore, the macro includes commands to count both regions of interest and timepoints, and subtract the background intensity in each channel from each region of interest for all timepoints. For NFRET calculation, the CFP bleedthrough correction varied according to the

CFP variant expressed (ECFP, Cerulean, or Cerulean3). Therefore, the macro assumes user input of an experimentally measured CFP bleedthrough correction value (that is, the CYFRET/CFP intensity ratio in an image of cells expressing only CFP) at cell A3.

```
++++
Sub calculateNfret()
    'define variables
    regions = Sheet1.Range("A:A").Find("Time (sec)").Row - 3
    timepoints = Sheet1.Range("A:A").Find(blankcell).Row - regions - 3
    cfpcorr = Cells(1, 3)
    substart = timepoints + regions * 2

    'calculate NFRET
    For j = 1 To timepoints
    For i = 1 To ((regions - 1) * 5) Step 5
        If (IsNumeric(Cells(substart + j, i + 1))) Then
        Cells(substart + regions + timepoints + j, i + 1) =
Round((Cells(substart + j, i + 1) - (cfpcorr * Cells(substart + j, i +
2)) - (0.1 * Cells(substart + j, i + 3))), 3)

        End If
    Next i
    Next j

     'calculate NFRET/CFP
    For j = 1 To timepoints
    For i = 1 To ((regions - 1) * 5) Step 5
        If (IsNumeric(Cells(substart + regions + timepoints + j, i +
1)) And (Cells(substart + regions + timepoints + j, i + 1)) <> 0) Then
        Cells(substart + regions + timepoints + j, i + 2) =
Round((Cells(substart + regions + timepoints + j, i + 1) /
Cells(substart + j, i + 2)), 6)
        End If
   Next i
   Next j
End Sub
++++
```

References

Chapter 1. Introduction

1. Aakalu G, Smith W, Nguyen N, Jiang C, Schuman E. Dynamic visualization of local protein synthesis in hippocampal neurons. *Neuron*. 2001;30(2):489-502.

2. Aksoy-Aksel A, Zampa F, Schratt G. MicroRNAs and synaptic plasticity-a mutual relationship. *Philosophical Transactions of the Royal Society B-Biological Sciences*. 2014;369(1652):20130515.

3. Ali PSS, Ghoshdastider U, Hoffmann J, Brutschy B, Filipek S. Recognition of the let-7g miRNA precursor by human Lin28B. *FEBS Lett*. 2012;586(22):3986-3990.

4. Alonso M, Medina J, Pozzo-Miller L. ERK1/2 activation is necessary for BDNF to increase dendritic spine density in hippocampal CA1 pyramidal neurons. *Learn Mem*. 2004;11(2):172-178.

5. Amen AM, Ruiz-Garzon CR, Shi J, Subramanian M, Pham DL, Meffert MK. A rapid induction mechanism for Lin28a in trophic responses. *Mol Cell*. 2017;65(3):490-+.

6. Baek D, Villen J, Shin C, Camargo FD, Gygi SP, Bartel DP. The impact of microRNAs on protein output. *Nature*. 2008;455(7209):64-U38.

7. Balzer E, Heine C, Jiang Q, Lee VM, Moss EG. LIN28 alters cell fate succession and acts independently of the let-7 microRNA during neurogliogenesis in vitro. *Development*. 2010;137(6):891-900.

8. Balzer E, Moss EG. Localization of the developmental timing regulator Lin28 to mRNP complexes, P-bodies and stress granules. *Rna Biology*. 2007;4(1):16-25.

9. Barca-Mayo O, Lu QR. Fine-tuning oligodendrocyte development by microRNAs. *Frontiers in Neuroscience*. 2012;6:UNSP 13.

10. Bicker S, Lackinger M, Weiss K, Schratt G. MicroRNA-132,-134, and -138: A microRNA troika rules in neuronal dendrites. *Cellular and Molecular Life Sciences*. 2014;71(20):3987-4005.

11. Bienvenut WV, Sumpton D, Martinez A, et al. Comparative large scale characterization of plant versus mammal proteins reveals similar and idiosyncratic N-alpha-acetylation features. *Molecular & Cellular Proteomics*. 2012;11(6):M111.015131.

12. Bluethgen N, van Bentum M, Merz B, Kuhl D, Hermey G. Profiling the MAPK/ERK dependent and independent activity regulated transcriptional programs in the murine hippocampus in vivo. *Scientific Reports*. 2017;7:45101.

13. Bogoyevitch MA, Kobe B. Uses for JNK: The many and varied substrates of the c-jun N-terminal kinases. *Microbiology and Molecular Biology Reviews*. 2006;70(4):1061-+.

14. Bradshaw K, Emptage N, Bliss T. A role for dendritic protein synthesis in hippocampal late LTP. *Eur J Neurosci*. 2003;18(11):3150-3152.

15. Bramham CR, Alme MN, Bittins M, et al. The arc of synaptic memory. *Experimental Brain Research*. 2010;200(2):125-140.

16. Bramham CR, Jensen KB, Proud CG. Tuning specific translation in cancer metastasis and synaptic memory: Control at the MNK-eIF4E axis. *Trends Biochem Sci*. 2016;41(10):847-858.

17. Briz V, Zhu G, Wang Y, et al. Activity-dependent rapid local RhoA synthesis is required for hippocampal synaptic plasticity. *Journal of Neuroscience*. 2015;35(5):2269-2282.

18. Caldeira MV, Melo CV, Pereira DB, Carvalho RF, Carvalho AL, Duarte CB. BDNF regulates the expression and traffic of NMDA receptors in cultured hippocampal neurons. *Mol Cell Neurosci*. 2007;35(2):208-219.

19. Canagarajah B, Khokhlatchev A, Cobb M, Goldsmith E. Activation mechanism of the MAP kinase ERK2 by dual phosphorylation. *Cell*. 1997;90(5):859-869.

20. Canal F, Palygin O, Pankratov Y, Correa SAL, Mueller J. Compartmentalization of the MAPK scaffold protein KSR1 modulates synaptic plasticity in hippocampal neurons. *FASEB J*. 2011;25(7):2362-2372.

21. Carvalho AL, Caldeira MV, Santos SD, Duarte CB. Role of the brain-derived neurotrophic factor at glutamatergic synapses. *Br J Pharmacol*. 2008;153:S310-S324.

22. Chai S, Cambronne XA, Eichhorn SW, Goodman RH. MicroRNA-134 activity in somatostatin interneurons regulates H-ras localization by repressing the palmitoylation enzyme, DHHC9. *Proc Natl Acad Sci U S A*. 2013;110(44):17898-17903.

23. Chang H, Triboulet R, Thornton JE, Gregory RI. A role for the perlman syndrome exonuclease Dis3l2 in the Lin28-let-7 pathway. *Nature*. 2013;497(7448):244-+.

24. Chao M. Neurotrophins and their receptors: A convergence point for many signalling pathways. *Nat Rev Neurosci*. 2003;4(4):299-309.

25. Chen C, Zhu C, Huang J, et al. SUMOylation of TARBP2 regulates miRNA/siRNA efficiency. *Nature Communications*. 2015;6:8899.

26. Cho J, Chang H, Kwon SC, et al. LIN28A is a suppressor of ER-associated translation in embryonic stem cells. *Cell*. 2012;151(4):765-777.

27. Cho J, Chang H, Kwon SC, et al. LIN28A is a suppressor of ER-associated translation in embryonic stem cells. *Cell*. 2012;151(4):765-777.

28. Cimadamore F, Amador-Arjona A, Chen C, Huang C, Terskikh AV. SOX2-LIN28/let-7 pathway regulates proliferation and neurogenesis in neural precursors. *Proc Natl Acad Sci U S A*. 2013;110(32):E3017-E3026.

29. Cohen MS, Orth CB, Kim HJ, Jeon NL, Jaffrey SR. Neurotrophin-mediated dendrite-to-nucleus signaling revealed by microfluidic compartmentalization of dendrites. *Proc Natl Acad Sci U S A*. 2011;108(27):11246-11251.

30. Cohen-Cory S. BDNF modulates, but does not mediate, activity-dependent branching and remodeling of optic axon arbors in vivo. *J Neurosci*. 1999;19(22):9996-10003.

31. Correa SAL, Hunter CJ, Palygin O, et al. MSK1 regulates homeostatic and experience-dependent synaptic plasticity. *Journal of Neuroscience*. 2012;32(38):13039-13051.

32. Daher A, Laraki G, Singh M, et al. TRBP control of PACT-induced phosphorylation of protein kinase R is reversed by stress. *Mol Cell Biol*. 2009;29(1):254-265.

33. Daniels SM, Gatignol A. The multiple functions of TRBP, at the hub of cell responses to viruses, stress, and cancer. *Microbiology and Molecular Biology Reviews*. 2012;76(3):652-+.

34. Davis S, Vanhoutte P, Pages C, Caboche J, Laroche S. The MAPK/ERK cascade targets both elk-1 and cAMP response element-binding protein to control long-term potentiation-dependent gene expression in the dentate gyrus in vivo. *J Neurosci*. 2000;20(12):4563-4572.

35. Desjardins A, Bouvette J, Legault P. Stepwise assembly of multiple Lin28 proteins on the terminal loop of let-7 miRNA precursors. *Nucleic Acids Res*. 2014;42(7):4615-4628.

36. Dhanasekaran DN, Johnson GL. MAPKs: Function, regulation, role in cancer and therapeutic targeting. *Oncogene*. 2007;26(22):3097-3099.

37. Duman RS, Voleti B. Signaling pathways underlying the pathophysiology and treatment of depression: Novel mechanisms for rapid-acting agents. *Trends Neurosci*. 2012;35(1):47-56.

38. English J, Sweatt J. Activation of p42 mitogen-activated protein kinase in hippocampal long term potentiation. *J Biol Chem*. 1996;271(40):24329-24332.

39. Frost RJA, Olson EN. Control of glucose homeostasis and insulin sensitivity by the let-7 family of microRNAs. *Proc Natl Acad Sci U S A*. 2011;108(52):21075-21080.

40. Gao J, Wang W, Mao Y, et al. A novel pathway regulates memory and plasticity via SIRT1 and miR-134. *Nature*. 2010;466(7310):1105-U120.

41. Gonzalez F, Raden D, Davis R. Identification of substrate recognition determinants for human Erk1 and Erk2 protein kinases. *Journal of Biological Chemistry*. 1991;266(33):22159.

42. Groth R, Mermelstein P. Brain-derived neurotrophic factor activation of NFAT (nuclear factor of activated T-cells)-dependent transcription: A role for the transcription factor NFATc4 in neurotrophin-mediated gene expression. *Journal of Neuroscience*. 2003;23(22):8125-8134.

43. Ha M, Kim VN. Regulation of microRNA biogenesis. *Nature Reviews Molecular Cell Biology*. 2014;15(8):509-524.

44. Hafner M, Max KEA, Bandaru P, et al. Identification of mRNAs bound and regulated by human LIN28 proteins and molecular requirements for RNA recognition. *Rna-a Publication of the Rna Society*. 2013;19(5):613-626.

45. Hagan JP, Piskounova E, Gregory RI. Lin28 recruits the TUTase Zcchc11 to inhibit let-7 maturation in mouse embryonic stem cells. *Nature Structural & Molecular Biology*. 2009;16(10):1021-U33.

46. Hanna J, Saha K, Pando B, et al. Direct cell reprogramming is a stochastic process amenable to acceleration. *Nature*. 2009;462(7273):595-U63.

47. Harvey CD, Yasuda R, Zhong H, Svoboda K. The spread of ras activity triggered by activation of a single dendritic spine. *Science*. 2008;321(5885):136-140.

48. Harward SC, Hedrick NG, Hall CE, et al. Autocrine BDNF-TrkB signalling within a single dendritic spine. *Nature*. 2016;538(7623):99-+.

49. Hedrick NG, Harward SC, Hall CE, Murakoshi H, McNamara JO, Yasuda R. Rho GTPase complementation underlies BDNF-dependent homo- and heterosynaptic plasticity. *Nature*. 2016;538(7623):104-+.

50. Heo I, Ha M, Lim J, et al. Mono-uridylation of pre-MicroRNA as a key step in the biogenesis of group II let-7 MicroRNAs. *Cell*. 2012;151(3):521-532.

51. Heo I, Joo C, Cho J, Ha M, Han J, Kim VN. Lin28 mediates the terminal uridylation of let-7 precursor MicroRNA. *Mol Cell*. 2008;32(2):276-284.

52. Heo I, Joo C, Kim Y, et al. TUT4 in concert with Lin28 suppresses MicroRNA biogenesis through pre-MicroRNA uridylation. *Cell*. 2009;138(4):696-708.

53. Herbert KM, Pimienta G, DeGregorio SJ, Alexandrov A, Steitz JA. Phosphorylation of DGCR8 increases its intracellular stability and induces a progrowth miRNA profile. *Cell Reports*. 2013;5(4):1070-1081.

54. Horch H, Katz L. BDNF release from single cells elicits local dendritic growth in nearby neurons. *Nat Neurosci*. 2002;5(11):1177-1184.

55. Huang YA, Ruiz CR, Eyler ECH, Lin K, Meffert MK. Dual regulation of miRNA biogenesis generates target specificity in neurotrophin-induced protein synthesis. *Cell*. 2012;148(5):933-946.

56. Huang Y, Kandel E. Theta frequency stimulation induces a local form of late phase LTP in the CA1 region of the hippocampus. *Learning & Memory*. 2005;12(6):587-593.

57. Jacobs D, Glossip D, Xing H, Muslin A, Kornfeld K. Multiple docking sites on substrate proteins form a modular system that mediates recognition by ERK MAP kinase. *Genes & Development*. 1999;13(2):163-175.

58. Jaitner C, Reddy C, Abentung A, et al. Satb2 determines miRNA expression and long-term memory in the adult central nervous system. *Elife*. 2016;5:e17361.

59. Jiang S, Baltimore D. RNA-binding protein Lin28 in cancer and immunity. *Cancer Lett*. 2016;375(1):108-113.

60. Jin J, Jing W, Lei X, et al. Evidence that Lin28 stimulates translation by recruiting RNA helicase A to polysomes. *Nucleic Acids Res*. 2011;39(9):3724-3734.

61. Juhila J, Sipila T, Icay K, et al. MicroRNA expression profiling reveals MiRNA families regulating specific biological pathways in mouse frontal cortex and hippocampus. *Plos One*. 2011;6(6):e21495.

62. Kandel E. Neuroscience - the molecular biology of memory storage: A dialogue between genes and synapses. *Science*. 2001;294(5544):1030-1038.

63. Kang H, Schuman E. A requirement for local protein synthesis in neurotrophin-induced hippocampal synaptic plasticity. *Science*. 1996;273(5280):1402-1406.

64. Kawashima H, Numakawa T, Kumamaru E, et al. Glucocorticoid attenuates brain-derived neurotrophic factor-dependent upregulation of glutamate receptors via the suppression of microrna-132 expression. *Neuroscience*. 2010;165(4):1301-1311.

65. Kennedy M. Signal-processing machines at the postsynaptic density. *Science*. 2000;290(5492):750-754.

66. Kim JD, Toda C, Ramirez CM, Fernandez-Hernando C, Diano S. Hypothalamic ventromedial Lin28a enhances glucose metabolism in diet-induced obesity. *Diabetes*. 2017;66(8):2102-2111.

67. Kim Y, Yeo J, Lee JH, et al. Deletion of human tarbp2 reveals cellular microRNA targets and cell-cycle function of TRBP. *Cell Rep*. 2014;9(3):1061-1074.

68. Kim Y, Yeo J, Lee JH, et al. Deletion of human tarbp2 reveals cellular MicroRNA targets and cell-cycle function of TRBP. *Cell Reports*. 2014;9(3):1061-1074.

69. Konopka W, Kiryk A, Novak M, et al. MicroRNA loss enhances learning and memory in mice. *Journal of Neuroscience*. 2010;30(44):14835-14842.

70. Kye M, Liu T, Levy SF, et al. Somatodendritic microRNAs identified by laser capture and multiplex RT-PCR. *Rna-a Publication of the Rna Society*. 2007;13(8):1224-1234.

71. Lee SR, Escobedo-Lozoya Y, Szatmari EM, Yasuda R. Activation of CaMKII in single dendritic spines during long-term potentiation. *Nature*. 2009;458(7236):299-U58.

72. Lei X, Xu J, Ma W, et al. Determinants of mRNA recognition and translation regulation by Lin28. *Nucleic Acids Res*. 2012;40(8):3574-3584.

73. Li Q, Zhang X, Hu W, et al. Importin-7 mediates memory consolidation through regulation of nuclear translocation of training-activated MAPK in drosophila. *Proc Natl Acad Sci U S A*. 2016;113(11):3072-3077.

74. Liao L, Pilotte J, Xu T, et al. BDNF induces widespread changes in synaptic protein content and up-regulates components of the translation machinery: An analysis using high-throughput proteomics. *J Proteome Res*. 2007;6(3):1059-1071.

75. Linnarsson S, Bjorklund A, Ernfors P. Learning deficit in BDNF mutant mice. *Eur J Neurosci*. 1997;9(12):2581-2587.

76. Liu X, Chen M, Li L, Gong L, Zhou H, Gao D. Extracellular signal-regulated kinases (ERKs) phosphorylate Lin28a protein to modulate P19 cell proliferation and differentiation. *Journal of Biological Chemistry*. 2017;292(10):3970-3976.

77. Liu X, Chen M, Li L, Gong L, Zhou H, Gao D. Extracellular signal-regulated kinases (ERKs) phosphorylate Lin28a protein to modulate P19 cell proliferation and differentiation. *J Biol Chem*. 2017;292(10):3970-3976.

78. Loughlin FE, Gebert LFR, Towbin H, Brunschweiger A, Hall J, Allain FH. Structural basis of pre-let-7 miRNA recognition by the zinc knuckles of pluripotency factor Lin28. *Nature Structural & Molecular Biology*. 2012;19(1):84-U105.

79. Mao L, Yang L, Tang Q, Samdani S, Zhang G, Wang J. The scaffold protein homer1b/c links metabotropic glutamate receptor 5 to extracellular signal-regulated protein kinase cascades in neurons. *Journal of Neuroscience*. 2005;25(10):2741-2752.

80. Mattson M, Meffert M. Roles for NF-kappa B in nerve cell survival, plasticity, and disease. *Cell Death Differ*. 2006;13(5):852-860.

81. Mayr F, Schuetz A, Doege N, Heinemann U. The Lin28 cold-shock domain remodels pre-let-7 microRNA. *Nucleic Acids Res*. 2012;40(15):7492-7506.

82. McNeill E, Van Vactor D. MicroRNAs shape the neuronal landscape. *Neuron*. 2012;75(3):363-379.

83. Mehta S, Zhang J. Reporting from the field: Genetically encoded fluorescent reporters uncover signaling dynamics in living biological systems. *Annu Rev Biochem*. 2011;80:375-+.

84. Mendoza MC, Er EE, Blenis J. The ras-ERK and PI3K-mTOR pathways: Cross-talk and compensation. *Trends Biochem Sci*. 2011;36(6):320-328.

85. Messaoudi E, Kanhema T, Soule J, et al. Sustained Arc/Arg3.1 synthesis controls long-term potentiation consolidation through regulation of local actin polymerization in the dentate gyrus in vivo. *Journal of Neuroscience*. 2007;27(39):10445-10455.

86. Montalbano A, Baj G, Papadia D, Tongiorgi E, Sciancalepore M. Blockade of BDNF signaling turns chemically-induced long-term potentiation into long-term depression. *Hippocampus*. 2013;23(10):879-889.

87. Nakamura T, Kunz RC, Zhang C, et al. A critical role for PKR complexes with TRBP in immunometabolic regulation and eIF2 alpha phosphorylation in obesity. *Cell Reports*. 2015;11(2):295-307.

88. Nam Y, Chen C, Gregory RI, Chou JJ, Sliz P. Molecular basis for interaction of let-7 MicroRNAs with Lin28. *Cell*. 2011;147(5):1080-1091.

89. Newman MA, Thomson JM, Hammond SM. Lin-28 interaction with the let-7 precursor loop mediates regulated microRNA processing. *RNA*. 2008;14(8):1539-1549.

90. Nowak JS, Hobor F, Velasco ADR, et al. Lin28a uses distinct mechanisms of binding to RNA and affects miRNA levels positively and negatively. *RNA*. 2017;23(3):317-332.

91. Panja D, Kenney JW, D'Andrea L, et al. Two-stage translational control of dentate gyrus LTP consolidation is mediated by sustained BDNF-TrkB signaling to MNK. *Cell Reports*. 2014;9(4):1430-1445.

92. Paroo Z, Ye X, Chen S, Liu Q. Phosphorylation of the human microRNA-generating complex mediates MAPK/Erk signaling. *Cell*. 2009;139(1):112-122.

93. Patterson S, Abel T, Deuel T, MArtin K, Rose J, Kandel E. Recombinant BDNF rescues deficits in basal synaptic transmission and hippocampal LTP in BDNF knockout mice. *Neuron*. 1996;16(6):1137-1145.

94. Patterson S, Pittenger C, Morozov A, et al. Some forms of cAMP-mediated long-lasting potentiation are associated with release of BDNF and nuclear translocation of phospho-MAP kinase. *Neuron*. 2001;32(1):123-140.

95. Peng S, Chen L, Lei X, et al. Genome-wide studies reveal that Lin28 enhances the translation of genes important for growth and survival of human embryonic stem cells. *Stem Cells*. 2011;29(3):496-504.

96. Perez LM, Bernal A, San Martin N, Lorenzo M, Fernandez-Veledo S, Galvez BG. Metabolic rescue of obese adipose-derived stem cells by Lin28/Let7 pathway. *Diabetes*. 2013;62(7):2368-2379.

97. Piskounova E, Polytarchou C, Thornton JE, et al. Lin28A and Lin28B inhibit let-7 MicroRNA biogenesis by distinct mechanisms. *Cell*. 2011;147(5):1066-1079.

98. Piskounova E, Viswanathan SR, Janas M, et al. Determinants of microRNA processing inhibition by the developmentally regulated RNA-binding protein Lin28. *J Biol Chem*. 2008;283(31):21310-21314.

99. Pizzorusso T, Ratto G, Putignano E, Maffei L. Brain-derived neurotrophic factor causes cAMP response element-binding protein phosphorylation in absence of calcium increases in slices and cultured neurons from rat visual cortex. *J Neurosci*. 2000;20(8):2809-2816.

100. Polesskaya A, Cuvellier S, Naguibneva I, Duquet A, Moss EG, Harel-Bellan A. Lin-28 binds IGF-2 mRNA and participates in skeletal myogenesis by increasing translation efficiency. *Genes Dev*. 2007;21(9):1125-1138.

101. Rex CS, Lin C, Kramar EA, Chen LY, Gall CM, Lynch G. Brain-derived neurotrophic factor promotes long-term potentiation-related cytoskeletal changes in adult hippocampus. *J Neurosci*. 2007;27(11):3017-3029.

102. Rigbolt KTG, Prokhorova TA, Akimov V, et al. System-wide temporal characterization of the proteome and phosphoproteome of human embryonic stem cell differentiation. *Science Signaling*. 2011;4(164):rs3.

103. Roush S, Slack FJ. The let-7 family of microRNAs. *Trends Cell Biol*. 2008;18(10):505-516.

104. Rybak A, Fuchs H, Smirnova L, et al. A feedback loop comprising lin-28 and let-7 controls pre-let-7 maturation during neural stem-cell commitment. *Nat Cell Biol*. 2008;10(8):987-993.

105. Sambandan S, Akbalik G, Kochen L, et al. NEUROSCIENCE activity-dependent spatially localized miRNA maturation in neuronal dendrites. *Science*. 2017;355(6325):634-637.

106. Sanghvi VR, Steel LF. The cellular TAR RNA binding protein, TRBP, promotes HIV-1 replication primarily by inhibiting the activation of double-stranded RNA-dependent kinase PKR. *J Virol*. 2011;85(23):12614-12621.

107. Schratt G, Nigh E, Chen W, Hu L, Greenberg M. BDNF regulates the translation of a select group of mRNAs by a mammalian target of rapamycin-phosphatidylinositol 3-kinase-dependent pathway during neuronal development. *Journal of Neuroscience*. 2004;24(33):7366-7377.

108. Schratt G, Tuebing F, Nigh E, et al. A brain-specific microRNA regulates dendritic spine development. *Nature*. 2006;439(7074):283-289.

109. Selbach M, Schwanhaeusser B, Thierfelder N, Fang Z, Khanin R, Rajewsky N. Widespread changes in protein synthesis induced by microRNAs. *Nature*. 2008;455(7209):58-63.

110. Sempere L, Freemantle S, Pitha-Rowe I, Moss E, Dmitrovsky E, Ambros V. Expression profiling of mammalian microRNAs uncovers a subset of brain-expressed microRNAs with possible roles in murine and human neuronal differentiation. *Genome Biol*. 2004;5(3):R13.

111. Shelly M, Cancedda L, Lim BK, et al. Semaphorin3A regulates neuronal polarization by suppressing axon formation and promoting dendrite growth. *Neuron*. 2011;71(3):433-446.

112. Shelly M, Lim BK, Cancedda L, Heilshorn SC, Gao H, Poo M. Local and long-range reciprocal regulation of cAMP and cGMP in Axon/Dendrite formation. *Science*. 2010;327(5965):547-552.

113. Shinoda G, Shyh-Chang N, de Soysa TY, et al. Fetal deficiency of Lin28 programs life-long aberrations in growth and glucose metabolism. *Stem Cells*. 2013;31(8):1563-1573.

114. Shinohara Y, Yahagi K, Kawano M, et al. miRNA profiling of bilateral rat hippocampal CA3 by deep sequencing. *Biochem Biophys Res Commun*. 2011;409(2):293-298.

115. Shyh-Chang N, Daley GQ. Lin28: Primal regulator of growth and metabolism in stem cells. *Cell Stem Cell*. 2013;12(4):395-406.

116. Smart F, Edelman G, Vanderklish P. BDNF induces translocation of initiation factor 4E to mRNA granules: Evidence for a role of synaptic microfilaments and integrins. *Proc Natl Acad Sci U S A*. 2003;100(24):14403-14408.

117. Takei N, Kawamura M, Hara K, Yonezawa K, Nawa H. Brain-derived neurotrophic factor enhances neuronal translation by activating multiple initiation processes - comparison with the effects of insulin. *J Biol Chem*. 2001;276(46):42818-42825.

118. Tanabe K, Nakamura M, Narita M, Takahashi K, Yamanaka S. Maturation, not initiation, is the major roadblock during reprogramming toward pluripotency from human fibroblasts. *Proc Natl Acad Sci U S A*. 2013;110(30):12172-12179.

119. Tanaka J, Horiike Y, Matsuzaki M, Miyazaki T, Ellis-Davies GCR, Kasai H. Protein synthesis and neurotrophin-dependent structural plasticity of single dendritic spines. *Science*. 2008;319(5870):1683-1687.

120. Tang S, Yasuda R. Imaging ERK and PKA activation in single dendritic spines during structural plasticity. *Neuron*. 2017;93(6):1315-+.

121. Thomas G, Huganir R. Mapk cascade signalling and synaptic plasticity. *Nature Reviews Neuroscience*. 2004;5(3):173-183.

122. Thomson J, Parker J, Perou C, Hammond S. A custom microarray platform for analysis of microRNA gene expression. *Nature Methods*. 2004;1(1):47-53.

123. Thornton JE, Chang H, Piskounova E, Gregory RI. Lin28-mediated control of let-7 microRNA expression by alternative TUTases Zcchc11 (TUT4) and Zcchc6 (TUT7). *Rna-a Publication of the Rna Society*. 2012;18(10):1875-1885.

124. Towler BP, Jones CI, Viegas SC, et al. The 3 '-5 ' exoribonuclease Dis3 regulates the expression of specific microRNAs in drosophila wing imaginal discs. *Rna Biology*. 2015;12(7):728-741.

125. Tsanov KM, Pearson DS, Wu Z, et al. LIN28 phosphorylation by MAPK/ERK couples signalling to the post-transcriptional control of pluripotency. *Nat Cell Biol*. 2017;19(1):60-67.

126. Van Hoof D, Munoz J, Braam SR, et al. Phosphorylation dynamics during early differentiation of human embryonic stem cells. *Cell Stem Cell*. 2009;5(2):214-226.

127. Vo N, Klein M, Varlamova O, et al. A cAMP-response element binding protein-induced microRNA regulates neuronal morphogenesis. *Proc Natl Acad Sci U S A*. 2005;102(45):16426-16431.

128. Wainstein E, Seger R. The dynamic subcellular localization of ERK: Mechanisms of translocation and role in various organelles. *Curr Opin Cell Biol*. 2016;39:15-20.

129. Wang L, Nam Y, Lee AK, et al. LELIN28 zinc knuckle domain is required and sufficient to induce let-7 oligouridylation. *Cell Reports*. 2017;18(11):2664-2675.

130. Warner MJ, Bridge KS, Hewitson JP, et al. S6K2-mediated regulation of TRBP as a determinant of miRNA expression in human primary lymphatic endothelial cells. *Nucleic Acids Res*. 2016;44(20):9942-9955.

131. Wiegert JS, Bengtson CP, Bading H. Diffusion and not active transport underlies and limits ERK1/2 synapse-to-nucleus signaling in hippocampal neurons. *J Biol Chem*. 2007;282(40):29621-29633.

132. Wilbert ML, Huelga SC, Kapeli K, et al. LIN28 binds messenger RNAs at GGAGA motifs and regulates splicing factor abundance. *Mol Cell*. 2012;48(2):195-206.

133. Wilson RC, Tambe A, Kidwell MA, Noland CL, Schneider CP, Doudna JA. Dicer-TRBP complex formation ensures accurate mammalian MicroRNA biogenesis. *Mol Cell*. 2015;57(3):397-407.

134. Wulczyn FG, Smirnova L, Rybak A, et al. Post-transcriptional regulation of the let-7 microRNA during neural cell specification. *Faseb Journal*. 2007;21(2):415-426.

135. Xu B, Zhang K, Huang Y. Lin28 modulates cell growth and associates with a subset of cell cycle regulator mRNAs in mouse embryonic stem cells. *Rna-a Publication of the Rna Society*. 2009;15(3):357-361.

136. Yang M, Yang S, Herrlinger S, et al. Lin28 promotes the proliferative capacity of neural progenitor cells in brain development. *Development*. 2015;142(9):1616-1627.

137. Yang Y, Wang X, Frerking M, Zhou Q. Spine expansion and stabilization associated with long-term potentiation. *J Neurosci*. 2008;28(22):5740-5751.

138. Yao B, Christian KM, He C, Jin P, Ming G, Song H. Epigenetic mechanisms in neurogenesis. *Nature Reviews Neuroscience*. 2016;17(9):537-549.

139. Yasuda R, Murakoshi H. The mechanisms underlying the spatial spreading of signaling activity. *Curr Opin Neurobiol*. 2011;21(2):313-321.

140. Ying S, Futter M, Rosenblum K, et al. Brain-derived neurotrophic factor induces long-term potentiation in intact adult hippocampus: Requirement for ERK activation coupled to CREB and upregulation of arc synthesis. *Journal of Neuroscience*. 2002;22(5):1532-1540.

141. Yoshii A, Constantine-Paton M. Postsynaptic BDNF-TrkB signaling in synapse maturation, plasticity, and disease. *Dev Neurobiol*. 2010;70(5):304-322.

142. Yu J, Vodyanik MA, Smuga-Otto K, et al. Induced pluripotent stem cell lines derived from human somatic cells. *Science*. 2007;318(5858):1917-1920.

143. Zeng Y, Yao B, Shin J, et al. Lin28A binds active promoters and recruits Tet1 to regulate gene expression. *Mol Cell*. 2016;61(1):153-160.

144. Zhu H, Shah S, Shyh-Chang N, et al. Lin28a transgenic mice manifest size and puberty phenotypes identified in human genetic association studies. *Nat Genet*. 2010;42(7):626-U106.

145. Zhu H, Shyh-Chang N, Segre AV, et al. The Lin28/let-7 axis regulates glucose metabolism. *Cell*. 2011;147(1):81-94.

Chapter 2.

1. Amen AM, Ruiz-Garzon CR, Shi J, Subramanian M, Pham DL, Meffert MK. A rapid induction mechanism for Lin28a in trophic responses. *Mol Cell*. 2017;65(3):490-+.

2. Baek D, Villen J, Shin C, Camargo FD, Gygi SP, Bartel DP. The impact of microRNAs on protein output. *Nature*. 2008;455(7209):64-U38.

3. Chen C, Zhu C, Huang J, et al. SUMOylation of TARBP2 regulates miRNA/siRNA efficiency. *Nature Communications*. 2015;6:8899.

4. Cho J, Chang H, Kwon SC, et al. LIN28A is a suppressor of ER-associated translation in embryonic stem cells. *Cell*. 2012;151(4):765-777.

5. Daher A, Laraki G, Singh M, et al. TRBP control of PACT-induced phosphorylation of protein kinase R is reversed by stress. *Mol Cell Biol*. 2009;29(1):254-265.

6. Daher A, Longuet M, Dorin D, et al. Two dimerization domains in the trans-activation response RNA-binding protein (TRBP) individually reverse the protein kinase R inhibition of HIV-1 long terminal repeat expression. *J Biol Chem*. 2001;276(36):33899-33905.

7. Daniels SM, Melendez-Pena CE, Scarborough RJ, et al. Characterization of the TRBP domain required for dicer interaction and function in RNA interference. *BMC Mol Biol*. 2009;10:38-2199-10-38.

8. Ding Y, Li J, Enterina JR, et al. Ratiometric biosensors based on dimerization-dependent fluorescent protein exchange. *Nature Methods*. 2015;12(3):195-+.

9. Gonzalez F, Raden D, Davis R. Identification of substrate recognition determinants for human Erk1 and Erk2 protein kinases. *Journal of Biological Chemistry*. 1991;266(33):22159.

10. Huang YA, Ruiz CR, Eyler ECH, Lin K, Meffert MK. Dual regulation of miRNA biogenesis generates target specificity in neurotrophin-induced protein synthesis. *Cell*. 2012;148(5):933-946.

11. Jacobs D, Glossip D, Xing H, Muslin A, Kornfeld K. Multiple docking sites on substrate proteins form a modular system that mediates recognition by ERK MAP kinase. *Genes & Development*. 1999;13(2):163-175.

12. Jiang S, Baltimore D. RNA-binding protein Lin28 in cancer and immunity. *Cancer Lett*. 2016;375(1):108-113.

13. Kim Y, Yeo J, Lee JH, et al. Deletion of human tarbp2 reveals cellular microRNA targets and cell-cycle function of TRBP. *Cell Rep*. 2014;9(3):1061-1074.

14. Laraki G, Clerzius G, Daher A, Melendez-Pena C, Daniels S, Gatignol A. Interactions between the double-stranded RNA-binding proteins TRBP and PACT define the medipal domain that mediates protein-protein interactions. *Rna Biology*. 2008;5(2):92-103.

15. Liu X, Chen M, Li L, Gong L, Zhou H, Gao D. Extracellular signal-regulated kinases (ERKs) phosphorylate Lin28a protein to modulate P19 cell proliferation and differentiation. *Journal of Biological Chemistry*. 2017;292(10):3970-3976.

16. Llopis J, McCaffery M, Miyawaki A, Farquhart M, Tsien RY. Measurement of cytosolic, mitochondrial, and golgi pH in single living cells with green fluorescent proteins. *Proceedings of the National Academies of Science*. 1998;95(12):6803-6808.

17. Markwardt ML, Kremers G-J, Kraft CA, Ray K, Cranfill PJC, Wilson KA, et al. An improved cerulean fluorescent protein with enhanced brightness and reduced reversible photoswitching. *PLoS ONE*. 2011;6(3):e17896.

18. Mayr F, Schuetz A, Doege N, Heinemann U. The Lin28 cold-shock domain remodels pre-let-7 microRNA. *Nucleic Acids Res*. 2012;40(15):7492-7506.

19. Miyawaki A. Development of probes for cellular functions using fluorescent proteins and fluorescence resonance energy transfer. *Annual Review of Biochemistry*. 2011;80:357-373.

20. Nagai T, Ibata K, Park E, Kubota M, Mikoshiba K, Miyawaki A. A variant of yellow fluorescent protein with fast and efficient maturation for cell-biological applications.. *Nature Biotechnology*. 2002;20(1):87-90.

21. Nagai T, Yamada S, Tominaga T, Ichikawa M, Miyawaki A. Expanded dynamic range of fluorescent indicators for ca(2+) by circularly permuted yellow fluorescent **proteins.**. *Proceedings of the National Academies of Science*. 2004;101(29):10554-10559.

22. Nam Y, Chen C, Gregory RI, Chou JJ, Sliz P. Molecular basis for interaction of let-7 MicroRNAs with Lin28. *Cell*. 2011;147(5):1080-1091.

23. Paroo Z, Ye X, Chen S, Liu Q. Phosphorylation of the human microRNA-generating complex mediates MAPK/Erk signaling. *Cell*. 2009;139(1):112-122.

24. Rizzo M, Springer G, Granada B, Piston D. An improved cyan fluorescent protein variant useful for FRET. *Nat Biotechnol*. 2004;22(4):445-449.

25. Romoser V, Hinkle P, Persechini A. Detection in living cells of Ca2+-dependent changes in the fluorescence emission of an indicator composed of two green fluorescent protein variants linked by a calmodulin-binding sequence - A new class of fluorescent indicators. *J Biol Chem*. 1997;272(20):13270-13274.

26. Rybak, Fuchs, Smirnova, et al. A feedback loop comprising *lin*-28 and *let*-7 controls pre-*let*-7 maturation during neural stem-cell commitment. *Nature Cell Biology*. 2008;10:987-993.

27. Selbach M, Schwanhaeusser B, Thierfelder N, Fang Z, Khanin R, Rajewsky N. Widespread changes in protein synthesis induced by microRNAs. *Nature*. 2008;455(7209):58-63.

28. Shinoda G, Shyh-Chang N, de Soysa TY, et al. Fetal deficiency of Lin28 programs life-long aberrations in growth and glucose metabolism. *Stem Cells*. 2013;31(8):1563-1573.

29. Shyh-Chang N, Daley GQ. Lin28: Primal regulator of growth and metabolism in stem cells. *Cell Stem Cell*. 2013;12(4):395-406.

30. Shyh-Chang N, Zhu H, Yvanka de Soysa T, et al. Lin28 enhances tissue repair by reprogramming cellular metabolism. *Cell*. 2013;155(4):778-792.

31. Stalder L, Heusermann W, Sokol L, et al. The rough endoplasmic reticiulum is a central nucleation site of siRNA-mediated RNA silencing. *EMBO Journal*. 2013;32(8):1115-1127.

32. Tsanov KM, Pearson DS, Wu Z, et al. LIN28 phosphorylation by MAPK/ERK couples signalling to the post-transcriptional control of pluripotency. *Nat Cell Biol*. 2017;19(1):60-67.

33. Viswanathan, SR (Viswanathan, Srinivas R.)[1], Powers, JT (Powers, John T.)[1], Einhorn, W (Einhorn, William)[1], et al. Lin28 promotes transformation and is associated with advanced human malignancies. *Nature Genetics*. 2009;41(7):843.

34. Warner MJ, Bridge KS, Hewitson JP, et al. S6K2-mediated regulation of TRBP as a determinant of miRNA expression in human primary lymphatic endothelial cells. *Nucleic Acids Res*. 2016;44(20):9942-9955.

35. Wilson RC, Tambe A, Kidwell MA, Noland CL, Schneider CP, Doudna JA. Dicer-TRBP complex formation ensures accurate mammalian MicroRNA biogenesis. *Mol Cell*. 2015;57(3):397-407.

36. Xia Z, Liu Y. Reliable and global measurement of fluorescence resonance energy transfer using fluorescence microscopes. *Biophys J*. 2001;81(4):2395-2402.

37. Zhou X, Clister TL, Lowry PR, Seldin MM, Wong GW, Zhang J. Dynamic visualization of mTORC1 activity in living cells. *Cell Reports*. 2015;10(10):1767-1777.

38. Zhu H, Shyh-Chang N, Segre AV, et al. The Lin28/let-7 axis regulates glucose metabolism. *Cell*. 2011;147(1):81-94.

Chapter 3.

1. Adams SR, Harootunian AT, Buechler YJ, Taylor SS, Tsien RY. Fluorescence ratio imaging of cyclic-amp in single cells. *Nature*. 1991;349(6311):694-697.

2. Allen MD, Zhang J. Subcellular dynamics of protein kinase A activity visualized by FRET-based reporters. *Biochem Biophys Res Commun*. 2006;348(2):716-721.

3. Almabouada F, Diaz-Ruiz A, Rabanal-Ruiz Y, Peinado JR, Vazquez-Martinez R, Malagon MM. Adiponectin receptors form homomers and heteromers exhibiting distinct ligand binding and intracellular signaling properties. *J Biol Chem*. 2013;288(5):3112-3125.

4. Ananthanarayanan B, Fosbrink M, Rahdar M, Zhang J. Live-cell molecular analysis of akt activation reveals roles for activation loop phosphorylation. *J Biol Chem*. 2007;282(50):36634-36641.

5. ARENZANASEISDEDOS F, THOMPSON J, RODRIGUEZ M, BACHELERIE F, THOMAS D, HAY R. Inducible nuclear expression of newly synthesized I-kappa-B-alpha negatively regulates dna-binding and transcriptional activities of nf-kappa-B. *Mol Cell Biol*. 1995;15(5):2689-2696.

6. Audet M, Lagace M, Silversides DW, Bouvier M. Protein-protein interactions monitored in cells from transgenic mice using bioluminescence resonance energy transfer. *Faseb Journal*. 2010;24(8):2829-2838.

7. Baldi L, Brown K, Franzoso G, Siebenlist U. Critical role for lysines 21 and 22 in signal-induced, ubiquitin-mediated proteolysis of I kappa B-alpha. *J Biol Chem*. 1996;271(1):376-379.

8. BEG A, RUBEN S, SCHEINMAN R, HASKILL S, ROSEN C, BALDWIN A. I-kappa-B interacts with the nuclear-localization sequences of the subunits of nf-kappa-B - a mechanism for cytoplasmic retention. *Genes Dev*. 1992;6(10):1899-1913.

9. Behar M, Hoffmann A. Tunable signal processing through a kinase control cycle: The IKK signaling node. *Biophys J*. 2013;105(1):231-241.

10. Borroto-Escuela DO, Romero-Fernandez W, Mudo G, et al. Fibroblast growth factor receptor 1-5-hydroxytryptamine 1A heteroreceptor complexes and their enhancement of hippocampal plasticity. *Biol Psychiatry*. 2012;71(1):84-91.

11. Brun MA, Tan K, Griss R, Kielkowska A, Reymond L, Johnsson K. A semisynthetic fluorescent sensor protein for glutamate. *J Am Chem Soc*. 2012;134(18):7676-7678.

12. Calleja V, Ameer-Beg SM, Vojnovic B, Woscholski R, Downward J, Larijani B. Monitoring conformational changes of proteins in cells by fluorescence lifetime imaging microscopy. *Biochem J*. 2003;372:33-40.

13. CHEN Z, HAGLER J, PALOMBELLA V, et al. Signal-induced site-specific phosphorylation targets I-kappa-B-alpha to the ubiquitin-proteasome pathway. *Genes Dev*. 1995;9(13):1586-1597.

14. Chu Y, Yao PY, Wang W, et al. Aurora B kinase activation requires survivin priming phosphorylation by PLK1. *Journal of Molecular Cell Biology*. 2011;3(4):260-267.

15. Day RN, Davidson MW. Fluorescent proteins for FRET microscopy: Monitoring protein interactions in living cells. *Bioessays*. 2012;34(5):341-350.

16. Degtyar V, Hafez IM, Bray C, Zucker RS. Dance of the SNAREs: Assembly and rearrangements detected with FRET at neuronal synapses. *Journal of Neuroscience*. 2013;33(13):5507-5523.

17. Deplazes E, Jayatilaka D, Corry B. ExiFRET: Flexible tool for understanding FRET in complex geometries. *J Biomed Opt*. 2012;17(1):011005.

18. Depry C, Allen MD, Zhang J. Visualization of PKA activity in plasma membrane microdomains. *Molecular Biosystems*. 2011;7(1):52-58.

19. DiDonato J, Hayakawa M, Rothwarf D, Zandi E, Karin M. A cytokine-responsive I kappa B kinase that activates the transcription factor NF-kappa B. *Nature*. 1997;388(6642):548-554.

20. Eisler SA, Fuchs YF, Pfizenmaier K, Hausser A. G-PKDrep-live, a genetically encoded FRET reporter to measure PKD activity at the trans-golgi-network. *Biotechnology Journal*. 2012;7(1):148-154.

21. Evrard-Todeschi N, Pons J, Gharbi-Benarous J, Bertho G, Benarous R, Girault J. Structure of the complex between phosphorylated substrates and the SCF beta-TrCP ubiquitin ligase receptor: A combined NMR, molecular modeling, and docking approach. *Journal of Chemical Information and Modeling*. 2008;48(12):2350-2361.

22. Fortmann KT, Lewis RD, Ngo KA, Fagerlund R, Hoffmann A. A regulated, ubiquitin-independent degron in I kappa B alpha. *J Mol Biol*. 2015;427(17):2748-2756.

23. Fosbrink M, Aye-Han N, Cheong R, Levchenko A, Zhang J. Visualization of JNK activity dynamics with a genetically encoded fluorescent biosensor. *Proc Natl Acad Sci U S A*. 2010;107(12):5459-5464.

24. Fuchs YF, Eisler SA, Link G, et al. A golgi PKD activity reporter reveals a crucial role of PKD in nocodazole-induced golgi dispersal. *Traffic*. 2009;10(7):858-867.

25. Fujioka A, Terai K, Itoh RE, et al. Dynamics of the Ras/ERK MAPK cascade as monitored by fluorescent probes. *J Biol Chem*. 2006;281(13):8917-8926.

26. Gao X, Zhang J. Spatiotemporal analysis of differential akt regulation in plasma membrane microdomains. *Mol Biol Cell*. 2008;19(10):4366-4373.

27. Gautier A, Juillerat A, Heinis C, et al. An engineered protein tag for multiprotein labeling in living cells. *Chem Biol*. 2008;15(2):128-136.

28. Gavet O, Pines J. Activation of cyclin B1-Cdk1 synchronizes events in the nucleus and the cytoplasm at mitosis. *J Cell Biol*. 2010;189(2):247-259.

29. Geguchadze R, Zhi G, Lau KS, et al. Quantitative measurements of Ca2+/calmodulin binding and activation of myosin light chain kinase in cells. *FEBS Lett*. 2004;557(1-3):121-124.

30. Gervasi N, Tchenio P, Preat T. PKA dynamics in a drosophila learning center: Coincidence detection by rutabaga adenylyl cyclase and spatial regulation by dunce phosphodiesterase. *Neuron*. 2010;65(4):516-529.

31. Goto A, Sumiyama K, Kamioka Y, et al. GDNF and endothelin 3 regulate migration of enteric neural crest-derived cells via protein kinase A and Rac1. *Journal of Neuroscience*. 2013;33(11):4901-4912.

32. Hachet-Haas M, Converset N, Marchal O, et al. FRET and colocalization analyzer - A method to validate measurements of sensitized emission FRET acquired by confocal microscopy and available as an ImageJ plug-in. *Microsc Res Tech*. 2006;69(12):941-956.

33. Haecker, Hans & Karin, Michael. Regulation and function of IKK and IKK-related kinases regulation and function of IKK and IKK-related kinases. *Science's STKE : signal transduction knowledge environment*. 2006;re13.

34. Hara M, Bindokas V, Lopez JP, et al. Imaging endoplasmic reticulum calcium with a fluorescent biosensor in transgenic mice. *American Journal of Physiology-Cell Physiology*. 2004;287(4):C932-C938.

35. Harvey CD, Ehrhardt AG, Cellurale C, et al. A genetically encoded fluorescent sensor of ERK activity. *Proc Natl Acad Sci U S A*. 2008;105(49):19264-19269.

36. Hashimoto-Tane A, Yokosuka T, Ishihara C, Sakuma M, Kobayashi W, Saito T. T-cell receptor microclusters critical for T-cell activation are formed independently of lipid raft clustering. *Mol Cell Biol*. 2010;30(14):3421-3429.

37. Haugh JM. Live-cell fluorescence microscopy with molecular biosensors: What are we really measuring? *Biophys J*. 2012;102(9):2003-2011.

38. Herbst KJ, Allen MD, Zhang J. Luminescent kinase activity biosensors based on a versatile bimolecular switch. *J Am Chem Soc*. 2011;133(15):5676-5679.

39. Hires SA, Zhu Y, Tsien RY. Optical measurement of synaptic glutamate spillover and reuptake by linker optimized glutamate-sensitive fluorescent reporters. *Proc Natl Acad Sci U S A*. 2008;105(11):4411-4416.

40. Hoesel B, Schmid JA. The complexity of NF-kappa B signaling in inflammation and cancer. *Molecular Cancer*. 2013;12:86.

41. Huxford T, Huang D, Malek S, Ghosh G. The crystal structure of the I kappa B alpha/NF-kappa B complex reveals mechanisms of NF-kappa B inactivation. *Cell*. 1998;95(6):759-770.

42. Ibraheem A, Yap H, Ding Y, Campbell RE. A bacteria colony-based screen for optimal linker combinations in genetically encoded biosensors. *Bmc Biotechnology*. 2011;11:105.

43. Jares-Erijman EA, Jovin TM. FRET imaging. *Nat Biotechnol*. 2003;21(11):1387-1395.

44. Johnson SA, You Z, Hunter T. Monitoring ATM kinase activity in living cells. *Dna Repair*. 2007;6(9):1277-1284.

45. Kajimoto T, Sawamura S, Tohyama Y, Mori Y, Newton AC. Protein kinase C delta-specific activity reporter reveals agonist-evoked nuclear activity controlled by src family of kinases. *J Biol Chem*. 2010;285(53):41896-41910.

46. Kamioka Y, Sumiyama K, Mizuno R, et al. Live imaging of protein kinase activities in transgenic mice expressing FRET biosensors. *Cell Struct Funct*. 2012;37(1):65-73.

47. Kato M, Ito T, Wagner G, Richardson C, Ellenberger T. Modular architecture of the bacteriophage T7 primase couples RNA primer synthesis to DNA synthesis. *Mol Cell*. 2003;11(5):1349-1360.

48. Kawai Y, Sato M, Umezawa Y. Single color fluorescent indicators of protein phosphorylation for multicolor imaging of intracellular signal flow dynamics. *Anal Chem*. 2004;76(20):6144-6149.

49. Kohno T, Kubo Y, Yasui K, et al. Serum starvation activates NF-kappa B through G protein beta 2 subunit-mediated signal. *DNA Cell Biol*. 2012;31(11):1636-1644.

50. Komatsu N, Aoki K, Yamada M, et al. Development of an optimized backbone of FRET biosensors for kinases and GTPases. *Mol Biol Cell*. 2011;22(23):4647-4656.

51. Kunkel MT, Ni Q, Tsien RY, Zhang J, Newton AC. Spatio-temporal dynamics of protein kinase B/Akt signaling revealed by a genetically encoded fluorescent reporter. *J Biol Chem*. 2005;280(7):5581-5587.

52. Kwok S, Lee C, Sanchez SA, Hazlett TL, Gratton E, Hayashi Y. Genetically encoded probe for fluorescence lifetime imaging of CaMKII activity. *Biochem Biophys Res Commun*. 2008;369(2):519-525.

53. Lissandron V, Terrin A, Collini M, et al. Improvement of a FRET-based indicator for cAMP by linker design and stabilization of donor-acceptor interaction. *J Mol Biol*. 2005;354(3):546-555.

54. Macurek L, Lindqvist A, Lim D, et al. Polo-like kinase-1 is activated by aurora A to promote checkpoint recovery. *Nature*. 2008;455(7209):119-U88.

55. Marvin JS, Borghuis BG, Tian L, et al. An optimized fluorescent probe for visualizing glutamate neurotransmission. *Nature Methods*. 2013;10(2):162-170.

56. Mathes E, O'Dea EL, Hoffmann A, Ghosh G. NF-kappa B dictates the degradation pathway of I kappa B alpha. *EMBO J*. 2008;27(9):1357-1367.

57. McElhinny J, Trushin S, Bren G, Chester N, Paya C. Casein kinase II phosphorylates I kappa B alpha at S-283, S-289, S-293, and T-291 and is required for its degradation. *Mol Cell Biol*. 1996;16(3):899-906.

58. Mehta S, Zhang J. Reporting from the field: Genetically encoded fluorescent reporters uncover signaling dynamics in living biological systems. *Annu Rev Biochem*. 2011;80:375-+.

59. Miyawaki A. Visualization of the spatial and temporal dynamics of intracellular signaling. *Developmental Cell*. 2003;4(3):295-305.

60. Miyawaki A, Llopis J, Heim R, et al. Fluorescent indicators for Ca2+ based on green fluorescent proteins and calmodulin. *Nature*. 1997;388(6645):882-887.

61. Mower AF, Kwok S, Yu H, et al. Experience-dependent regulation of CaMKII activity within single visual cortex synapses in vivo. *Proc Natl Acad Sci U S A*. 2011;108(52):21241-21246.

62. Nagai T, Yamada S, Tominaga T, Ichikawa M, Miyawaki A. Expanded dynamic range of fluorescent indicators for ca(2+) by circularly permuted yellow fluorescent proteins. *Proceedings of the National Academies of Science*. 2004;101(29):10554-10559.

63. Nakai J, Ohkura M, Imoto K. A high signal-to-noise Ca2+ probe composed of a single green fluorescent protein. *Nat Biotechnol*. 2001;19(2):137-141.

64. Nakayama K, Nakayama K. Regulation of the cell cycle by SCF-type ubiquitin ligases. *Semin Cell Dev Biol*. 2005;16(3):323-333.

65. Neininger A, Thielemann H, Gaestel M. FRET-based detection of different conformations of MK2. *EMBO Rep*. 2001;2(8):703-708.

66. Newman RH, Zhang J. Visualization of phosphatase activity in living cells with a FRET-based calcineurin activity sensor. *Molecular Biosystems*. 2008;4(6):496-501.

67. Oliveira AF, Yasuda R. An improved ras sensor for highly sensitive and quantitative FRET-FLIM imaging. *Plos One*. 2013;8(1):e52874.

68. Olson CA, Liao H, Sun R, Roberts RW. mRNA display selection of a high-affinity, modification-specific phospho-I kappa B alpha-binding fibronectin. *Acs Chemical Biology*. 2008;3(8):480-485.

69. Ouyang M, Sun J, Chien S, Wang Y. Determination of hierarchical relationship of src and rac at subcellular locations with FRET biosensors. *Proc Natl Acad Sci U S A*. 2008;105(38):14353-14358.

70. Ozes O, Mayo L, Gustin J, Pfeffer S, Pfeffer L, Donner D. NF-kappa B activation by tumour necrosis factor requires the akt serine-threonine kinase. *Nature*. 1999;401(6748):82-85.

71. Padilla-Parra S, Tramier M. FRET microscopy in the living cell: Different approaches, strengths and weaknesses. *Bioessays*. 2012;34(5):369-376.

72. Palmer AE, Giacomello M, Kortemme T, et al. Ca2+ indicators based on computationally redesigned calmodulin-peptide pairs. *Chem Biol*. 2006;13(5):521-530.

73. Parrini MC, Camonis J, Matsuda M, de Gunzburg J. Dissecting activation of the PAK1 kinase at protrusions in living cells. *J Biol Chem*. 2009;284(36):24133-24143.

74. Periasamy A, Wallrabe H, Chen Y, Barroso M. Quantitation of protein-protein interactions: Confocal FRET microscopy. *Biophysical Tools for Biologists, Vol 2: in Vivo Techniques*. 2008;89:569-+.

75. Piljic A, de Diego I, Wilmanns M, Schultz C. Rapid development of genetically encoded FRET reporters. *Acs Chemical Biology*. 2011;6(7):685-691.

76. Piston DW, Rizzo MA. FRET by fluorescence polarization microscopy. *Fluorescent Proteins, Second Edition*. 2008;85:415-430.

77. Rebois RV, Robitaille M, Petrin D, Zylbergold P, Trieu P, Hebert TE. Combining protein complementation assays with resonance energy transfer to detect multipartner protein complexes in living cells. *Methods*. 2008;45(3):214-218.

78. Roff M, Thompson J, Rodriguez M, et al. Role of I kappa B alpha ubiquitination in signal-induced activation of NF-kappa B in vivo. *J Biol Chem*. 1996;271(13):7844-7850.

79. Rothman DM, Shults MD, Imperiali B. Chemical approaches for investigating phosphorylation in signal transduction networks. *Trends Cell Biol*. 2005;15(9):502-510.

80. Sasaki K, Sato M, Umezawa Y. Fluorescent indicators for Akt/protein kinase B and dynamics of akt activity visualized in living cells. *J Biol Chem*. 2003;278(33):30945-30951.

81. Sato M, Kawai Y, Umezawa Y. Genetically encoded fluorescent indicators to visualize protein phosphorylation by extracellular signal-regulated kinase in single living cells. *Anal Chem*. 2007;79(6):2570-2575.

82. SCHERER D, BROCKMAN J, CHEN Z, MANIATIS T, BALLARD D. Signal-induced degradation of I-kappa-B-alpha requires site-specific ubiquitination. *Proc Natl Acad Sci U S A*. 1995;92(24):11259-11263.

83. Shinohara H, Behar M, Inoue K, et al. Positive feedback within a kinase signaling complex functions as a switch mechanism for NF-kappa B activation. *Science*. 2014;344(6185):760-764.

84. Sipieter F, Vandame P, Spriet C, et al. From FRET imaging to practical methodology for kinase activity sensing in living cells. *Fluorescence-Based Biosensors: from Concepts to Applications*. 2013;113:145-216.

85. Song Y, Rodgers VGJ, Schultz JS, Liao J. Protein interaction affinity determination by quantitative FRET technology. *Biotechnol Bioeng*. 2012;109(11):2875-2883.

86. Spencer SL, Cappell SD, Tsai F, Overton KW, Wang CL, Meyer T. The proliferation-quiescence decision is controlled by a bifurcation in CDK2 activity at mitotic exit. *Cell*. 2013;155(2):369-383.

87. Sun Y, Rombola C, Jyothikumar V, Periasamy A. Forster resonance energy transfer microscopy and spectroscopy for localizing protein-protein interactions in living cells. *Cytometry Part a*. 2013;83(9):780-793.

88. Suzuki H, Chiba T, Suzuki T, et al. Homodimer of two F-box proteins beta TrCP1 or beta TrCP2 binds to I kappa B alpha for signal-dependent ubiquitination. *J Biol Chem*. 2000;275(4):2877-2884.

89. Takao K, Okamoto KI, Nakagawa T, et al. Visualization of synaptic Ca2+/calmodulin-dependent protein kinase II activity in living neurons. *Journal of Neuroscience*. 2005;25(12):3107-3112.

90. Tantama M, Hung YP, Yellen G. Optogenetic reporters: Fluorescent protein-based genetically encoded indicators of signaling and metabolism in the brain. *Optogenetics: Tools for Controlling and Monitoring Neuronal Activity*. 2012;196:235-263.

91. Tay S, Hughey JJ, Lee TK, Lipniacki T, Quake SR, Covert MW. Single-cell NF-kappa B dynamics reveal digital activation and analogue information processing. *Nature*. 2010;466(7303):267-U149.

92. Terai K, Matsuda M. Ras binding opens c-raf to expose the docking site for mitogen-activated protein kinase kinase. *EMBO Rep*. 2005;6(3):251-255.

93. Terai K, Matsuda M. The amino-terminal B-raf-specific region mediates calcium-dependent homo- and hetero-dimerization of raf. *EMBO J*. 2006;25(15):3556-3564.

94. Timm T, von Kries JP, Li X, Zennpel H, Mandelkow E, Mandelkow E. Microtubule affinity regulating kinase activity in living neurons was examined by a genetically encoded

fluorescence resonance energy Transfer/Fluorescence lifetime imaging-based biosensor INHIBITORS WITH THERAPEUTIC POTENTIAL. *J Biol Chem*. 2011;286(48):41711-41722.

95. Ting AY, Kain KH, Klemke RL, Tsien RY. Genetically encoded fluorescent reporters of protein tyrosine kinase activities in living cells. *Proc Natl Acad Sci U S A*. 2001;98(26):15003-15008.

96. Tomida T, Takekawa M, O'Grady P, Saito H. Stimulus-specific distinctions in spatial and temporal dynamics of stress-activated protein kinase kinase kinases revealed by a fluorescence resonance energy transfer biosensor. *Mol Cell Biol*. 2009;29(22):6117-6127.

97. TRAENCKNER E, PAHL H, HENKEL T, SCHMIDT K, WILK S, BAEUERLE P. Phosphorylation of human I-kappa-B-alpha on serine-32 and serine-36 controls I-kappa-B-alpha proteolysis and nf-kappa-B activation in response to diverse stimuli. *EMBO J*. 1995;14(12):2876-2883.

98. Tsou L, Zheng B, Hsu C, Sasaki AT, Cantley LC. A fluorescent reporter of AMPK activity and cellular energy stress. *Cell Metabolism*. 2011;13(4):476-486.

99. Violin JD, Zhang J, Tsien RY, Newton AC. A genetically encoded fluorescent reporter reveals oscillatory phosphorylation by protein kinase C. *J Cell Biol*. 2003;161(5):899-909.

100. Wang YX, Botvinick EL, Zhao YH, et al. Visualizing the mechanical activation of src. *Nature*. 2005;434(7036):1040-1045.

101. Williams DA, Fogarty KE, Tsien RY, Fay FS. Calcium gradients in single smooth-muscle cells revealed by the digital imaging microscope using fura-2. *Nature*. 1985;318(6046):558-561.

102. Winston J, Strack P, Beer-Romero P, Chu C, Elledge S, Harper J. The SCF beta-TRCP-ubiquitin ligase complex associates specifically with phosphorylated destruction motifs in I kappa B alpha and beta-catenin and stimulates I kappa B alpha ubiquitination in vitro (vol 13, pg 270, 1999). *Genes Dev*. 1999;13(8):1050-1050.

103. Witt J, Barisic S, Schumann E, et al. Mechanism of PP2A-mediated IKK beta dephosphorylation: A systems biological approach. *Bmc Systems Biology*. 2009;3:71.

104. Wu G, Xu G, Schulman B, Jeffrey P, Harper J, Pavletich N. Structure of a beta-TrCP1-Skp1-beta-catenin complex: Destruction motif binding and lysine specificity of the SCF beta-TrCP1 ubiquitin ligase. *Mol Cell*. 2003;11(6):1445-1456.

105. Wu-Zhang AX, Murphy AN, Bachman M, Newton AC. Isozyme-specific interaction of protein kinase C delta with mitochondria dissected using live cell fluorescence imaging. *J Biol Chem*. 2012;287(45).

106. Yamaguchi Y, Shinotsuka N, Nonomura K, et al. Live imaging of apoptosis in a novel transgenic mouse highlights its role in neural tube closure. *J Cell Biol*. 2011;195(6):1047-1060.

107. Yoshizaki H, Mochizuki N, Gotoh Y, Matsuda M. Akt-PDK1 complex mediates epidermal growth factor-induced membrane protrusion through ral activation. *Mol Biol Cell*. 2007;18(1):119-128.

108. Zaccolo M, De Giorgi F, Cho CY, et al. A genetically encoded, fluorescent indicator for cyclic AMP in living cells. *Nat Cell Biol*. 2000;2(1):25-29.

109. Zhang J, Ma YL, Taylor SS, Tsien RY. Genetically encoded reporters of protein kinase A activity reveal impact of substrate tethering. *Proc Natl Acad Sci U S A*. 2001;98(26):14997-15002.

110. Zhou V, Gao X, Han S, Brinker A, Caldwell JS, Gu X. An intracellular conformational sensor assay for abl T315I. *Analyt Biochem*. 2009;385(2):300-308.

111. Zhou X, Clister TL, Lowry PR, Seldin MM, Wong GW, Zhang J. Dynamic visualization of mTORC1 activity in living cells. *Cell Reports*. 2015;10(10):1767-1777.

Chapter 4. Discussion

1. Alves, BN, Tsui, R, Almaden, J, Shokhirev, MN, Davis-Turak, J, Fujimoto, J, Birnbaum, H, Ponomarenko, J, Hoffmann, A. I kappa B epsilon is a key regulator of B cell expansion by providing negative feedback on cRel and RelA in a stimulus-specific manner. *Journal of Immunology*. 2014;192(7):3121-3132.

2. Cho J, Chang H, Kwon SC, et al. LIN28A is a suppressor of ER-associated translation in embryonic stem cells. *Cell*. 2012;151(4):765-777.

3. Depry C, Mehta S, Li R, Zhang J. Visualization of compartmentalized kinase activity dynamics using adaptable BimKARs. *Chem Biol*. 2015;22(11):1470-1479.

4. Geiger A, Russo L, Gensch T, et al. Correlating calcium binding, forster resonance energy transfer, and conformational change in the biosensor TN-XXL. *Biophys J*. 2012;102(10):2401-2410.

5. Gratz A, Goetz C, Jose J. A FRET-based microplate assay for human protein kinase CK2, a target in neoplastic disease. *Journal of Enzyme Inhibition and Medicinal Chemistry*. 2010;25(2):234-239.

6. Haugh JM. Live-cell fluorescence microscopy with molecular biosensors: What are we really measuring? *Biophys J*. 2012;102(9):2003-2011.

7. Lohse MJ, Nuber S, Hoffmann C. Fluorescence/Bioluminescence resonance energy transfer techniques to study G-protein-coupled receptor activation and signaling. *Pharmacol Rev*. 2012;64(2):299-336.

8. Mertens HDT, Piljic A, Schultz C, Syergun DI. Conformational analysis of a genetically encoded FRET biosensor by SAXS. *Biophys J*. 2012;102(12):2866-2875.

9. Nakamura, T., Kunz, R., Zhang, C., Kimura, T., Yuan, C., Baccaro, B., Namiki, Y., Gygi, S., Hotamsligil, G. A critical role for PKR complexes with TRBP in immumetabolic regulation and eIF2-alpha phosphorylation in obesity. *Cell Reports*. 2015;11:295.

10. Nobis M, McGhee EJ, Morton JP, et al. Intravital FLIM-FRET imaging reveals dasatinib-induced spatial control of src in pancreatic cancer. *Cancer Res*. 2013;73(15):4674-4686.

11. Olson CA, Liao H, Sun R, Roberts RW. mRNA display selection of a high-affinity, modification-specific phospho-I kappa B alpha-binding fibronectin. *Acs Chemical Biology*. 2008;3(8):480-485.

12. Palmer AE, Qin Y, Park JG, McCombs JE. Design and application of genetically encoded biosensors. *Trends Biotechnol*. 2011;29(3):144-152.

13. Robinson KH, Yang JR, Zhang J. FRET- and BRET-based biosensors in live cell compound screens. In: Zhang J, Ni Q, Newman RH, ed. *Fluorescent protein based biosensors: Methods and protocols.* ; 2014:217-225.

14. Stalder, L., Heusermann, W., Sokol, L., Trojer, D., Wirz, J., Hean, J., Fritzsche, A., Aeschimann, F., Pfanzagl, V., Basselet, P., Weiler, J., Hintersteiner, M., Morrisey, D., Meisner-Kober, N. The rough endoplasmic reticulum is a central nucleation site of siRNA-mediated RNA silencing. *The EMBO Journal*. 2013;32:1115.

15. Tian, L, Akerboom, J, Schreiter, E, Looger, L. Neural activity imaging with genetically encoded calcium indicators. In: Knopfel T BE, ed. *Optogenetics: Tools for controlling and monitoring neural activity.* ; 2012:79-94. 10.1016/B978-0-444-59426-6.00005-7.

16. Timm T, von Kries JP, Li X, Zennpel H, Mandelkow E, Mandelkow E. Microtubule affinity regulating kinase activity in living neurons was examined by a genetically encoded fluorescence resonance energy Transfer/Fluorescence lifetime imaging-based biosensor INHIBITORS WITH THERAPEUTIC POTENTIAL. *J Biol Chem*. 2011;286(48):41711-41722.

17. Tsalkova T, Mei FC, Li S, et al. Isoform-specific antagonists of exchange proteins directly activated by cAMP. *Proc Natl Acad Sci U S A*. 2012;109(45):18613-18618.

Appendix: Extended methods

1. Amen AM, Ruiz-Garzon CR, Shi J, Subramanian M, Pham DL, Meffert MK. A rapid induction mechanism for Lin28a in trophic responses. *Mol Cell*. 2017;65(3):490-+.

2. Daher A, Longuet M, Dorin D, et al. Two dimerization domains in the trans-activation response RNA-binding protein (TRBP) individually reverse the protein kinase R inhibition of HIV-1 long terminal repeat expression. *J Biol Chem*. 2001;276(36):33899-33905.

3. Daher A, Laraki G, Singh M, et al. TRBP control of PACT-induced phosphorylation of protein kinase R is reversed by stress. *Mol Cell Biol*. 2009;29(1):254-265.

4. Griesbeck O, Baird G, Campbell R, Zacharias D, Tsien R. Reducing the environmental sensitivity of yellow fluorescent protein - mechanism and applications. *J Biol Chem*. 2001;276(31):29188-29194.

5. Huang Y ZL. An in vitro single primer site-directed mutagenesis method for use in biotechnology. In: *Methods in molecular biology: In vitro mutagenesis.* ; 2016:375-383.

6. Llopis J, McCaffery M, Miyawaki A, Farquhart M, Tsien RY. Measurement of cytosolic, mitochondrial, and golgi pH in single living cells with green fluorescent proteins. *Proceedings of the National Academies of Science*. 1998;95(12):6803-6808.

7. Nagai T, Yamada S, Tominaga T, Ichikawa M, Miyawaki A. Expanded dynamic range of fluorescent indicators for ca(2+) by circularly permuted yellow fluorescent proteins.. *Proceedings of the National Academies of Science*. 2004;101(29):10554-10559.

8. Nagai T, Yamada S, Tominaga T, Ichikawa M, Miyawaki A. Expanded dynamic range of fluorescent indicators for Ca2+ by circularly permuted yellow fluorescent proteins. *Proc Natl Acad Sci U S A*. 2004;101(29):10554-10559.

9. Rizzo M, Springer G, Granada B, Piston D. An improved cyan fluorescent protein variant useful for FRET. *Nat Biotechnol*. 2004;22(4):445-449.

10. Thevanez P, Ruttimann UE, Unser M. A pyramid approach to subpixel registration based on intensity. . 1998;7(1):27.

11. Xia Z, Liu Y. Reliable and global measurement of fluorescence resonance energy transfer using fluorescence microscopes. *Biophys J*. 2001;81(4):2395-2402.

Curriculum Vitae

LAUREL OLDACH

Laurel.Oldach@gmail.com

(410) 925 7139

EDUCATION

Ph.D. 2018 Johns Hopkins University School of Medicine

Biochemistry, Cellular and Molecular Biology- Pharmacology

Advisors: Dr. Jin Zhang, Ph.D., and Dr. Mollie Meffert, M.D.-Ph.D.

B.A. 2011 Biology Reed College, Portland, OR

Phi Beta Kappa. Advisor: Dr. Stephen Arch, Ph.D.

RESEARCH EXPERIENCE

Johns Hopkins University School of Medicine 2011-2018

Graduate researcher supervised by Drs. Jin Zhang & Mollie Meffert Baltimore, MD

Characterization of the interaction between dsRNA binding proteins lin28a and TRBP.

- Conducted an interdisciplinary project comentored by two principal investigators to characterize a phosphorylation-dependent protein-protein interaction regulating microRNA biogenesis.
- Utilized classical biochemistry techniques to demonstrate Erk-mediated interaction of lin28a and TRBP, and developed a novel FRET biosensor to visualize binding in primary neuronal cell culture.

Reed College 2010 - 2011

Undergraduate researcher supervised by Dr. Stephen Arch Portland, OR

- Completed an undergraduate honors thesis investigating signaling mechanisms in axonal transport of mRNA transcript for a neurohormone in *Aplysia californica*
- Utilized pharmacological interventions to perturb mRNA localization in *ex vivo* ganglion culture.

University of North Carolina- Chapel Hill Summers, 2009-2010

Undergraduate research assistant supervised by Dr. Alex Duncan Chapel Hill, NC

- Optimized purification strategy for a pore-forming membrane protein, *Neisseria gonorrhoeae* porin B, to study its effects on innate immune signaling through the NLRP3 inflammasome.
- Characterized the effects of purified porin B on cytokine secretion and cell death in monocytes.

ACADEMIC AWARDS AND HONORS

2013 NSF Graduate Fellowship Honorable Mention

2011 Turock Family Foundation Research Grant, JHUSOM

2011 Phi Beta Kappa, Reed College

2011 Dean's Commendation for Academic Excellence, Reed College

2010 Biology Undergraduate Research Project Grant, Reed College

2010 Carolina Summer Fellowship (REU), University of North Carolina-Chapel Hill

PUBLICATIONS

Oldach L, Gorshkov K, Zhang J & Meffert MK. Dynamic visualization of Lin28a upregulation by TRBP. *Molecular Biology of the Cell* 29 (10).

Oldach L & Zhang J (2014). Genetically encoded fluorescent biosensors for live-cell visualization of protein phosphorylation. *Chemistry and Biology* 21(2).

Mehta S, Aye-Han N, Ganesan A, **Oldach L**, Gorshkov K, & Zhang J (2014). Calmodulin-controlled spatial decoding of oscillatory Ca2+ signals by calcineurin. *eLife* 10.7554/eLife.03765

Zhu W, Vengevogel MS, Knilans KJ, Anderson JE, **Oldach LM**, McKinnon KP, Hobbs MM, Sempowski GD, Duncan JA (2012). *Neisseria gonorrhoeae* suppresses dendritic cell-induced, antigen-dependent CD4 T cell proliferation. *PLoS One* 7(7).

POSTERS AND TALKS

December 2017. Biological Chemistry Department Thursday Evening Research Discussion, Johns Hopkins University, Baltimore, MD. “Visualization of Lin28a/TRBP binding in living neurons.”

December 2017. Center for Cell Dynamics Seminar Series, Johns Hopkins University, Baltimore, MD (invited; seminar cancelled due to schedule conflict).

March 2017. Pharmacology Department Research in Progress Seminar Series, Johns Hopkins University. “Visualizing the Interaction of dsRNA binding proteins Lin28a and TRBP.”

October 2016. Oldach L, Gorshkov K, Zhang J, Meffert MK. Poster. Biological Chemistry Departmental Retreat, Johns Hopkins University, Baltimore, MD. “Development of a FRET sensor for the interaction between Lin28a and TRBP.”

January 2016. Pharmacology Department Research in Progress Seminar Series, Johns Hopkins. “Phosphorylation-dependent interaction between dsRNA binding proteins Lin28a and TRBP.”

March 2015. Biochemistry, Cellular and Molecular Biology program colloquium. “Characterizing the interaction between dsRNA-binding proteins Lin28a and TRBP.”

September 2014. Oldach L, Zhang J, Meffert MK. “Investigating an interaction between Lin28a and TRBP.” Poster. 2014 Biochemistry, Cellular and Molecular Biology Program Retreat. St. Michael’s, Maryland.

April 2014. Pharmacology Department Research in Progress Seminar Series. “Toward an optical sensor for IKK activity.”

TEACHING EXPERIENCE

Johns Hopkins University School of Medicine	**Baltimore, MD**
Teaching Assistant, Cell Structure and Dynamics	Spring 2015
Teaching Assistant, Method and Logic in Biology	Summer 2014
Teaching Assistant, Cell Structure and Dynamics	Spring 2014
Reed College	**Portland, OR**
Scientific Writing Tutor	2011
Teaching Assistant, Animal Behavior	2010
Tutor, Introductory Biology	2010

SERVICE AND LEADERSHIP

Science Cafe Coordinator, Project Bridge (JHUSOM) 2016

Recruited senior scientists to give short talks and Q-and-A sessions to the public; scheduled with local businesses as venues.

Staff writer, BCMB Community Newsletter (JHUSOM) 2012 - 2013

Reported on seminars, curriculum changes, and other program news; copy-edited peers' submissions.

Science outreach teacher, Village Learning Place (Baltimore) Summer 2013

Led weekly classroom lessons and hands-on demonstrations of scientific methods and principles to third-grade students.